Effects of Chronic Hypertension and Acute Cerebral Ischemia on Blood-Brain Barrier Permeability, Brain Water Content, and Cerebral Blood Volume Using MRI

Guihua Zhai

A dissertation submitted to the faculty of the University of North Carolina at Chapel Hill in partial fulfillment of the requirements for the degree of Doctor of Philosophy in the Department of Biomedical Engineering.

Chapel Hill
2006

Approved by:

Weili Lin
Keith Smith
David Lalush
Carol Lucas
Hongyu An
Henry Hsiao

ABSTRACT

GUIHUA ZHAI: Effects of Chronic Hypertension and Acute Cerebral Ischemia on Blood-Brain Barrier Permeability, Brain Water Content, and Cerebral Blood Volume Using MRI
(Under the direction of professor Weili Lin)

The process of stroke alters the vascular physiology of the brain. In this dissertation, we have focused on the assessment of cerebrovascular alterations under two ischemic conditions: chronic hypertension with increased cerebral blood perfusion pressure (CPP) and transient focal cerebral ischemia with decreased CPP via the stroke-prone spontaneous hypertensive rats (SHRsp) model and the suture model, respectively. Based on these two models, the temporal evolutions of water content, permeability of BBB and cerebral blood volume (CBV), were monitored using magnetic resonance imaging (MRI).

In SHRsp rats, there was no significant water content increase before BBB breakdown, indicating the vasogenic nature of the edema. A weak linear relationship was found between the water content and the permeability to Gd-DTPA during edema development after BBB breakdown, suggesting that the movement of water into brain tissue could have been facilitated by the increase in cerebrovascular permeability to such small molecules as Gd-DTPA. In addition, our results showed that, in SHRsp rats, the occurrence of BBB breakdown was no later than the presence of hemorrhage and the decrease of CBV under the symptoms of weight loss and enlarged ventricles.

In a suture model of 90 min occlusion, while BBB permeability followed a biphasic pattern, the water content showed an increasing trend. BBB leakage did not play an important

role in water content increase out to at least 6hr after reperfusion. After that, BBB breakdown worsened the edema formation. When permeability was recovered at 24 hr after reperfusion, water content reached its maximal value of the study period.

In conclusion, though both chronic hypertension with increased CPP or acute ischemia with decreased CPP can result in BBB breakdown and edema development, the stroke development patterns are different under these two conditions. Our results shed some light on the roles of BBB breakdown in edema formation, may help to evaluate and monitor the effectiveness of therapeutic intervention, and may aid the development of new therapies targeted at maintainance of the BBB.

ACKNOWLEDGEMENTS

First, I would like to sincerely thank my advisor Dr. Weili Lin for his generous financial support and academic guidance. I have worked under Dr. Lin's supervision for six years. During this period I have grown from a nervous student, knowing nothing about MRI but a simple birdcage coil, to an experienced researcher. Second, I would like to thank all my committee members: Dr. Lucus, Dr. Lalush, Keith Smith, Hongyu An and Dr. Hsiao for their time, for giving insightful questions for my written exam, and preliminary oral exam. Specifically, I sincerely thank Keith and Dr. Hsiao for their generous encouragement and valuable suggestions.

I am grateful to all my fellow graduate students, both past and present, dear Hui Liu and Peter Nicholas for their whole-hearted help, Qingwei Liu, Bremer Jonathan, Yueh Lee for their friendship. I also need to thank Xiuzhi Lu, Liansheng Chang and Kim Liu for their technical help.

Finally, I want to express my gratitude to all my family members for their continued love and support.

TABLE OF CONTENTS

LIST OF FIGURES viiii

Chapter

1 Introduction 1

1.1 Literature Review on Animal Models for Stroke Research 1

1.2 Two Animal Models: SHRsp Rats and the Suture Model 2

1.3 Three Parameters 8

1.4 Specific Aims 11

1.5 Main Challenges 13

1.6 Major Accomplishments in this Dissertation 13

1.7 Organization of this Dissertation 14

2 Physiological Concepts Pertaining to the Proposed Studies 16

2.1 Stroke 16

2.2 Blood-Brain Barrier (BBB) 18

2.3 Metabolism 20

2.4 Circulation in the Human Brain 21

2.5 SHRsp Rats 24

2.6 The Suture Model 26

3 Physical Principles of Magnetic Resonance 31

3.1 Principles of Magnetic Resonance 31

3.2 Spin-Lattice Interaction and Spin-Spin Interaction 33

3.3 Signal Detection....34
3.4 Spatial Localization of the Spins....35
3.5 Sequence Diagram....36
3.5.1 2D Gradient Echo Imaging....36
3.5.2 Spin Echo Example....40
3.5.3 3D Volume Imaging....42
3.6 Signal, Noise, and Contrast....44
3.7 Fast Imaging Methods....49
3.7.1 EPI Sequence....49
3.7.2 FLASH Sequence....53
4 Dissertation Related Methods....56
4.1 Absolute Water Content Measurement....56
4.2 The Steady-State Method to Measure CBV....59
4.2.1 The Steady-State Method....59
4.2.2 Error propagation from the signal measurement into CBV estimation....60
4.2.3 Imaging parameters selection....60
4.2.4 Water Exchange Mechanisms....62
4.3 Dynamic Susceptibility Contrast (DSC)....65
4.4 The Continuous Arterial Spin Labeling (CASL) Method to Measure CBF....67
4.5 Patlak Plot Method to Measure Permeability....71
4.6 Look-locker Method to Measure T1....75
4.7 UNFOLD....77
4.8 Magnetization Transfer Contrast (MTC)....81

5 Major Findings on SHRsp Rats.....85

5.1 Vascular Permeability and Absolute Water Content in SHRsp Rats: A Magnetic Resonance Imaging Approach.....85

5.2 Vascular Permeability May Spatially Predict Subsequent Hemorrhages in Stroke-prone Spontaneous Hypertensive Rats.....105

5.3 Regional Cerebral Blood Volume Alteration in Stroke-Prone Spontaneous hypertensive Rats.....109

6 Temporal and Spatial Relationship Between Water Content and Permeability in the Suture Model.....116

7 Conclusions and Future Directions.....128

REFERENCES: 131

LIST OF FIGURES

Figure

2.1: Schematic representation of the positions of the main arteries. ACA, anterior cerebral artery; PCA, posterior cerebral artery; MCA, middle cerebral artery; SCA, superior cerebellar artery; CCA, common carotid artery; ECA, external carotid artery; ICA, internal carotid artery..... 30

3.1: Sequence diagram for a 2D gradient echo imaging sequence..... 39

3.2: Traversal of k-space for the sequence shown in Fig. 3.1..... 41

3.3: The sequence diagram for a 2D spin echo imaging sequence..... 43

3.4: A 3D gradient echo imaging sequence in which the two directions orthogonal to the read direction are phase encoded. 45

3.5: An EPI sequence showing the phase encoding and read gradient waveforms. 51

3.6: A spin echo EPI imaging sequence..... 52

4.1: Plot of voxel signal measured on a phantom with large flip angles around 180^0. The signal measurements are least-squares fitted to the solid line. 58

4.2: The signal as a function of flip angle pre contrast agent for blood ('o'), gray matter ('*'), and white matter ('+'). 61

4.3: The signal as a function of flip angle post contrast agent for blood ('o'), gray matter ('*'), and white matter ('+'). 62

4.4: signal curves of the voxels chosen to obtain global arterial input function. 68

4.5: Concentration curve as the global arterial input function. 69

4.6: rCBF, rMTT and rCBV maps on an ischemia rat during occlusion period. 70

4.7: Pulse sequence timing diagram. Labeling RF and gradients are applied during the labeling period. Then, a postlabeling delay is inserted. Finally, rapid gradient-echo echo-planar imaging is performed to acquire images. 72

4.8: A typical CBF map under ischemic condition. 72

4.9: A Model of blood-brain exchange. The test solute may move from the plasma to any of the reversible compartments or vice versa; the solute can enter, but can not leave the irreversible regions..... 73

4.10: Schematic diagram of the TOMROP sequence. 76

4.11: a: The sampling function is shifted along the phase-encoding direction; b: the shift generates a phase ramp in the point spread function shown in b; c: phase shifts are passed to the images in c..... 79

4.12: Object and aliasing components occupy different frequencies. 79

4.13: Aliased images on a phantom with half k-space coverage a: without and b: with shifting the sampling function along the phase-encoding direction; c: reconstructed image using UNFOLD method..... 80

4.14: Water proton magnetization transfer in biological tissues..... 82

4.15: MT related maps (a) T_{1s} (b) T_1 (c) M_0 (d) M_{0s} (e) K_{for} (f) MTR of a stroke rat with 90 min occlusion 48hrs after reperfusion. 84

5.1: Patlak plot of the data from one voxel with BBB leakage and one voxel with normal BBB. 92

5.2: T2-weighted images from a: group A; b: group B and c: group C. 94

5.3: a: A T2-weighted image and b: the corresponding permeability map. 96

5.4: A T2-weighted image of one rat with hemorrhage. 96

5.5: T2-weighted images of one rat during the five consecutive weeks. 97

5.6: The temporal evolution of brain water content of different rats..... 99

5.7: The temporal evolution of permeability of different rats..... 99

5.8: Water content of rat brain of group A, group B and group C. Error bars are the standard deviation of the intra-subject variability. 100

5.9: Relationship between water content and permeability of rats in group C. 100

5.10: The temporal evolution of T2-weighted images, $T2^*$-weighted images, and permeability maps of a representative rat. 108

5.11: Representative T2-weighted image, T1-weighted image pre and post contrast, and permeability map..... 112

5.12: CBV values of four ROIs at three different stages: normal, with enlarged ventricle/weight loss, with lesions. 112

5.13: CBV alteration of different areas at different time points in the normal rats. 112

6.1: T2-weighted image showing final lesion 24 hrs after reperfusion, a: lesion both in cortex and striatum, b: lesion only in stritum. 120

6.2: T2-weighted images, a: 1hr and b: 24 hr after reperfusion; permeability maps, c: 1hr and d: 24hr after reperfusion; T1-weighted images, e: 1hr and f: 24hr after reperfusion. 121

6.3: The evolution of water content for group B. 122

6.4: The relationship between water content and permeability for group B1. 123

CHAPTER 1

Introduction

Magnetic resonance imaging (MRI) has emerged as a powerful non-invasive imaging modality due to its flexibility, versatility, high resolution, and sharp contrast. It has been extensively used for many applications ranging from clinical diagnosis to anatomic/functional study, as well as for pathological investigation. Compared with computer tomography (CT), MRI can obtain images with superior soft tissue contrast and without any risk of radiation, which are preferable in the structural, functional and pathological study of human brain. This comes at the expense of increased scanning time and equipment cost, however. This dissertation is focused on pathological study of stroke using two animal models: stroke-prone spontaneous hypertensive (SHRsp) rats and the suture model.

1.1 Literature Review on Animal Models for Stroke Research

Stroke is the third leading cause of death in the US. Based on the underlying causes stroke can be classified into two categories: ischemic stroke and hemorrhagic stroke. About 75% of all strokes have the clinical expression of brain infarctions; large, usually single, brain hemorrhages occupy the background for about 11%; and subrachnoid hemorrhages make up almost 5% of all strokes[116].

For the systematic study of the pathophysiology and treatment of cerebral ischemia, animal models have to be used due to the following reasons. 1) Human ischemic stroke is

diverse in its causes and anatomic sites; the use of standardized animals selected for uniformity removes the uncontrollable variables encountered in human disease and permits relatively simple analysis and assessment of pathogenesis and treatment. 2) Invasive surgical procedures and direct access to brain tissue are often required for rigorous investigation. 3) Ischemic insult during the first seconds to minutes can be studied only in animals. 4) In vitro models such as tissue slices or neuronal/glial cell cultures are lacking vasculature, which is essential for the study of abnormal perfusion[116]. To study brain ischemia, rodents are more desirable over larger animal species (notably cats, dogs, rabbits, and subhuman primates) from several vantage points: 1) low cost, 2) lower cost of procedures, 3) genetically homogeneity within strains owing to inbreeding, 4) close resemblance of its cerebral circulation to that of humans, 5) small brain size suitable for biochemical analysis via in vivo freeze-trapping and 6) greater acceptability from both ecologic and ethical perspectives[114].

Basically, the rodent models of cerebral ischemia can be classified into two categories: models of global cerebral ischemia and models of focal cerebral ischemia. Models of global cerebral ischemia include the two-vessel and four-vessel occlusion models of forebrain ischemia, and ischemia models involving elevated cerebrospinal fluid pressure, neck tourniquet, decapitation, or Levine preparation of hypoxia-ischemia[114]. Models of focal cerebral ischemia in rats include the middle cerebral artery occlusion model, stroke-prone spontaneous hypertensive rats (SHRsp), and miscellaneous models of cerebral embolism and thrombosis, such as blood clot embolization, microsphere embolization, photochemically initiated thromboembolism, and arachidonate-induced thrombosis[114].

1.2 Two Animal Models: SHRsp Rats and the Suture Model

Stroke represents a disease of the blood vessels in the brain that typically results in a reduction of, or disruption in, blood flow to the brain. The rate of cerebral blood flow depends on two factors: (1) cerebral perfusion pressure (CPP), the difference between the arterial and intracranial pressures at the level of the cranium and (2) the resistance or hindrance of the vessels of the brain[104]. Either increased CPP or decreased CPP can result in the abnormality of cerebral blood flow.

In this dissertation, we focused on two focal ischemic models: SHRsp rats and the suture model to study two CPP modulated ischemic conditions: chronic hypertension with increased CPP and transient focal cerebral ischemia with decreased CPP.

CPP can be defined as:

CPP=MAP-ICP

MAP is the mean arterial pressure and ICP (Intracranial pressure) is the pressure within the rigid skull.

The principle constituents within the skull are brain (80%), blood (12%) and CSF (8%). The total human volume is 1600ml. With an increase of the volume of the contents of the skull, a rigid fluid-filled container, the pressure inside will rise considerably.

When the intracranial pressure rises due to developed edema, cerebrovascular resistance increases, since these vessels are compressed. Cerebral blood flow is reduced accordingly, except that a normal blood flow can be preserved by the rise in blood pressure, which accompanies increased intracranial pressure.

Under normal conditions, cerebral blood flow (CBF) can be kept constant between the arterial pressure limits of 60 and 140 mmHg by altering the diameter of the blood vessels, hence changing cerebral blood volume (CBV) in brain tissues.

Under hypertension, the autoregulatory mechanisms to maintain constant CBF could be altered. For example, the autoregulatory range can shift to a higher pressure in patients with hypertension. When blood pressure rises above the upper limit, blood flow increases rapidly with increased CPP and could potentially cause severe overstretching or rupture of cerebral blood vessels, sometimes resulting in serious brain edema or cerebral hemorrhage[102]. In contrast to chronic hypertension, CPP falls under the condition of cerebral ischemia, though MAP may not change much. When an artery becomes narrowed or completely occluded, its resistance increases and hence the pressure drops along its length. This results in a reduced pressure at the level of smaller arteries and arterioles, which are the primary vessels for regulating blood flow within an organ.

When CPP falls, the cerebrovasculature can respond with two compensatory mechanisms serving to maintain the normal delivery of oxygen and nutrients. First, resistance arterioles can dilate in order to reduce vascular resistance and maintain cerebral blood flow (CBF) at near normal levels. The second compensatory mechanism is through increases in oxygen extraction fraction (OEF) [103-105]. When the delivery of oxygen falls, the amount of available oxygen extracted from the blood can increase in order to maintain normal oxygen metabolism. OEF can increase from a baseline of 30% to up to 80%. This situation has been called "misery perfusion"[106].

In this dissertation, SHRsp rats and suture models are used to study chronic hypertension and acute ischemia, separately.

Stroke-prone spontaneous hypertensive rats (SHRsp), established by Okamoto et al.[64], are a suitable experimental model for investigating the pathogenesis of stroke and its treatment measures in humans. In these rats, stroke occurs as a consequence of high blood

pressure and the process is accelerated if the rats are on a specific permissive diet, low in potassium and protein and high in sodium (Japanese permissive diet [JPD]) [65].

In contrast, the suture model is a unilateral, transient MCA occlusion (MCA-O) model, since human focal cerebral infarcts are most frequently found in the middle cerebral artery (MCA) territory, presumably due to the deficient collateral blood supply in this region and the large size of MCA. The MRI changes in the suture occlusion model are very similar to those observed in human brain ischemia.

In both models, after the onset of stroke, the integrity of blood-brain barrier (BBB) is compromised, edema develops, rCBF is altered, and the ability of autoregulation may be lost. However, there are many differences between these two models.

1) CPP is different.

In SHRsp rats, MAP will increase, resulting in an increased CPP, and the process is accelerated when the rats are on a specific permissive diet.

In contrast to chronic hypertension, CPP will fall under the condition of cerebral ischemia.

2) The initiation mechanism of stroke differs.

The underlying physiological mechanisms for developing stroke in SHRsp rats are generally as follows[58, 59, 71, 75]: the BBB in SHRsp is less vulnerable than in normotensive rats to an acute rise in blood pressure, probably due to the structural modifications in the resistant vessels. But severe hypertension (over 200 mmHg) induces the chronic moderate reduction of cerebral blood flow, which causes cerebrovascular damage due to long-term moderate ischemic hypoxia, and results in arterionecrosis. Arterionecrosis is due to the increased vascular permeability and is a common reason for both hemorrhage and infarction. When the

disruption of BBB does occur, high intravascular pressure functions as an effective propulsive force for the extravasation of plasma components through damaged BBB. Endothelial cells and smooth muscle cells in damaged cerebral vessels are replaced by basal membrane and collagenous fiber, yielding necrosis of arterioles. Further damage leads to rupture of microaneurysms formed at the weakened arterionecrotic wall and thrombotic occlusion of aneurismal arterioles, which are hypothesized to be the basis of cerebral hemorrhage and infarct, respectively.

Microaneurysms have been observed in zones of BBB injury, whereas regions without marked BBB leakage show more minor changes. These vascular changes are thought to result from chronic elevation of intraluminal pressure[114].

In contrast, under ischemic condition in suture model, the cell injury depends on the duration and depth of ischemia.

The cerebral blood flow (CBF) threshold is different for cell dysfunction or death under ischemic conditions. It has been shown that when CBF falls below 16 to 18 ml/100g/min, spontaneous and evoked electrical activity ceases, but when CBF falls below 10 to 12 ml/100g/min, cellular ion homeostasis is lost and membrane function collapses. At this point, cells take up Ca^{2+}, with rapid efflux of K^+, and influx of Na^+, Cl^-, and water driven by osmotic pressure. The CBF threshold for cellular energy failure is similar to that for loss of membrane homeostasis. The threshold varies with the duration of the ischemia. Other indices of a perturbed cellular metabolism may not require such a low CBF threshold. For example, extra- and intracellular acidosis occurs at higher CBF values than those associated with energy failure. In addition, edema can develop at higher CBF values (20ml/100g/min)

than those causing loss of ion homeostasis. Finally, protein synthesis is extraordinarily sensitive to a reduction in CBF, thus it has an even higher CBF threshold [6,7].

Under severe ischemic conditions, the permeability of BBB may increase, causing the formation of vasogenic edema.

3) The two models have different nature of edema.

The edema in the SHRsp rats fed with the Japanese diet and exposed to 1% NaCl develops as vasogenic edema (increase in absolute extracellular water content) without the phase of cytotoxic edema (the transfer of water from the extracellular space into the cells due to cellular energy failure) [66].

Ischemic cerebral edema has a characteristic time course. It begins with a cytotoxic phase with the influx of Na^+ and water into the intracellular compartment, the efflux of K^+ into the extracellular compartment, and intact BBB, followed by a vasogenic phase with the disruption of BBB.

4) Autoregulation is altered.

Under hypertension, the autoregulatory mechanisms to maintain constant CBF could be altered. For example, the autoregulatory range can shift to a higher pressure in patients with hypertension. Vessels constrict in response to increased CPP. When blood pressure rises above the upper limit, blood flow increases rapidly and could potentially cause severe overstretching or rupture of cerebral blood vessels, sometimes resulting in serious brain edema or cerebral hemorrhage[102].

Under ischemic conditions, the vessels dilate in response to decreased CPP and autoregulatory control is changed within the ischemic territory[115].

5) The two models have different metabolic abnormalities.

Among the metabolic abnormities found in the SHRsp model, it has been shown that an atypical inflammatory condition[62], proteinuria (protein levels ≥ 40mg/d), precedes cerebral edema identified by T2-weighted MRI in salt-loaded SHRsp rats. When proteinuria exceeded 40mg/day, but before brain abnormalities could be detected by MRI, the protein concentration of CSF increased at least twofold, possibly as a consequence of the altered osmotic balance caused by the high-salt permissive dietary treatment in genetically responsive animals. As soon as MRI detected BBB leaks, massive amounts of plasma proteins entered brain interstitial fluid and CSF compartments.

In contrast, with biochemical/metabolic alterations in areas of focal ischemia, changes in brain metabolites (lactate, pyruvate, c-AMP and ADP) after MCA-O are confined to the corresponding arterial territory[115].

6) The two models have different histochemical changes.

Among the histopathological findings with the SHRsp model[66], histological evaluations of the lesion areas showed that the gray matter was markedly spongy, with loss of neurons, accumulation of astrocytes, and deposition of fibrinoid-eosinophilic material, and the white matter was also characterized by a rarefied texture. The arterioles in the lesions showed vessel wall alterations, with detectable perivascular infiltrates, monocytes-macrophages, and occasionally erythrocytes[66].

In contrast, focal brain ischemia alters the appearance of the neuronal perikaryon, and induces synaptic swelling, astrocytic enlargement, widening of the extracellular space, and possibly axonal enlargement[115].

1.3 Three Parameters

From the previous description, we can see that in addition to inducing extensive physiological alteration, stroke causes extensive remodeling of cerebral vasculature. Usually, the physiological parameters used to describe cerebrovacular physiology include permeability of blood-brain barriers (BBB), cerebral blood flow (CBF), cerebral blood volume (CBV) [3], and blood pressure. These parameters are important for studying the underlying mechanisms of brain injury, staging injury progression, and eventually evaluating and developing therapeutic treatments to brain disorders.

In this study, we focused on the assessment of cerebrovascular alterations under two CPP modulated ischemic conditions: chronic hypertension and transient focal cerebral ischemia via SHRsp rats and the suture model, separately.

Extensive studies have been done with these models, however, there are some areas remaining to be elucidated.

The increased permeability of the BBB, which can result from both hypertension and ischemic conditions, can cause edema. Brain edema leads to increased intracranial pressure (ICP), causing a deterioration of the patient's neurological condition. Therefore, brain edema is among the leading causes of morbidity and mortality in patients with stroke. Therefore, the relationship between permeability and water content was investigated under both hypertension and ischemic conditions in this dissertation.

First, under hypertension, the permeability of the BBB may increase depending on the extent of hypertension, allowing extravasation of small molecules and blood proteins into brain tissue and resulting in damage to neuronal cells, and edema, an accumulation of water in the brain. However, the temporal and spatial relation between the formation of brain edema and the extent to which permeability is altered is poorly understood. Further studies

may shed some light on the roles of BBB breakdown in edema formation, help to evaluate and monitor the effectiveness of therapeutic intervention, and aid the development of new therapies targeted at maintainance of the BBB.

Second, under ischemic conditions, the integrity of the BBB may be compromised depending on the duration and extent of ischemia, resulting in the formation of vasogenic edema. However, the temporal and spatial relationship between the increase in brain water content and the disruption of the BBB has not been studied.

Third, when blood pressure rises above the upper limit, blood flow increases rapidly and could potentially cause severe overstretching or rupture of cerebral blood vessels, sometimes resulting in serious brain edema or cerebral hemorrhage[102]. Accurate early detection of hemorrhage is crucial for the initial evaluation of patients presenting with acute stroke symptoms, since a history of intracerebral hemorrhage is a contradiction of the use of thrombolytic agents. However, whether the presence of hemorrhage is preceded by BBB leakage remains unknown.

Fourth, disease processes involving the central nervous system can cause alterations of CBV. Quantitative measurements of CBV are desirable for the investigation of both the disease process and the therapeutic interventions for various cerebral disorders. With the ability to obtain quantitative measurements of CBV using MRI, it is possible to investigate the dynamic alterations of CBV under hypertension. Furthermore, the relationship between CBV alteration and BBB breakdown in regards to whether the vessel loses its autoregulatory ability before BBB breakdown or vice versa was also investigated in this study.

In summary, the questions we are concerned with include:

1) In SHRsp rats, what is the role of BBB breakdown in the development of edema?

2) In the suture model, what is the role of BBB breakdown in the development of edema?

3) In SHRsp rats, what is the relationship between hemorrhagic transformation and BBB breakdown?

4) In SHRsp rats, how does CBV change with the hypertensive condition?

Therefore, in order to address the proposed Aims (please see below), permeability of the BBB, rat brain water content, and CBV were studied via two experimental animal models including the stroke-prone spontaneous hypertensive rats (SHRsp) model[58-99] and the transient ischemia model[24-36] i.e. the suture model.

1.4 Specific Aims

The specific aims of this dissertation are:

Specific Aim 1: To study the temporal and spatial relationship between brain water content and permeability using the SHRsp model.

The purpose of this study is to investigate the temporal and spatial interplay between brain edema and vascular permeability under the chronic hypertensive condition.

Hypothesis: In SHRsp rats, there is a linear relationship between permeability and water content in edema development.

Null Hypothesis: In SHRsp rats, there is no linear relationship between permeability and water content in edema development.

Specific Aim 2: To study the hemorrhagic transformation in relation to BBB breakdown using the SHRsp model.

The purpose of this study is to verify if hemorrhage is preceded by BBB leakage under the hypertensive condition, such that the hemorrhagic transformation can be predicted by BBB leakage.

Hypothesis: In SHRsp rats, BBB breakdown detected by Gd occurs no later than hemorrhage since Gd is much smaller than red blood cells.

Null Hypothesis: In SHRsp rats, hemorrhage occurs before BBB breakdown detected by Gd.

Specific Aim 3: To examine CBV alterations under hypertension using the SHRsp model.

This aim will focus on the modulation of blood pressure in relation to CBV. The effects of chronic hypertension on cerebral hemodynamics will be assessed using the SHRsp model. The time course of BBB breakdown in relation to CBV alteration under chronic hypertension will also be studied in this aim.

Hypothesis: CBV should decrease under chronic hypertension before BBB breakdown to maintain constant CBF due to the autoregulatory mechanism.

Null Hypothesis: Under hypertensive conditions, there is no CBV change.

Specific Aim 4: To study the temporal and spatial relationship between brain water content and permeability using the suture model.

The purpose of this study is to investigate the temporal and spatial interplay between brain edema and vascular permeability under acute ischemic conditions.

Hypothesis: In the suture model, there is a linear relationship between permeability and water content in edema development.

Null Hypothesis: In the suture model, there is no linear relationship between permeability and water content in the development of edema.

To achieve the above goals, MRI technique was utilized to monitor the temporal evolution of these physiological changes, including the brain water content, vascular

permeability, and CBV. Prerequisite experimental techniques were developed for consistent SHRsp and suture models. MR imaging parameter optimization and advanced image processing methods were employed to extract the information of interest from the two animal models.

1.5 Main Challenges

Many challenges arise due to the complexity of animal experiments, the imperfection of the MRI system, and the limitations of methodologies employed. Examples are as follows:

1) The high variability in lesion size due to the difference in the extent of ischemia during the process of preparation of the suture model;

2) The unpredictable location of the BBB leakage in the rat brain without previous studies;

3) The intra-animal diversity in stroke development among SHRsp rats;

4) The RF inhomogeneity and flip angle miscalibration in MRI system, which reduce the accuracy of absolute water content measurement;

5) The inconsistency of T1 measurement of blood before the injection of contrast agent due to the slow regrowth of longitudinal magnetization resulting from large blood T1 value;

6) The low signal-to-noise ratio in the CBV map due to the selection of AMI227 as the contrast agent, its dose, and the IP injection method;

7) The incompatibility between the permeability measurement and the CBF measurement by the DSC method due to its requirement of injection of the contrast agent though there should not be any contrast agent in the blood before permeability measurement to make sure the uptake process is unidirectional for accurate permeability measurement.

1.6 Major Accomplishments in this Dissertation

To address the above questions it is necessary to develop a spectrum of techniques for use in animal experiments, sequence design and imaging parameter selection for MRI, and post-imaging processing. The major accomplishments include:

1) The employment of the approach proposed by Ramesh Venkatesan[45] for absolute water content measurement, in which the RF inhomogeneity and flip angle miscalibration are compensated for by a theoretical model;

2) The design of two variants of TOMROP[57] sequences for long or short T1 measurement;

3) The measurement of BBB permeability by interpreting the Patlak plot, which charts the relationship between the ratios of the total tissue solute concentration and the arterial plasma concentration-time integral to the plasma solute concentration, respectively;

4) The measurement of CBV by a steady-state method;

5) The employment of the arterial spin labeling method to measure CBF, without the need of contrast agent injection;

6) The design of a UNFOLD[56] sequence for permeability measurement to cover more slices without increasing acquisition time;

7) The design of a PIPS (phase incremented progressive saturation) [118, 121] sequence and the calculation of MT related parameters as a more sensitive way to detect BBB opening.

1.7 Organization of this Dissertation

This dissertation begins with a brief introduction of dissertation related physiology concepts such as stroke, BBB, metabolism and hemodynamics of the brain, SHRsp rats and suture models in Ch. 2.

Ch. 3 gives a brief introduction to basic MR concepts. The basic principles in magnetic resonance include the Larmor equation, spin relaxation, and the Bloch equation,

which are introduced first, followed by a review of magnetic resonance imaging concepts relevant to the proposed studies, including imaging equations, gradient echo and spin echo sequences, k-space coverage, 1D, 2D and 3D imaging approaches, fast imaging methods, and signal and noise in MRI.

The focus of Chapter 4 is to introduce the methods employed in this dissertation including a theoretical model to measure water content, a T-one by multiple readout pulses (TOMROP) sequence to measure T1, a Patlak plot to measure permeability, the UNFOLD (unaliasing by Fourier encoding the overlaps using the temporal dimension) method to cover more slices, the steady-state method to measure CBV, the Dynamic susceptibility contrast (DSC) method to measure CBF and CBV, the continuous arterial spin labeling method to measure CBF, and the PIPS (phase incremented progressive saturation) sequence to measure K_{for}.

Chapter 5 gives the findings on SHRsp rats, including the important role of BBB for edema formation, the vasogenic nature of edema in SHRsp rats, the relationship between BBB breakdown and the presence of hemorrhage, and the decrease of CBV with the symptoms of weight loss/enlarged ventricles.

Chapter 6 describes the findings resulting from studies of suture models of 90 min occlusion, including a biphasic pattern of BBB opening, and a trend of increasing brain water content.

Chapter 7 provides the conclusions and the future research directions.

CHAPTER 2

Physiological Concepts Pertaining to the Proposed Studies

This chapter introduces the physiologic background of stroke, including both BBB and hemodynamics, as well as two animal models of stroke, SHRsp rats and the suture model.

2.1 Stroke

Stroke, also known as “brain attack”, represents a disease of the blood vessels in the brain that typically results in a reduction of, or disruption in, blood flow to the brain. There are two types of stroke based on the underlying causes: ischemic stroke and hemorrhagic stroke. We will first discuss the underlying causes of ischemic stroke followed by hemorrhagic stroke below.

Ischemic stroke, the most common type of stroke, is caused by blockage of an artery or blood vessel. Ischemic strokes can be further subdivided into one of the three types: thrombotic, embolic, and lacunar stroke. Thrombotic or large-artery stroke occurs when an artery to the brain is blocked by a blood clot (a thrombi) as a result of atherosclerosis. Embolic stroke is usually caused by a dislodged blood clot (an embolus) that forms elsewhere, and becomes wedged in an artery after traveling through the blood vessels. In about 15% of embolic stroke, the blood clots result from a rhythm disorder known as atrial fibrillation. Finally, lacunar stroke can be viewed as a subtype of thrombotic stroke.

Cerebral ischemia can also be classified as global or focal. Clinically relevant global ischemia is only temporary as a result of cardiac arrest followed by resuscitation. In focal ischemia, the core has dramatically reduced CBF, but the penumbra is a marginally perfused border zone that receives blood from collaterals. Focal ischemia may be permanent or transient when followed by reperfusion. Reperfusion can either occur spontaneously or through the use of the thrombolytic therapy[4].

Hemorrhagic stroke, on the other hand, is caused by bleeding in the brain from a broken or leaking blood vessel, which can be categorized by: parenchymal, or cerebral, hemorrhagic stroke, subarachnoid hemorrhagic stroke, and arteriovenous malformation (AVM) stroke. Parenchymal hemorrhagic stroke is most often caused by hypertension exerting excessive pressure on arterial walls that are damaged by atherosclerosis. Subarachnoid hemorrhagic stroke usually results from the rupture of an aneurysm- a thin or weak spot in an artery that balloons out and can burst.

Either type of stroke can cause brain cell death, leading to loss of control of certain functions. When neurons and other cellular elements die after severe and prolonged ischemia, such a condition is called infarction. Transient ischemic attack (TIA) is a “mini-stroke”. In a TIA, a short-term reduction in blood flow to the brain causes temporary stroke symptoms, but does not cause permanent brain damage.

Before a stroke can be treated, diagnostic tests must be performed, which may include a neurological exam, blood tests, an electrocardiogram, imaging tests, electrical tests such as an EEG (electroencephalogram) or an evoked response, or blood flow tests such as Doppler ultrasound tests. Imaging tests include CT (computed tomography) scanning and MRI scanning. CT scans are particularly useful for the detection of intracerebral hemorrhage.

Strokes caused by blood clots can be treated with clot-disolving drugs such as rt-PA (recombinant tissue plasminogen activator), which must be given within 3 hours from the start of a stroke to be effective. This time period is therefore called the therapeutic window. Other medicines such as anticoagulants and antiplatelet agents can also be used to treat or to prevent stroke, and sometimes surgery is also employed[4].

2.2 Blood-Brain Barrier (BBB)

The features of the cerebral capillary endothelial cells are distinctly different from those of systemic capillaries. Systemic capillaries have interendothelial clefts, fenestrae, and prominent pinocytotic vesicles, thus allowing relatively nonselective diffusion across the capillary wall. In contrast, the brain capillaries are almost completely surrounded by the astrocyte foot processes and the endothelial cells are relatively lacking in pinocytotic vesicles, which are rich in mitochondria believed to facilitate energy-dependent transport properties, and they are also connected by tight junctions, thus resulting in highly selective transport of water-soluble compounds across the endothelium. This peculiarity has led to the concept of the "blood-brain barrier" (BBB) [102].

In general, the blood-brain barrier is highly permeable to water, carbon dioxide, oxygen, and most lipid-soluble substances such as alcohol and anesthetics, and the exchange of these substances is limited only by the surface area of the blood vessels and by cerebral blood flow. Conversely, the blood-brain barrier is almost totally impermeable to plasma proteins and most non-lipid-soluble large organic molecules. The non lipid-soluble substances must cross by specific carrier-mediated transport systems, such as Glut1 for glucose and the L system, the A system and the ASC system for amino acids[102]. The blood-brain barrier is slightly permeable to electrolytes such as sodium, chloride, and potassium.

Specific ion channels and ion transporters facilitate electrolyte movement across the barrier. For example, the abluminal endothelial pump, Na^+-K^+-ATPase, exchanges extracellular K^+ with intracellular Na^+ in an energy-dependent manner, hence playing an important role in removing extracellular K^+ released during intense neuronal activity.

Blood-brain barrier (BBB) breakdown is a feature of cerebral ischemia, malignant primary tumors, multiple sclerosis, and other neurodegenerative diseases. A leaky BBB allows extravasation of small molecules and blood proteins into brain tissue and accounts for the excessive accumulation of interstitial fluid (vasogenic edema) [110].

Water movement from the capillaries to the extracellular space (ECS) follows the Starling equation[111]

$$J_{cap} = L_{cap}[\{P_{plasma} - P_{tissue}\} - \sigma_{protein}\{\Pi_{protein,plasma} - \Pi_{protein,tissue}\}] \qquad (2.1)$$

where P_{plasma}-P_{tissue} is the hydrostatic pressure difference between plasma and tissue, $\Pi_{protein,plasma} - \Pi_{protein,tissue}$ is the difference in protein osmotic pressure between plasma and tissue, L_{cap} is capillary hydraulic conductivity, J_{cap} is the flux of water from capillary of interest and σ is the osmotic reflection coefficient. σ_{salt} equals 0 at peripheral capillaries since the plasma fluid enters tissue with its normal salt content, while $\sigma_{protein}$ equals 0.93 at peripheral capillaries which means that about 93% of the plasma protein is retained in the vascular bed.

In the brain, due to the presence of the BBB, the blood vessels are essentially impermeable to salts and proteins, therefore, Eq. (2.1) has to be modified to include a potential contribution of a salt gradient as follows[112]:

$$J_{cap} = L_{cap}[\{P_{plasma} - P_{tissue}\} - \sigma_{protein}\{\Pi_{protein,plasma} - \Pi_{protein,tissue}\} - \sigma_{salt}\{\Pi_{salt,plasma} - \Pi_{salt,tissue}\}] \qquad (2.2)$$

where $\sigma_{protein}$ and σ_{salt} are effectively 1.

Any movement of water into the central nerve system (CNS) driven by the blood pressure is immediately opposed by the pressure gradient set up by the proteins and salt retained in the vascular lumen. As soon as $(\Pi_{salt,plasma} - \Pi_{salt,tissue}) + (\Pi_{protein,plasma} - \Pi_{protein,tissue}) > (P_{plasma} - P_{tissue})$, water is forced back into circulation.

This negative feedback control of water flow into the CNS fails as the blood-brain barrier (BBB) breaks down, causing the formation of edema. Essentially, σ_{salt} goes to 0 and $\sigma_{protein}$ may decrease to even less than 0.93 depending on the degree of disruption of the BBB[112].

2.3 Metabolism

Like other tissues, the brain requires oxygen and nutrients to meet its metabolic needs. Practically all of the oxygen consumed by the brain is utilized in the complete oxidation of glucose. Only an extremely small portion of the glucose goes to lactic acid by anaerobic metabolism. The energy thus derived is stored in the cells as high energy phosphate compounds, such as phospho-creatine and adenosine triphosphate, and is released upon demand. Under resting but awake conditions, the metabolism of the brain accounts for about 15 percent of the total metabolism of the body, though the mass of the brain is only about 2 percent of the total body mass[104, 110].

Most of the metabolism of the brain occurs in the neurons, rather than in the glial supportive tissues. The neurons need energy to transport sodium and calcium ions out of the cell and potassium and chloride ions to the interior. When a neuron conducts an action potential, these ions move in the opposite directions, thus increasing the metabolic need to maintain proper ionic concentration differences[110].

However, unlike most tissues of the body, the brain has limited ability to conduct anaerobic metabolism. One of the reasons is that brain cells require far more energy than cells of other tissues due to its high metabolic rate. An additional reason is that the extra stores of glycogen and oxygen in brain tissues are slight. There is only a ~2-minute supply of glucose stored as glycogen in the neurons. Therefore, second-by-second delivery of glucose and oxygen from the blood is needed for proper neuronal activity. This explains why sudden cessation of cerebral blood flow or sudden total lack of oxygen can cause unconsciousness within 5 to 10 seconds[110]. Three factors may lead to decreased brain function: (1) deficit of essential nutrients in arterial blood, (2) restriction of cerebral circulation, or (3) intracellular defects in metabolism[104].

Energy depletion is central to the pathophysiology of ischemic lesions. Failure to maintain cellular adenosine triphosphate (ATP) levels leads to degradation of membrane and cytoskeletal integrity, loss of ion homeostasis, involving cellular accumulation of Ca^{++}, Na^{+}, and Cl^{-}, with osmotically obligated water, and production of metabolic acids[117].

2.4 Circulation in the Human Brain

The brain represents 2% of the body weight, but normally receives about one-sixth of the heart's output of blood and consumes nearly 20% of the oxygen utilized by the whole body[104].

The rate of cerebral blood flow depends on two factors: (1) the pressure in the head, or the difference between the arterial and venous pressures at the level of the cranium, and (2) the resistance, or hindrance of the vessels of the brain[104].

Blood pressure in the head is largely determined by the mean arterial blood pressure. A normal arterial blood pressure is maintained by numerous homeostatic mechanisms such as

the carotid sinus reflex and central control of peripheral vascular tone. When the mean arterial blood pressure is above a critical minimum level, cerebral blood flow is actually regulated intrinsically by changes in cerebrovascular resistance.

Cerebrovascular resistance impedes the flow of blood through the brain, and effectors include intracranial pressure, blood viscosity, organic changes in cerebral vessels, and functional tone of cerebral vessels. These concepts are introduced separately below.

Intracranial pressure: The thin walled vessels of the brain are immersed in cerebrospinal fluid. When the intracranial pressure rises, cerebrovascular resistance increases since these vessels are compressed. Cerebral blood flow is reduced accordingly except that a normal blood flow can be preserved by the rise in blood pressure, which accompanies increased intracranial pressure.

Brain viscosity: The viscocity of the blood is largely dependent on the proportion of erythrocytes. In severe anemia of all types, there is a reduction in resistance and a corresponding increase in blood flow. A normal state of oxygen delivery can be maintained by this compensatory mechanism.

Organic change in cerebral vessels: marked sclerosis and narrowing of the lumen of cerebral arteries and a good deal of parenchymal atrophy usually can be found in the brains of some patients. It has usually been assumed that cerebral arteriosclerosis imposes a resistance to the flow of blood through the brain, causing a decrease in nutrition, which leads to the functional and anatomic changes in the brain substance.

Cerebrovascular tone: By constriction or dilation of the cerebral circulation either locally or generally, a remarkable degree of homeostasis can be maintained. Alterations in

cerebrovascular tone may be achieved by certain neurogenic mechanisms, by humoral agents or by a number of drugs.

In contrast to neurogenic control, chemical substances exert effects upon cerebrovascular tone. Besides carbon dioxide tension, the hydrogen ion concentration is of equal or greater importance and difficult to separate from carbon dioxide tension. Oxygen tension is another important factor in the regulation of cerebrovascular resistance.

To maintain cerebral hemostasis, circulation is adjusted to local metabolic needs. Cerebral blood flow increases with the rise in cerebral metabolism. The fact that at least three products of metabolism (decrease in oxygen tension, increase in hydrogen ion concentration and carbon dioxide tension) are dilators to cerebral vessels suggests these substances are possible agents, which accomplish this adjustment.

In addition to these endogenous substances, numerous drugs, such as histamine, can affect cerebrovascular tone.

Another mechanism to control cerebral blood flow is pressure. Cerebral blood flow can be kept constant between the arterial pressure limits of 60 and 140 mmHg by altering the diameter of the blood vessels, hence changing the fraction of blood volume in brain tissues. This autoregulatory range can shift to 180-200 mmHg in people with hypertension. After the pressure rises above the upper limit, the blood flow increases rapidly and can cause severe overstretching or rupture of cerebral blood vessels, sometimes yielding serious brain edema or cerebral hemorrhage[102].

The autoregulation mechanism is also altered under ischemic conditions. A biphasic CBF pattern during reperfusion--a short-lived reperfusion hyperemia followed by a prolonged post-ischemic hypoperfusion--was observed under transient, severe, non-lethal

global forebrain ischemia (GFI) conditions. In addition, correlative scanning EM studies on the smooth muscle cell surface of arterioles suggest vasodilation during hyperemia and return to their contractile state during hypoperfusion. Capillary narrowing and pericytes detachment were also found during hypoperfusion[109].

From the descriptions above, we can see that stroke can alter the normal function of the brain. The relationship between permeability and water content, and the CBV alterations under both chronic hypertension and acute ischemic conditions, are the focuses of this dissertation. The two conditions are studied with two different animal models: SHRsp rats and the suture model, which are introduced below.

2.5 SHRsp Rats

The stroke-prone spontaneous hypertensive rat (SHRsp) line, established by Okamoto et al.[64], is a suitable experimental model for investigating the pathogenesis of stroke and the effectiveness of various treatment modalities in humans primarily for the following three reasons. First, in these rats, stroke occurs as a consequence of high blood pressure and the process is accelerated if the rats are on a specific permissive diet, low in potassium and protein and high in sodium (Japanese permissive diet [JPD]) [65]. Second, it emphasizes the role of genetic factors in stroke development aside from long-standing hypertension due to the fact that the spontaneously hypertensive rat (SHR) remains stroke free despite a similar degree of hypertension after exposure to JPD. Third, pathological findings of cerebrovascular lesions in SHRsp correspond well to those in humans[146, 147, 149-151]. In SHRsp, stroke often occurs in the anteromedial and occipital cortex and the basal ganglia. The common features at these sites include 1) recurrent branchings, i.e., blood vessels in which the blood flow is

opposite to that of the parent vessels; and 2) the involvement of vascular boundary zone areas. These features suggest obvious parallels with human stroke.

By using this model, the relationship between histopathological findings and behavioral or metabolic abnormalities (e.g., proteinuria, edema development due to BBB damage, increased aggressiveness, hypokinesia or hyperkinesias, a sudden loss of body weight) has been extensively investigated[61-67], and the model has also been utilized to study vascular and brain tissue alterations to understand the mechanism for developing stroke.

Among the histopathological findings with the SHRsp model[66], histological evaluations of the lesion areas showed that the gray matter was markedly spongy, with loss of neurons, accumulation of astrocytes, and deposition of fibrinoid-eosinophilic material, and the white matter was also characterized by a rarefied texture. The arterioles in the lesions showed vessel wall alterations, with detectable perivascular infiltrates, monocyte-macrophages, and occasionally erythrocytes.

Among the metabolic abnormities found in the SHRsp model, it has been shown that an atypical inflammatory condition[62], proteinuria (protein levels $\geq$ 40mg/d), precedes cerebral edema as identified by T2-weighted MRI in salt-loaded SHRsp rats. When proteinuria exceeded 40mg/day, but before the appearance of brain abnormalities detected by MRI, the protein concentration of CSF increased at least twofold, possibly as a consequence of the altered osmotic balance caused by the high-salt permissive dietary treatment in genetically responsive animals. As soon as MRI detected BBB leaks, massive amounts of plasma proteins entered the brain interstitial fluid and CSF compartments[61-62]. It has also been reported that the edema in the SHRsp rats fed with the Japanese diet and exposed to 1% NaCl develops as vasogenic edema (increase in absolute extracellular water content) without

the phase of the cytotoxic edema[66] (the transfer of water from the extracellular space into the cells due to cellular energy failure).

The underlying physiological mechanisms for developing stroke in SHRsp rats are generally as follows[58, 59, 71, 75]: the BBB in SHRsp is less vulnerable than in normotensive rats to an acute rise in blood pressure, probably due to the structural modifications in the resistant vessels. But, severe hypertension (over 200 mmHg) induces the chronic, moderate reduction of cerebral blood flow, which causes increased cerebrovascular permeability due to long-termed moderate ischemic hypoxia. When the disruption of BBB does occur, high intravascular pressure functions as an effective propulsive force for the extravasation of plasma components through damaged BBB. Endothelial cells and smooth muscle cells in damaged cerebral vessels are replaced by basal membrane and collagenous fibers, yielding necrosis of arterioles. Further damage leads to rupture of arteriolar aneurysms and thrombotic occlusion of aneurismal arterioles, which are hypothesized to be the basis of cerebral hemorrhage and infarct, respectively.

Microaneurysms have been observed in zones of BBB injury, whereas regions without marked BBB leakage show more minor changes. The pathogenesis of these vascular changes is thought to result from chronic elevation of intraluminal pressure[114].

2.6 The Suture Model

Human focal cerebral infarcts are most frequently found in the middle cerebral artery (MCA) territory, presumably due to the deficient collateral blood supply in this region and the large size of MCA. Therefore, focal ischemia models most often involve unilateral, transient, or permanent MCA occlusion (MCA-O). The positions of the main arteries associated with stroke are shown in Fig. 2.1[42]. The MRI changes in the suture occlusion

model are very similar to those observed in human brain ischemia. The details of the suture model have been described elsewhere [37]. A brief description of the surgical procedure for the suture model is given below.

The right common carotid artery and external carotid artery are exposed through a ventral midline incision. After the right proximal external carotid artery is permanently ligated, a 4-0 nylon monofilament is advanced into the internal carotid artery through an arteriotomy of the common carotid artery ~3mm below the carotid bifurcation, roughly 20-22 mm until reaching the proximal anterior cerebral artery to block the origin of the MCA. Ischemia lasts 90 minutes by keeping the suture in place and reperfusion is achieved by withdrawing the suture from the internal carotid artery to the common carotid artery. The reason for the 90-minute duration of ischemia is that reperfusion after temporary middle cerebral artery occlusion is still helpful for the survival of the penumbral zone for up to 90 minutes[35].

The suture model may produce varying volumes of infarction, depending upon the rat strain, body weight, and the extent of insertion of the suture. A poly-L-lysine coated suture can reduce variability. However, the rats can be divided into different groups based on the size of final lesion for statistical analysis.

The extent of cell injury depends on the duration and depth of ischemia.

The CBF threshold is different for cell dysfunction or death under ischemic conditions. It has been shown that when CBF falls below 16 to 18 ml/100g/min, spontaneous and evoked electrical activity ceases, but when CBF falls below 10 to 12 ml/100g/min, cellular ion homeostasis is lost and membrane function collapses. At this point cells take up Ca^{2+} with rapid efflux of K^+, and influx of Na^+, Cl^-, and water driven by osmotic pressure.

The CBF threshold for cellular energy failure is similar to that for loss of membrane homeostasis, however, it varies with the duration of the ischemia. Other indices of perturbed cellular metabolism may not require such a low CBF threshold. For example, extra- and intracellular acidosis occurs at higher CBF values than those associated with energy failure. In addition, edema can develop at higher CBF values (20ml/100g/min) than those causing loss of ion homeostasis. Finally, protein synthesis is extraordinarily sensitive to a reduction in CBF, thus it reflects an even higher CBF threshold [6,7].

Generally, the ischemic injury happens as follows[117]:

Lack of oxygen causes the failure of the neuron's normal process for making ATP, causing the cell to switch to anaerobic metabolism, producing lactic acid. ATP-reliant ion transport pumps fail, allowing ions, including Ca^{++}, to flow into the cell. The intracellular calcium levels get too high since the ion pumps can no longer transport calcium out of the cell. The presence of calcium triggers the release of glutamate, which stimulates glutamate receptors to allow more calcium into cells. Excess calcium overexcites cells and causes the generation of harmful chemicals like free radicals, calcium-dependent enzymes such as ATPase, and phospholipases.

Phospholipases can break down the cell's membrane, allowing more ions and harmful chemicals to flow into the cell. Toxic and apoptotic factors are released into the cell by mitochodria breakdown. The apoptosis cascade causes cells to begin the process of programmed cell death. If the cell dies via necrosis, it releases glutamate, which overexcites nearby neurons, and toxic chemicals, which poison nearby neurons.

After the withdrawal of the suture, blood flow is restored to the brain. The role of reperfusion is two-fold[33]: on the one hand, it restores the delivery of oxygen and glucose to

the tissue, but on the other hand, it can also cause further tissue damage via delayed or secondary injury. Reperfusion may aggravate brain injury by three mechanisms: by restoration of the supply of water and osmotic equivalents, thus exacerbating edema; by the re-establishing the supply of oxygen after the period of ischemia, accelerating the formation of oxygen free radicals; and by the release of a variety of biomedical mediators associated with edema or infarction from neurons or endothelial cells. A free radical prefers to steal electrons from the lipid membrane of a cell, initiating a free radical attack on the cell known as lipid peroxidation.

The initial period of recirculation after ischemia is important for the development of stroke. The 'no-reflow phenomenon' and 'hyperemia-hypoperfusion' are the two patterns of post-ischemic circulatory disturbance[25, 29, 32-34].

After reperfusion, the integrity of the BBB may be compromised, thus resulting in significant brain edema and infarction. Ischemic cerebral edema has a characteristic time course. It begins with a cytotoxic phase with the influx of Na^+ and water into the intrcellular compartment, the efflux of K^+ into the extracellular compartment, and intact BBB, followed by a vasogenic phase with the disruption of BBB. However, the role of the breakdown of the BBB's inpermeability to proteins in relation to accumulation of fluid remains to be determined[33, 34].

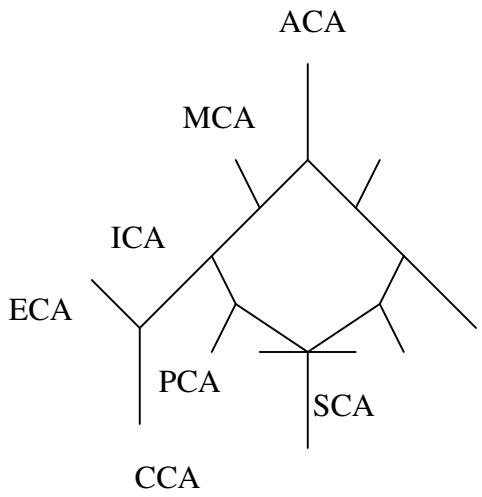

Figure 2.1: Schematic representation of the positions of the main arteries. ACA, anterior cerebral artery; PCA, posterior cerebral artery; MCA, middle cerebral artery; SCA, superior cerebellar artery; CCA, common carotid artery; ECA, external carotid artery; ICA, internal carotid artery.

CHAPTER 3

Physical Principles of Magnetic Resonance

The purpose of this chapter is to provide an overview of the theory of MRI and to introduce some important concepts related to this dissertation. It begins with the motion of a single proton, followed by the formation of an image. Finally, some important dissertation related concepts are introduced.

3.1 Principles of Magnetic Resonance

MRI is based on the interaction of a nuclear spin with an external magnetic field. Only nuclei with nonzero intrinsic angular momentum (total 'spin') can be imaged. Given its '1/2' spin and its abundance in human body, the dominant nucleus in MRI is the hydrogen proton. Hydrogen is the dominant nucleus in MRI, and its interaction with the external field results in the precession of the proton spin about the field direction. The precession is governed by the fundamental equation of motion,

$$\frac{d\vec{\mu}}{dt} = \gamma\vec{\mu} \times \vec{B} \qquad (3.1)$$

where $\vec{\mu}$ is the magnetic moment; γ is the gyromagnetic ratio, which is a constant and equals to 2.675×10^8 rad/T/sec for proton; and $\vec{B}$ is the main magnetic field strength in Tesla.

The frequency of the precession is proportional to the strength of the magnetic field and depends on the nucleus type. It can be expressed by the Larmor equation,

$$\vec{\varpi}_0 = -\gamma \cdot \vec{B}_0 \tag{3.2}$$

where $\vec{\varpi}_0$ is the Larmor frequency in rad/sec, and $\vec{B}_0$ is the main magnetic field strength in Tesla.

The equation of motion in the rotating reference frame, which rotates clockwise around the z axis with respect to the laboratory reference frame, for a spin immersed in the combination of the constant field $\vec{B}_0 = B_0\vec{z}$ and RF field with frequency ϖ is

$$\left(\frac{d\vec{\mu}}{dt}\right)' = \vec{\mu} \times [\vec{z}'(\varpi_0 - \varpi) + \vec{x}'\varpi_1]$$

$$= \gamma\vec{\mu} \times \vec{B}_{eff} \tag{3.3}$$

where the spin precession frequency $\varpi_1 = \gamma B_1$.

The effective magnetic field is

$$\vec{B}_{eff} = [\vec{z}'(\varpi_0 - \varpi) + \vec{x}'\varpi_1]/\gamma \tag{3.4}$$

Thus far, only the motion of a single magnetic moment is discussed. But the proton spin interacts with its neighboring atoms, resulting in important modifications to this behavior.

For images of a macroscopic body, the average magnetic dipole moment density (magnetization) has to be introduced to model these modifications. The magnetization is

$$\vec{M} = \frac{1}{V}\sum_{proton\,\sin V}\vec{\mu}_i \tag{3.5}$$

In contrast to a given magnetic moment, the magnitude of the macroscopic magnetization is not fixed, since it is the vector sum of many proton spins involved in both spin-lattice interactions and spin-spin interactions.

3.2 Spin-Lattice Interaction and Spin-Spin Interaction

In spin-lattice interaction, the moments try to align with the external field through the exchange of energy with the surroundings and the rate of the longitudinal magnetization is represented by

$$\frac{dM_z}{dt} = \frac{1}{T_1}(M_0 - M_z) \tag{3.6}$$

where T_1 is the experimental 'spin-lattice' relaxation time.

In spin-spin interaction, the individual spins in the transverse plane tend to fan out in time since the spins experience local fields, which are combinations of the applied field and the fields of their neighbors, and thus precess with different local precession frequencies. The 'fanning out' is referred to as 'dephasing', and the reduction in transverse magnetization in the rotating reference frame is given by

$$\left(\frac{d\vec{M}_\perp}{dt}\right)' = -\frac{1}{T_2}\vec{M}_\perp \tag{3.7}$$

where T_2 is the 'spin-spin' relaxation time.

In practice, there is an additional dephasing of the magnetization introduced by external field inhomogeneities with a separate decay time T_2' to characterize the reduction. Thus the overall relaxation time

$$\frac{1}{T_2^*} = \frac{1}{T_2} + \frac{1}{T_2'} \tag{3.8}$$

The loss of transverse magnetization due to T_2' can be recovered.

After introducing all of the related parameters, now the change of magnetization in the presence of a magnetic field and with relaxation terms is given by the Bloch equation,

$$\frac{d\vec{M}}{dt} = \gamma\vec{M} \times \vec{B}_{ext} + \frac{1}{T_1}(M_0 - M_z)\vec{z} - \frac{1}{T_2}\vec{M}_\perp \tag{3.9}$$

where $\vec{B}_{ext} = B_0\vec{z} + B_1\vec{x}'$ when an rf field $B_1\vec{x}'$ is added to the static field.

3.3 Signal Detection

A change in its magnetic flux environment induces the emf in a coil, which can be calculated by Faraday's law of induction. For precessing magnetization, the transverse magnetization induces the dominant signal in the receive coil. Therefore, the magnitude of the transverse magnetization $M_\perp = \sqrt{M_x^2 + M_y^2}$ is referred to as the 'signal'.

With the neglect of relaxation effects, the complex demodulated signal can be given as

$$s(t) = \varpi_0 \Lambda B_\perp \int d^3 r M_\perp(\vec{r},0) e^{i(\Omega t + \phi(\vec{r},t))} \tag{3.10}$$

where Λ is a constant which includes the gain factors from the electronic detection system, $B_\perp$ is the receive field amplitude, and Ω is the demodulation frequency (with no offset, $\Omega = \varpi_0$). The angle ϕ is the accumulated phase

$$\phi(\vec{r},t) = -\int_0^t dt' \varpi(\vec{r},t') \tag{3.11}$$

where $\varpi(\vec{r},t') = \varpi_0$ only if there is a uniform static field. The signal can be written as

$$s(t) = \int d^3 \rho(\vec{r}) e^{i(\Omega t + \phi(\vec{r},t))} \tag{3.12}$$

where the effective spin density $\rho(\vec{r})$ is introduced as

$$\rho(\vec{r}) = \varpi_0 \Lambda B_\perp M_0(\vec{r}) \tag{3.13}$$

When the phase factor depends only on one dimension, for example, the z coordinate, the signal can be written as

$$s(t) = \int dz \rho(z) e^{i(\Omega t + \phi(z,t))} \tag{3.14}$$

where $\rho(z) = \iint dxdy\rho(\vec{r})$.

3.4 Spatial Localization of the Spins

Since the object of imaging is to determine the spin density $\rho(z)$ of a sample from the measurement of the signal, the spin position has to be connected to the signal.

If a linearly varying field is added to the static field, then the z-component of the field is

$$B_z(z,t) = B_0 + zG_z(t), \tag{3.15}$$

where G_z is the constant gradient in the z-direction

$G_z = \partial B_z / \partial z$.

Then the variation in the angular frequency of the spins is

$$\varpi(z,t) = \varpi_0 + \varpi_G(z,t) \tag{3.16}$$

where $\varpi_G(z,t) = \gamma z G(t)$.

Now the relation between the position of spins along one direction and their precession rates is established by the use of a gradient, leading to the concept of so-called frequency encoding along that direction.

The accumulated phase due to the applied gradient is

$$\varphi_G(z,t) = -\int_0^t dt' \varpi_G(z,t')$$

$$= -\gamma z \int_0^t dt' G(t') \tag{3.17}$$

Then s (t) can be written as

$$s(t) = \int dz\rho(z)e^{i\varphi_G(z,t)} \tag{3.18}$$

The signal can also be given by

$$s(k) = \int dz\rho(z)e^{-i2\pi kz} \tag{3.19}$$

where $k(t) = \gamma\int_0^t dt' G(t')$

This expression shows that, when the static field is augmented by linear gradients, the signal s(k) is the Fourier transform of the spin density of the sample. On the other hand, the spin density of the sample can be obtained by taking the inverse Fourier transform of the signal

$$\rho(z) = \int dk s(k)e^{+i2\pi kz} \tag{3.20}$$

The signal s(k) and the image $\rho(z)$ are a 'Fourier transform pair'.

The extension of the one-dimensional imaging equation to all three spatial dimensions is given by

$$s(k_x, k_y, k_z) = \iiint dxdydz\rho(x, y, z)e^{-i2\pi(k_x x + k_y y + k_z z)} \tag{3.21}$$

where $k_x(t) = \gamma\int_0^t G_x(t')dt'$, $k_y(t) = \gamma\int_0^t G_y(t')dt'$, $k_z(t) = \gamma\int_0^t G_z(t')dt'$

In order to reconstruct the image by (3.21), the signal needs to be collected over a sufficiently large set of k values, i.e., 'good coverage' of k-space is required. A detailed description of how the k-space data is collected in 2D and 3D imaging is given in the next section.

3.5 Sequence Diagram

3.5.1 2D Gradient Echo Imaging

A typical 2D gradient echo sequence diagram is shown in Fig. 3.1.

In this case, a single thin slice extending from $z_0 - \Delta z/2$ to $z_0 + \Delta z/2$ is excited by using a combination of slice selection gradient $G_{z,ss}$ and rf pulse.

The frequency at position z is

$$f(z) = f_0 + \gamma G_z z \tag{3.22}$$

where $f_0 = \gamma B_0$ is the Larmor precession frequency.

So the frequency for the slice after encoding with $G_{z,ss}$ ranges from $(\gamma G_z z_0 + \gamma G_z \Delta z/2)$ to $(\gamma G_z z_0 - \gamma G_z \Delta z/2)$. Thus the frequency profile of the rf pulse, in the rotating frame, should be unity over the range Δf from $(\gamma G_z z_0 + \gamma G_z \Delta z/2)$ to $(\gamma G_z z_0 - \gamma G_z \Delta z/2)$, and zero outside.

The bandwidth BW_{rf} of the rf pulse is given by

$$\begin{aligned} BW_{rf} &= \Delta f \\ &= (\gamma G_z z_0 + \gamma G_z \Delta z/2) - (\gamma G_z z_0 - \gamma G_z \Delta z/2) \\ &= \gamma G_z \Delta z \end{aligned} \tag{3.23}$$

In fact Δz is the slice thickness, TH, of the excited slice. Therefore TH can be given by

$$TH = \frac{BW_{rf}}{\gamma G_z} \tag{3.24}$$

As described above, the frequency profile of the rf pulse is a boxcar function, that is, rect $(f/\Delta f)$ of bandwidth Δf. Therefore, the temporal envelope of the rf pulse $B_1(t)$, which is the inverse transform of the frequency profile, is a sinc function,

$$B_1(t) \propto \sin c(\pi \Delta f t) \tag{3.25}$$

The rf pulse oscillates in the laboratory frame with its amplitude modulated with the sinc envelope. The first zero crossing of the expression occurs at a time $t_1=1/\Delta f$, therefore the total number of zero crossings of the rf pulse with duration τ_{rf} is given by

$$n_{zc} = [\tau_{rf} / t_1] = [\Delta f \tau_{rf}] \tag{3.26}$$

where [] means the operation ' largest integer less than or equal to'. The more zero crossings, the closer the excitation profile approaches the ideal boxcar.

Consider the slice is excited instantaneously at t=0 in the midst of a constant gradient, Gz=Gss, then the transverse magnetization gains phase at the time t in the rotating frame, given by

$$\phi(z,t) = -\gamma G_{ss} z t \tag{3.27}$$

If the spin density is taken as a constant over thin slices, the signal can be written as

$$s(t) \approx \rho(z_0) \int_{z_0-\frac{\Delta z}{2}}^{z_0+\frac{\Delta z}{2}} e^{i\phi(z,t)} dz \tag{3.28}$$

The integral reduces to zero as time progresses, since spins at different z positions accumulate different phases. Therefore, a negative gradient with magnitude Gss, and duration τ_{rf} /2 is turned on to rephrase the signal, though this gradient has nothing to do with slice selection.

After the slice is excited, phase encoding along the y direction and frequency encoding along the x direction are turned on subsequently to cover the whole k-space. How the k-space is covered is given to full length below.

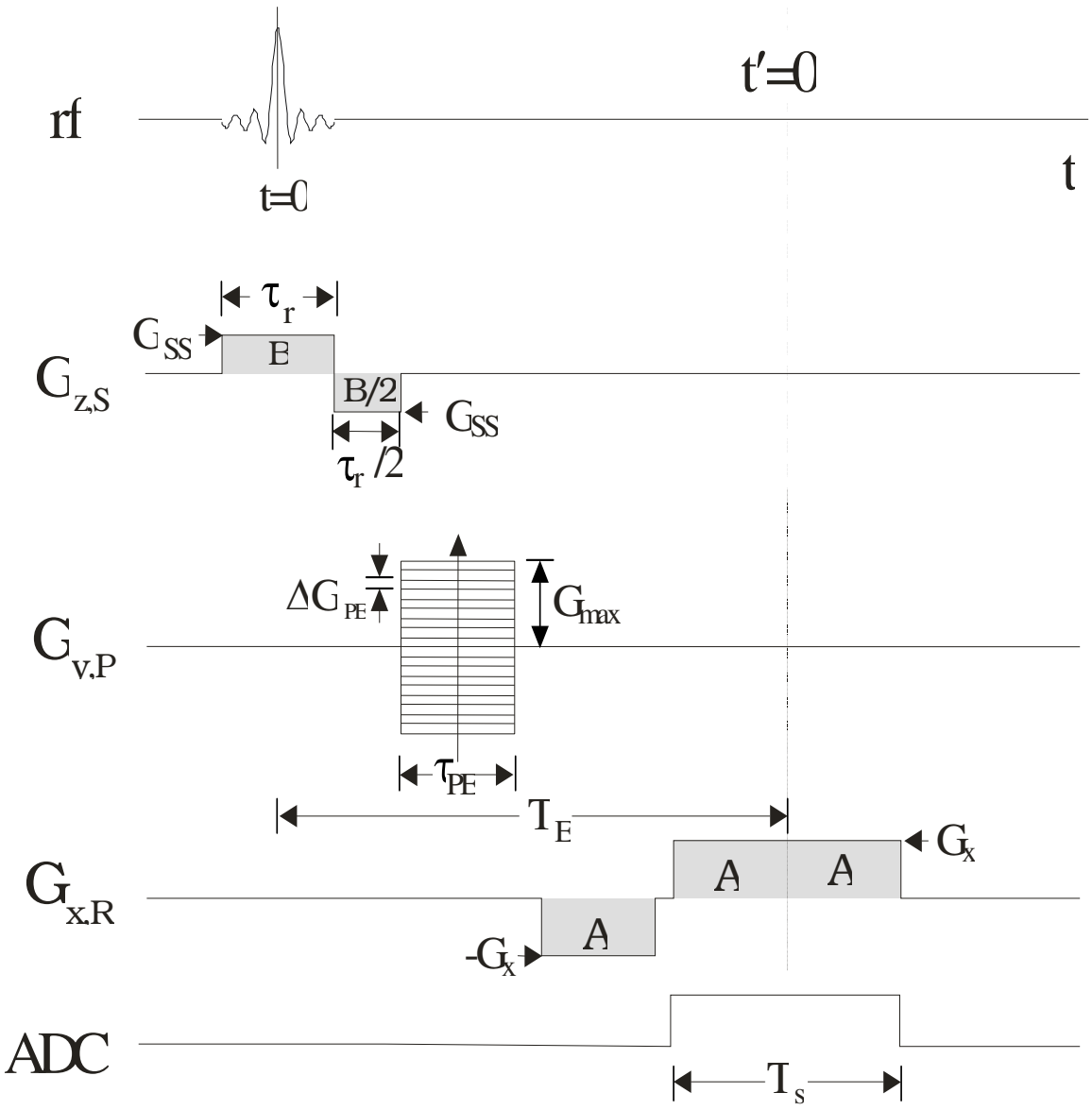

Figure 3.1: Sequence diagram for a 2D gradient echo imaging sequence.

Signal is sampled during ADC on time. In order to reconstruct the image of the spin density, sufficient k_x, k_y values are required. Given the k coverage diagram shown in Fig. 3.2, starting from $k_{PE,\,min}$, $k_{R,\,min}$, one horizontal k_x line, including N_x points separated by Δk_x is collected. Due to the relaxation effects, only one line is collected during one TR, which is the repetition time of one excitation cycle. Next, starting from ($k_{PE,\,min} + \Delta$Ky), $k_{R,\,min}$, another horizontal k_x line is collected, and so on, until a total of N_y lines are collected. Given the parameters shown in Fig. 3.1, $k_{PE,\max} = \gamma G_{y,\max}\tau_y$, $k_{R,\max} = \gamma G_x T_s / 2$, $\Delta k_x = \gamma G_x \Delta t$,

$\Delta k_y = \gamma \Delta G_y \tau_y$. Thus, the total acquisition time in this case is

$T_{acq} = N_y TR$. (3.29)

TE is the time where $k_x=0$, $k_y=0$, and therefore of great importance in determining the signal. Furthermore, the sampling of the k-space is determined by the Nyquist criterion, given by

$\Delta k_x = 1/FOV_x$,

$\Delta k_y = 1/FOV_y$. (3.30)

FOV should be larger than the size of the object to avoid aliasing.

3.5.2 Spin Echo Example

Fig. 3.3 shows the sequence diagram for a 2D spin echo imaging sequence. We focus on four aspects of this sequence. First, no rephrasing gradient for the application of the π pulse is needed since the π pulse, as a symmetric slice gradient, is self-refocusing. Second, the phase is reversed after the application of the π pulse. Third, the signal decay due to T2' effect can be recovered with this sequence. The mechanism is discussed with the phase argument below.

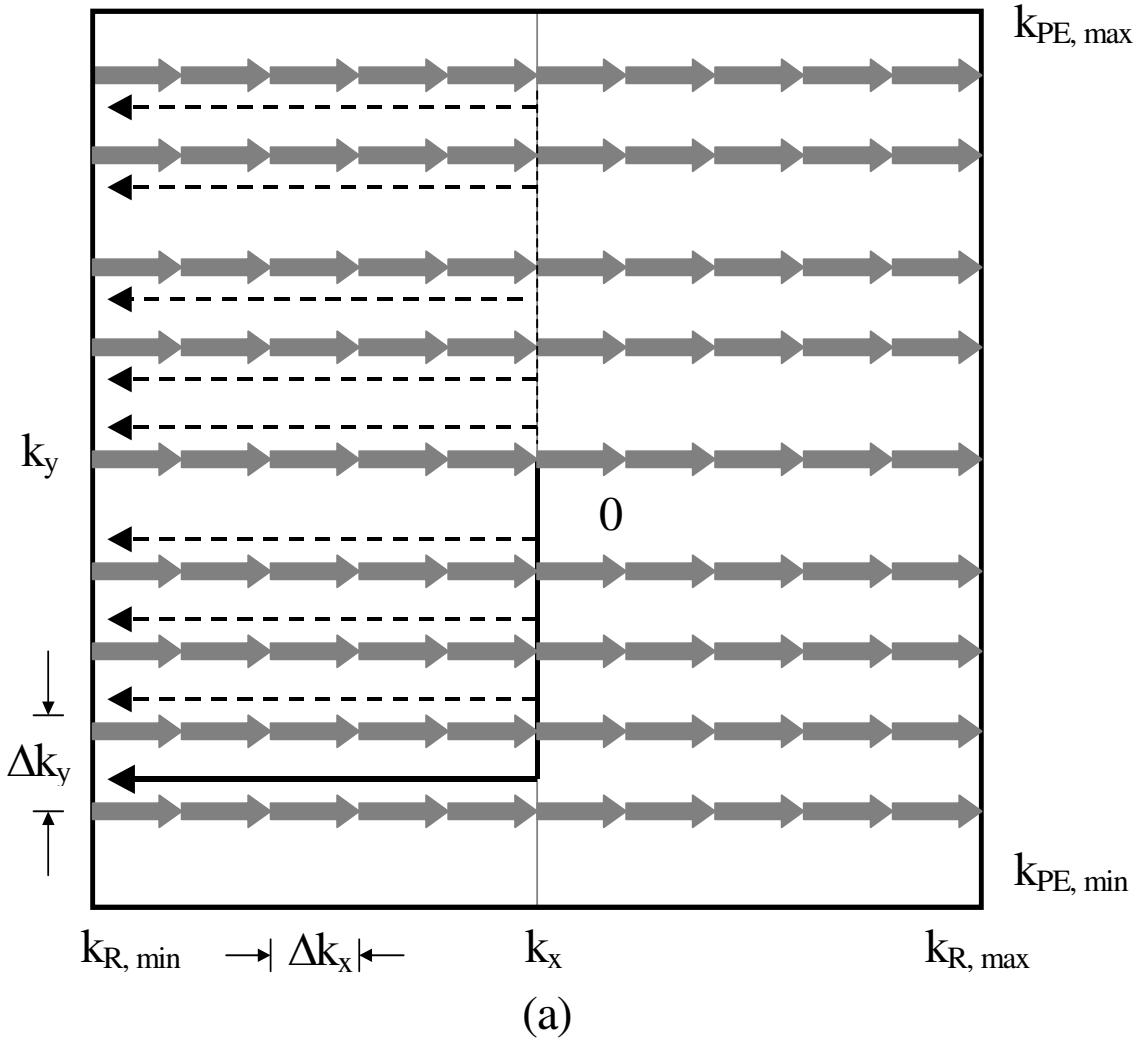

Figure 3.2: Traversal of k-space for the sequence shown in Fig. 3.1.

Assume the time interval between $\pi/2$ pulse and π pulse is τ, then the phase ϕ in the rotating frame relative to the y'-axis is

$$\phi(\vec{r},t) = -\gamma\Delta B(\vec{r})t \qquad \text{for } 0 < t < \tau \tag{3.31}$$

with $\phi_0 = 0$.

The second pulse rotates the spins about the y'-axis through the angle π at time τ,

$$\begin{aligned}&\phi(\vec{r},\tau^+) = -\phi(\vec{r},\tau^-)\\ &= \gamma\Delta B(\vec{r})\tau\end{aligned} \tag{3.32}$$

After time τ,

$$\begin{aligned}&\phi(\vec{r},t) = -\phi(\vec{r},\tau^+) - \gamma\Delta B(\vec{r})(t-\tau)\\ &= -\gamma\Delta B(\vec{r})(t-2\tau)\\ &= -\gamma\Delta B(\vec{r})(t-TE),\end{aligned} \tag{3.33}$$

with the echo time defined by $\mathrm{TE} \equiv 2\tau$.

This equation shows that the accumulated phase of all spins will return to zero at t=TE, regardless of the time-independent field variation ΔB and the position $\vec{r}$. The realignment of the spins is called a spin echo.

Finally, the spin echo signal is written as

$$M_\perp \approx M_0(1 - e^{-TR/T_1})e^{-TE/T_2} \tag{3.34}$$

3.5.3 3D Volume Imaging

Fig. 3.4 shows a 3D gradient echo imaging sequence. Compared with a 2D sequence, a thick slab of volume is excited in 3D imaging rather than a thin slice. Then the slab is phase encoded by adding a gradient table along the slice selection direction. The process of phase encoding along the slice selection direction is also known as partition encoding.

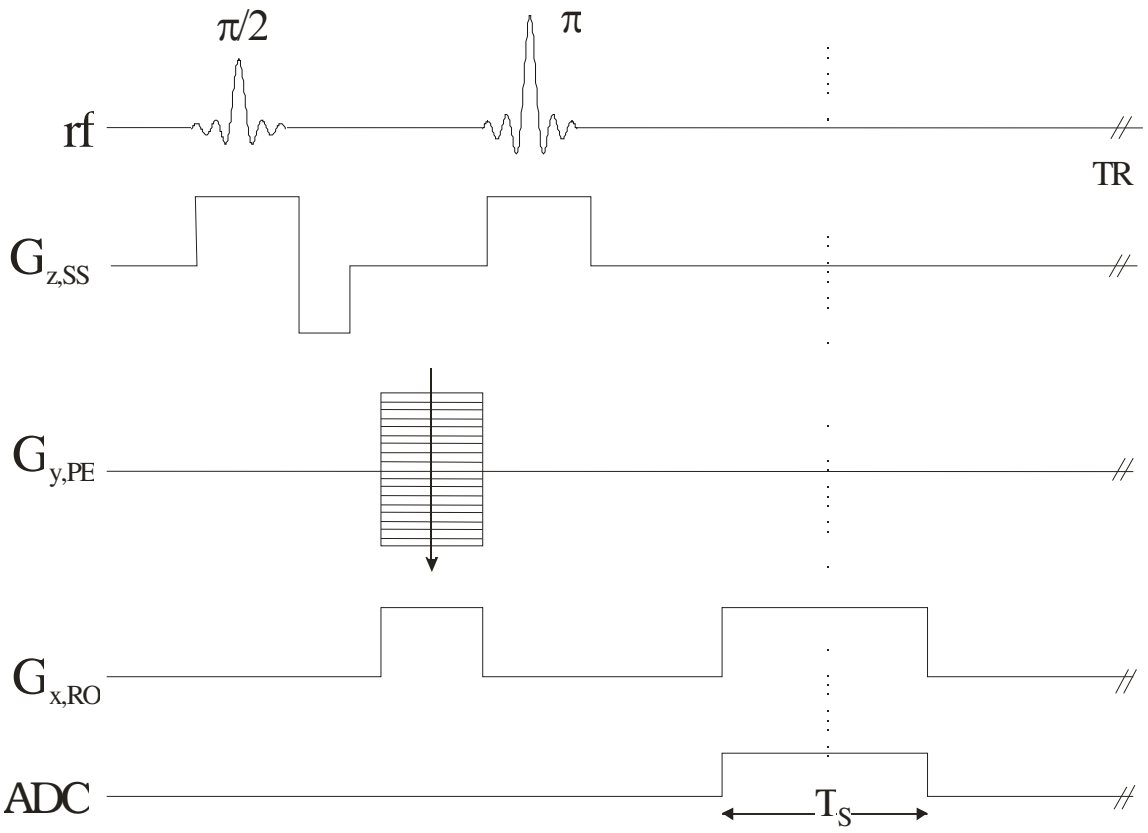

Figure 3.3: The sequence diagram for a 2D spin echo imaging sequence

The excited slice is usually called a slab (with a thickness TH) and the reconstructed multiple slices (with a thickness Δz =TH/Nz) are known as partitions. After the rf pulse excites the same slab, then a different slice position is encoded by the phase encoding table. Thus the total acquisition time is $T_{acq}=N_zN_yTR$.

There are several advantages to collecting data with a 3D volume method in comparison with 2D multi-slice imaging. First, the partition thickness $z=TH/N_z$ can be changed by changing N_z without any limitation of the rf amplitude or duration. Second, consecutive slices can be adjacent. In contrast, there is always a slice gap in practice in 2D imaging since an imperfect rf pulse profile leads to cross-talk between neighboring slices. Third, a larger rf bandwidth can be used for thicker slabs in 3D imaging, thus TE can be reduced with a shorter rf pulse duration. Fourth, signal loss due to T2* dephasing can be reduced with short TE and high spatial resolution in the partition encoding direction. Fifth, the signal-to-noise ratio can be enhanced at the expense of increased imaging time.

3.6 Signal, Noise, and Contrast

The signal-to-noise ratio (SNR) is studied in detail in this section. Contrast-to-noise ratio (CNR) and visibility concepts and three important types of contrast are introduced.

The voxel signal S is proportional to its volume $\Delta x\Delta y\Delta z$, given as

$$S \propto \Delta x\Delta y\Delta z \tag{3.35}$$

The variance of the fluctuating noise in the raw data is given by

$$\sigma_m^2 \propto 4KT \cdot R \cdot BW \tag{3.36}$$

where K is Boltzmann constant, T is absolute temperature, R is the effective resistance of the coil loaded by the body, and BW is the bandwidth of the detecting system. The noise

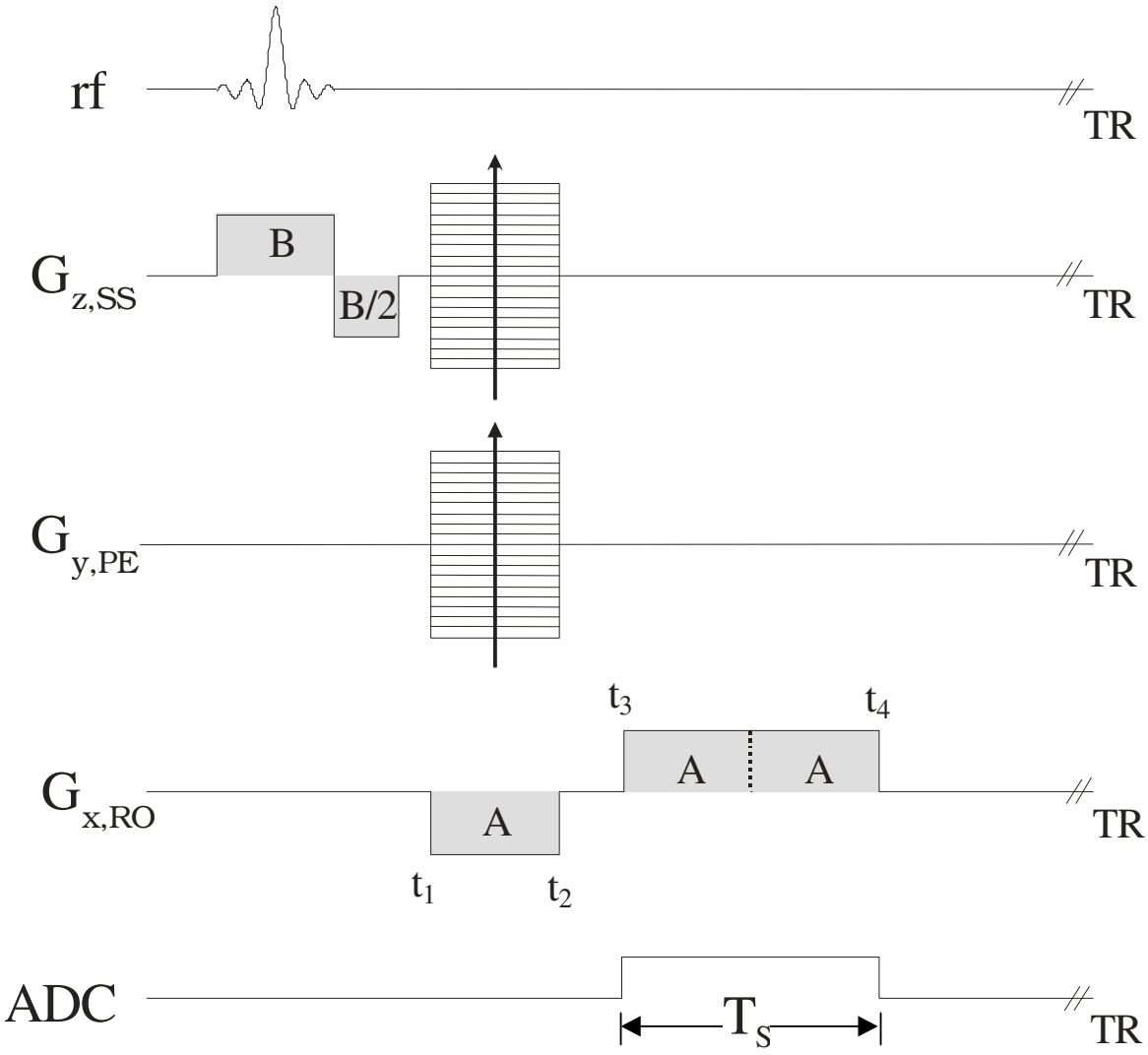

Figure 3.4: A 3D gradient echo imaging sequence in which the two directions orthogonal to the read direction are phase encoded.

variance in the image domain is smaller than that in the detected signal and is the same for all voxels, given by

$$\sigma_0^2 = \frac{\sigma_m^2}{N_x N_y N_z} \tag{3.37}$$

In practice, σ_0 is measured by measuring the mean or standard deviation of a region-of-interest outside the object where there is no signal. The voxel signal here is 'Rayleigh distributed' in the magnitude image, with its mean and standard deviation as $1.253\sigma_0$ and $0.665\sigma_0$, respectively[159].

The probability distribution p(x) for Rayleigh distribution[159] is given by

$$p(x) = \frac{1}{\sigma^2} x e^{-x^2/2\sigma^2} \tag{3.38}$$

In addition, repeating an imaging experiment N_{acq} times and averaging the signal over these N_{acq} measurements results in SNR improvement as the square root of the number of acquisitions N_{acq} if the noise is uncorrelated from one experiment to the next.

From (3.35), (3.36), and (3.37), SNR can be given by

$$SNR/voxel \propto \frac{\Delta x \Delta y \Delta z \sqrt{N_{acq}}}{\sqrt{\frac{BW_{read}}{N_x N_y N_z}}} \tag{3.39}$$

Or $$SNR/voxel \propto \Delta x \Delta y \Delta z \sqrt{N_{acq} N_x N_y N_z \Delta t} \tag{3.40}$$

where $\Delta t = \frac{1}{BW_{read}}$

Or $$SNR/voxel \propto \Delta x \Delta y \Delta z \sqrt{N_{acq} N_y N_z T_s} \tag{3.41}$$

where $Ts = N_x \Delta t$.

Though the imaging parameters may be varied, the following relations hold all the time:

(a) $L_x = N_x \Delta x$

(b) $L_y = N_y \Delta y$

(c) $Lz_x = N_z \Delta z$

(d) $T_s = N_x \Delta t$

(e) $BW_{read} = \dfrac{1}{\Delta t} = \gamma G_x L_x$

(f) $BW / voxel = BW_{read} / N_x$ (3.42)

In a useful image, to distinguish different tissues depends on the contrast-to-noise ratio CNR:

$$CNR_{AB} = \frac{C_{AB}}{\sigma_0} = \frac{S_A - S_B}{\sigma_0} = SNR_A - SNR_B \quad (3.43)$$

The probability that two tissues are different is 95% if CNR_{AB} equals 2 and is 99% when CNR_{AB} equals 3.

Numerous contrast mechanisms, such as flow, magnetic susceptibility differences, magnetization transfer contrast, etc., can be obtained with MRI by manipulating the tissue signal, but the most basic ones are based on spin density, and T1 and T2 differences between tissues as discussed below.

In a 90^0 flip angle gradient echo experiment, the contrast between tissue A and B is

$$C_{AB} = S_A(TE) - S_B(TE) = \rho_{0,A}(1 - e^{-TR/T_{1,A}})e^{-TE/T^*_{2,A}} - \rho_{0,B}(1 - e^{-TR/T_{1,B}})e^{-TE/T^*_{2,B}} \quad (3.44)$$

Under the conditions

$$TE << T^*_{2A,B} \Rightarrow e^{-TE/T^*_2} \to 1$$

$$TR >> T_{1A,B} \Rightarrow e^{-TR/T_1} \to 0$$

C_{AB} becomes

$$C_{AB} = (\rho_{0,A} - \rho_{0,B}) - \rho_{0,A}(e^{-TR/T_{1,A}} + \frac{TE}{T^*_{2,A}}) + \rho_{0,B}(e^{-TR/T_{1,B}} + \frac{TE}{T^*_{2,B}})$$

+higher order and cross terms

$$\approx \rho_{0,A} - \rho_{0,B} \quad (3.45)$$

Thus yielding the spin density weighted contrast.

Under the conditions

$$TE << T^*_{2A,B} \Rightarrow e^{-TE/T^*_2} \to 1$$

C_{AB} is now

$$C_{AB} = S_A(TE) - S_B(TE)$$

$$\approx \rho_{0,A}(1 - e^{-TR/T_{1,A}}) - \rho_{0,B}(1 - e^{-TR/T_{1,B}})$$

$$= (\rho_{0,A} - \rho_{0,B}) - (\rho_{0,A}e^{-TR/T_{1,A}} - \rho_{0,B}e^{-TR/T_{1,B}}) \quad (3.46)$$

obtaining a T1-weighted contrast. Differentiating C_{AB} with respect to TR can optimize the T1-weighted image.

If TR is chosen such that

$$TR >> T_{1A,B} \Rightarrow e^{-TR/T_1} \rightarrow 0$$

Then the gradient echo contrast is

$$C_{AB} = \rho_{0,A} e^{-TE/T_{2,A}^*} - \rho_{0,B} e^{-TE/T_{2,B}^*} \quad (3.47)$$

which indicates a T2* weighted contrast. Differentiating C_{AB} with respect to TE can optimize the $T2^*$-weighted image.

Besides the three major contrast mechanisms, certain external agents can act to reduce the T_1 of the tissue after being introduced into the targeted tissues. If the targeted tissue and its neighboring tissue are difficult to differentiate, but have different response to a contrast agent, then the agent helps to differentiate the two, hence enhancing the contrast.

In general, both T_1 and T_2 are shortened, and the shorting effect is directly proportional to the concentration C of the contrast agent delivered to the tissue, given as

$$\frac{1}{T_1(C)} = \frac{1}{T_{1,0}} + \alpha_1 C$$

$$\frac{1}{T_2(C)} = \frac{1}{T_{2,0}} + \alpha_2 C \quad (3.48)$$

where $T_{1,0}$ and $T_{2,0}$ are the intrinsic T_1 and T_2 of the tissue, $T_1(c)$ and $T_2(c)$ are the shortened values, α_1 is the longitudinal relaxivity, and α_2 is the transverse relaxivity of the contrast agent. α_1 and α_2 are specific to the composition of the contrast agent.

3.7 Fast Imaging Methods

3.7.1 EPI Sequence

As mentioned earlier, the total acquisition time for a 3D image is $N_y N_z$ TR, therefore, there are two ways to reduce the total acquisition time: one is to reduce TR and the other is to

collect all the data within one TR. FLASH (fast low angle shot) and EPI (echo planar imaging) are two sequences utilizing each method, respectively.

Fig. 3.5 shows the phase encoding and read gradient waveforms for an EPI sequence and Fig. 3.6 shows a spin echo EPI imaging sequence.

In a single shot EPI sequence, one 'train' of echoes is collected after a single rf excitation with a short phase encoding gradient pulse (a blip) between each echo. Given the parameters defined in Fig. 3.5, the total acquisition time, excluding preparatory pulses, is

$$T_D = N_y(T_S + \Delta T) = N_x N_y \Delta t + N_y \Delta T \tag{3.49}$$

The minimum total time to complete an experiment is

$$T_T = \tau_{rf}/2 + t_0 + T_D \tag{3.50}$$

Based on the definition of TE where k=0, TE in EPI sequence is given by

$$TE = \frac{N_y + 1}{2} N_x \Delta t + (N_y + 1)\tau_{rf} + t_0 \tag{3.51}$$

Accordingly, the EPI image intensity is approximated by

$$\rho(\vec{r}) = \rho_0(\vec{r}) e^{-TE/T_2^*} \tag{3.52}$$

No T_1 dependence is seen since TR is infinitely long for this case. T_1-weighted contrast can be obtained by repeating the EPI experiment at intervals of TR, yielding

$$\rho(\vec{r}) = \rho_0(\vec{r}) e^{-TE/T_2^*} (1 - e^{-TR/T_1}) \tag{3.53}$$

Since all the data is collected after one rf excitation, T2* is the only factor that limits the number of phase encoding steps, that is, how many lines can be covered in k-space. A reasonable rule to follow is that sufficient signal can be collected until the total data sampling time becomes comparable to T2*, leading to the relation

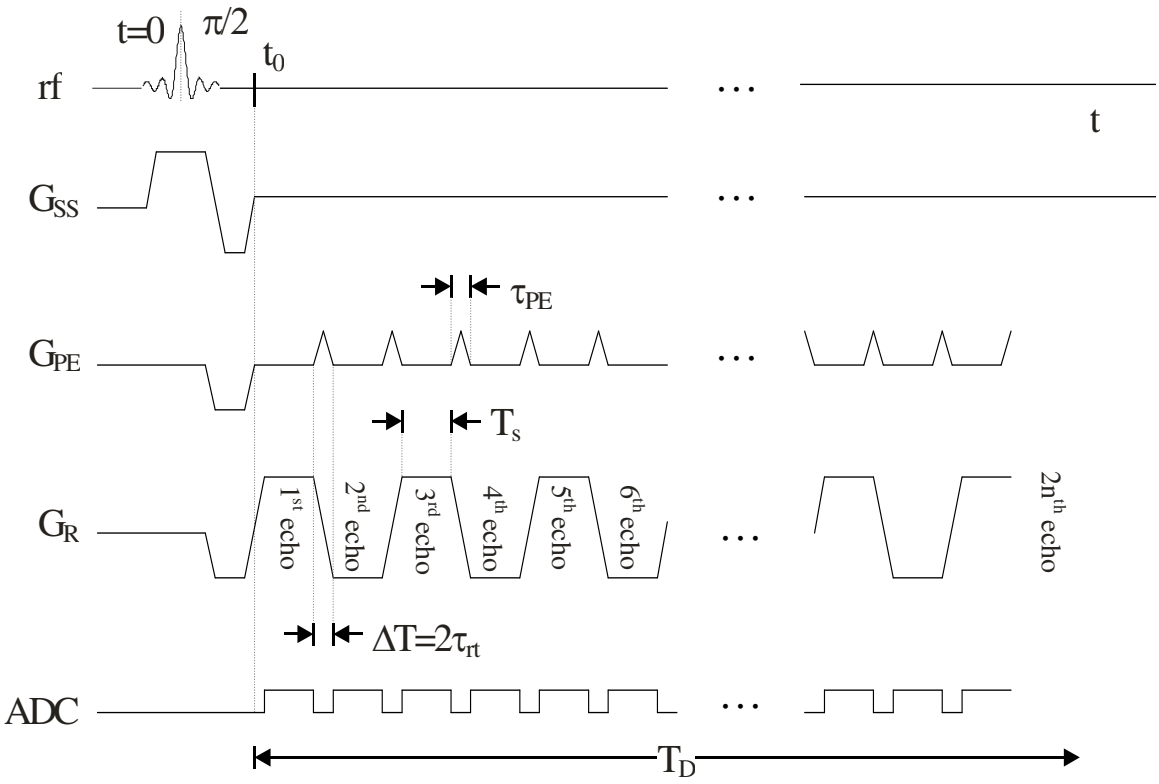

Figure 3.5: An EPI sequence showing the phase encoding and read gradient waveforms.

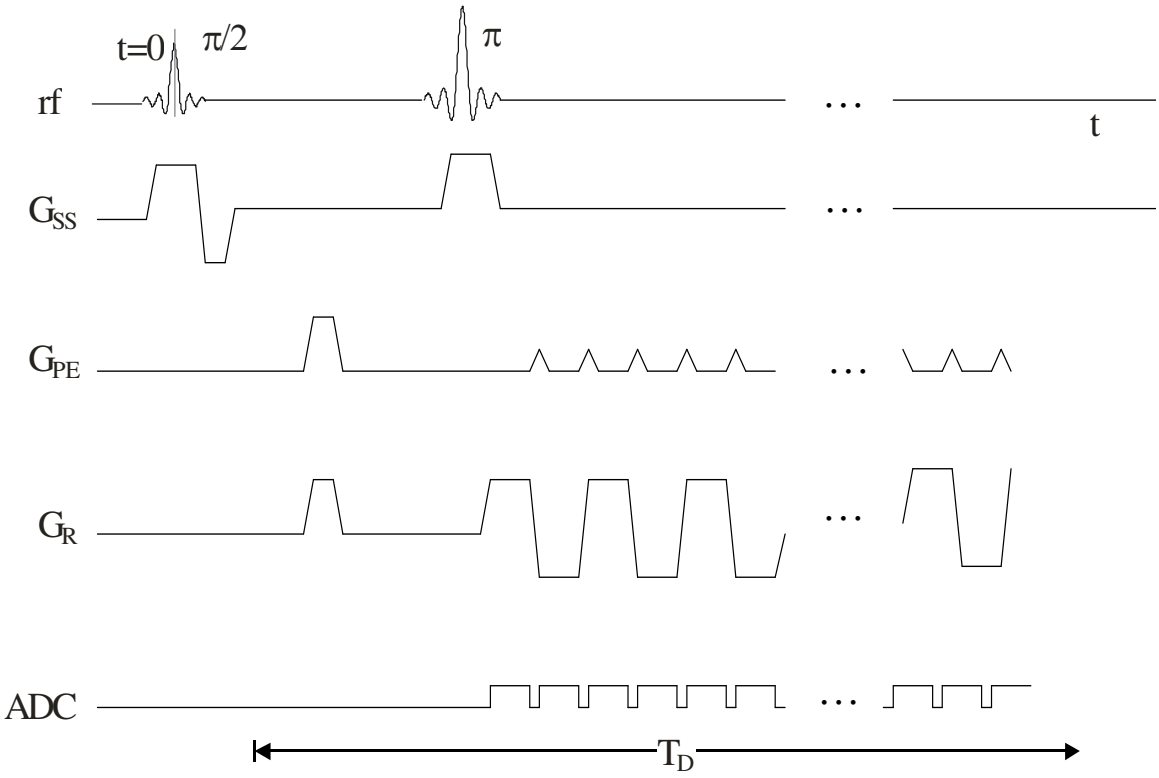

Figure 3.6: A spin echo EPI imaging sequence.

$$N_{y,\max} \approx \frac{T_2^*}{N_x \Delta t + 2\tau_{rf}} \tag{3.54}$$

In summary, the following relations must be considered when developing an EPI sequence.

(a) $\Delta t = 1/(\gamma G_{x,\max} L_x)$

(b) $\Delta x = L_x / N_x$

(c) $\Delta G_{y0} = 1/(\gamma L_y \tau_{rf})$

(d) $N_{y,\max} \approx \frac{T_2^*}{N_x \Delta t + 2\tau_{rf}}$

(e) $\Delta y_{\min} \approx L_y / N_{y,\max}$ (3.55)

where the sampling rate in (a), and the phase encoding step amplitude in (c) are determined by the Nyquist Criterion.

3.7.2 FLASH Sequence

Another method to reduce the acquisition time is by using a Flash sequence with a short TR. In this subsection the build-up of the magnetization to steady state is discussed.

The steady state means the value of M_z just prior to each subsequent rf pulse is unchanged from cycle to cycle. In the steady-state incoherence (SSI) sequence, the transverse magnetization prior to each rf pulse is destroyed on purpose by the spoiling mechanism.

The longitudinal and transverse magnetization evolves during the first period according to

$$M_\perp(t) = M_\perp(0^+) e^{-t/TR}$$

$$M_z(t) = M_0(1 - e^{-t/T_1}) + M_z(0^+) e^{-t/T_1} \tag{3.56}$$

where

$$M_{\perp}(0^{+}) = M_0 \sin\theta$$

$$M_z(0^{+}) = M_0 \cos\theta$$

During the period from nTR to (n+1) TR, the relative time within this cycle to the total time from the first pulse t is

$$t_n \equiv t - nTR \tag{3.57}$$

Then

$$M_z(t_n) = M_0(1 - e^{-t/T_1}) + M_z(nTR^{+})e^{-t/T_1} \tag{3.58}$$

where

$$M_z(nTR^{+}) = M_z(nTR^{-})\cos\theta$$

Define the steady-state equilibrium value of M_z to be M_{ze}, which must satisfy

$$M_{eq} = M_0(1 - e^{-t/T_1}) + M_{eq}\cos\theta e^{-t/T_1} \tag{3.59}$$

This yields the equilibrium value

$$M_{eq} = \frac{M_0(1 - E_1)}{1 - E_1\cos\theta} \tag{3.60}$$

where $E_1 = e^{-TR/T_1}$

The transverse magnetization can be given by

$$M_{\perp}(t_n) = M_{eq}\sin\theta E_2 \tag{3.61}$$

under steady state equilibrium, where $E_2 = e^{-TE/T_2^{*}}$.

Finally, the steady-state signal from a voxel is

$$\rho(\theta, TE) = \rho_0 \sin\theta \frac{(1 - E_1)}{(1 - E_1\cos\theta)} e^{-TE/T_2^{*}} \tag{3.62}$$

The general behavior of ρ is a function of θ, and the Ernest angle is defined as where the maximal signal occurs,

$$\theta = \cos^{-1} E_1 \equiv \theta_E \tag{3.63}$$

CHAPTER 4

Dissertation Related Methods

This chapter introduces the methods used in this dissertation to measure water content, CBV, CBF, and permeability.

4.1 Absolute Water Content Measurement

Absolute water content of the rat brain, in the presence of RF inhomogeneity and flip angle miscalibration, can be measured using an MRI approach[43-46]. The principle of such an approach is introduced below.

The ideal FLASH signal is given as

$$s(\theta) = \frac{(1 - E_1)}{1 - E_1 \cos\theta} \sin\theta \qquad (4.1)$$

where $E_1 = e^{-TR/T_1}$. It can be transformed into

$$\frac{s(\theta)}{\sin\theta} = \frac{s(\theta)}{\tan\theta} E_1 + M_0(1 - E_1) \qquad (4.2)$$

after the T^*_2 effect is ignored.

This expression implies that the data in [$x = \frac{s(\theta)}{\tan\theta}$, $y = \frac{s(\theta)}{\sin\theta}$] space can be least squares fitted to a line whose slope and intercept made with the y axis are E_1 and $M_0(1\text{-}E_1)$, respectively. Subsequently, M_0, the longitudinal equilibrium magnetization, can be estimated with a known T_1.

M_0 is given by

$$M_0 = \frac{\rho_0 \gamma^2 \hbar^2}{4KT} B_0 \tag{4.3}$$

where ρ_0 is the spin density, defined as the number of protons per unit volume, γ is the gyromagnetic ratio, $\hbar \equiv h/2\pi$ in terms of Planck's quantum constant h, K is the Bolzmann's constant, T is the absolute temperature, and B_0 is the external static magnetic field. Therefore, M_0 can be used as a measurement of water content since it is proportional to the spin density.

But in practice, there are spatial variations in the RF field. If the same coil is used both for RF-transmission and reception, the RF sensitivity patterns for transmission and reception are the same. If α is used to model the spatial sensitivity variation, the signal measured at a given voxel ρ is scaled to to $\alpha\rho$, and the flip angle is also scaled from the desired value θ to $\alpha\theta$. In addition, there is a flip angle miscalibration scaling factor α_0, which will be estimated later.

Therefore, for the nonideal case, the signal can be rewritten in the form[43]

$$\frac{\rho_{nonideal}(\theta_0)}{\sin(\alpha_0 \alpha \theta_0)} = \frac{\rho_{nonideal}(\theta_0)}{\tan(\alpha_0 \alpha \theta_0)} E_1 + \alpha \rho_0 (1 - E_1) \tag{4.4}$$

In order to obtain an estimate of spin density or brain water content, both α_0 and α are needed. We will discuss how α_0 can be experimentally derived, followed by the procedures for α below. The signal should be zero for all the tissues when the actual flip angle experienced is 180^0, and the signal behaves linearly as a function of flip-angle in the neighborhood of 180^0, as is shown in Fig. 4.1. The signal zero crossing can be obtained by fitting a set of high filp angle (around 180^0) signal measurements to a straight line. If the signal zero crossing occurs at θ_z, then α_0 is estimated as

$$\alpha_0 = \frac{180}{\theta_z} \tag{4.5}$$

Next, a low flip-angle (<< the Ernest angle) image of a homogeneous phantom that fills the volume-of-interest in the nonideal case is described by

$$\rho(r,\theta_0)\Big|_{\theta_0<<\theta_E} \approx (\alpha(r)\rho_0)(\alpha(r)\alpha_0\theta_0) \propto \alpha^2(r) \qquad (4.6)$$

yielding the estimates of the spatial variations in the RF-field. That is, a relative RF-field map is the square root of the low flip-angle image of a homogeneous object.

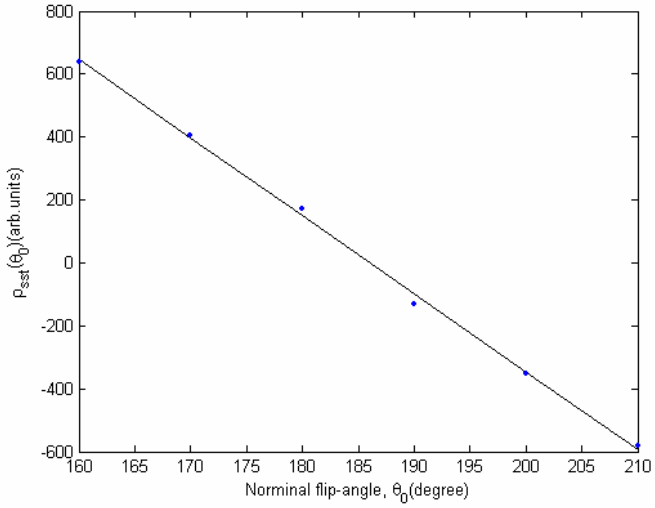

Figure 4.1: Plot of voxel signal measured on a phantom with large flip angles around 180^0. The signal measurements are least squares fitted to the solid line.

If T_2*-induced signal loss is not neglected, a double echo sequence can be used to determine T_2* first by fitting the two signal measurements to an exponential decay, thus minimizing the effects of T_2* signal decay.

Finally, an absolute estimate of brain water content is obtained by normalizing the effective spin-density of the brain to that of a water phantom.

Another method to measure water content is the wet-dry method. The percent of water content can be calculated by the following equation: percent water=((wet weight-dry weight)/wet weight)*100. The MRI method can be compared with the wet-dry method on gel phantoms or normal rat brain. Normal rat brain has water content of about 78%.

4.2 The Steady-State Method to Measure CBV

4.2.1 The Steady-State Method

Due to its simplicity compared with the DSC (dynamic susceptibility contrast) [107, 108] method, the 3D steady state method[113] offers a great potential to determine absolute cerebral blood volume with an intravascular T_1 contrast agent when the BBB remains intact. The basic principle is given as follows.

Supposing the injected contrast agent only affects the vascular space (intravascular compartment) and the blood volume of one voxel is α, the voxel signal before and after the injection of the contrast agent can be given by

$$S_{tissuepre}=(1-\alpha)\, S_{pt}+\alpha\, S_{bloodpre} \quad (4.7)$$

$$S_{tissuepost}=(1-\alpha)\, S_{pt}+\alpha\, S_{bloodpost} \quad (4.8)$$

where S_{pt} is the tissue signal if the whole voxel is only occupied by the tissue.

If one voxel is totally occupied by blood and can be found in the sagittal sinus or the jagular vein, then $S_{bloodpre}$ and $S_{bloodpost}$ can be obtained. Subsequently, α can be given by

$$\alpha = (S_{tissuepost} - S_{tissuepre})/(S_{bloodpost} - S_{bloodpre}) \quad (4.9)$$

and hence yielding the CBV map.

4.2.2 Error propagation from the signal measurement into CBV estimation

From Eq. (4.9), the error in CBV can be estimated by

$$\delta\hat{CBV} \approx (\frac{\partial CBV}{\partial \hat{S}_{tissuepre}})\partial\hat{S}_{tissuepre} + (\frac{\partial CBV}{\partial \hat{S}_{tissuepost}})\partial\hat{S}_{tissuepost} + (\frac{\partial CBV}{\partial \hat{S}_{bloodpre}})\partial\hat{S}_{bloodpre} + (\frac{\partial CBV}{\partial \hat{S}_{bloodpost}})\partial\hat{S}_{bloodpost} \tag{4.10}$$

The variance of the CBV estimation error is

$$\sigma^2_{\hat{CBV}} = \frac{2\sigma_0^2}{(S_{bloodpost} - S_{bloodpre})^2} + \frac{2\sigma_0^2 CBV^2}{(S_{bloodpost} - S_{bloodpre})^2} = \frac{2\sigma_0^2}{(S_{bloodpost} - S_{bloodpre})^2}(1 + CBV^2) \tag{4.11}$$

$S_{tissuepost}$, $S_{tissuepre}$, $S_{bloodpost}$, and $S_{bloodpre}$ have the same variance σ_0^2.

4.2.3 Imaging parameters selection

Below I will discuss further how imaging parameters are selected to reduce the variance of CBV estimation.

The signal for this sequence (also a FLASH sequence) can be given as

$$S = \rho \frac{1 - E_1}{1 - E_1 \cos\theta} \sin\theta \times e^{-TE/T_2^*} \tag{4.12}$$

where $E_1 = e^{-TR/T_1}$. TE is chosen as short as possible to improve S.

Next, I did some simulations to discuss how the flip angle is chosen based on the error propagation analysis.

Let TR=30ms, and assume T_{1blood}=1500ms, $T_{1gray\ matter}$=1250ms, $T_{1\ white\ matter}$=1110ms at 3T, and T_{1blood}=150ms after the injection of contrast agent.

The signal as a function of flip angle pre and post administration of contrast agent for blood ('o'), gray matter ('*'), and white matter ('+') is shown in Fig. 4.2 and Fig. 4.3. SNR is better pre contrast agent with flip angle=15^0, however, as shown in Fig. 4.3, ($S_{bloodpost}$-$S_{bloodpre}$) is bigger when flip angle=35^0 than when flip angle=15^0. From Eq. (4.11), flip angle=35^0 is chosen to reduce $\sigma^2_{\bar{CBV}}$.

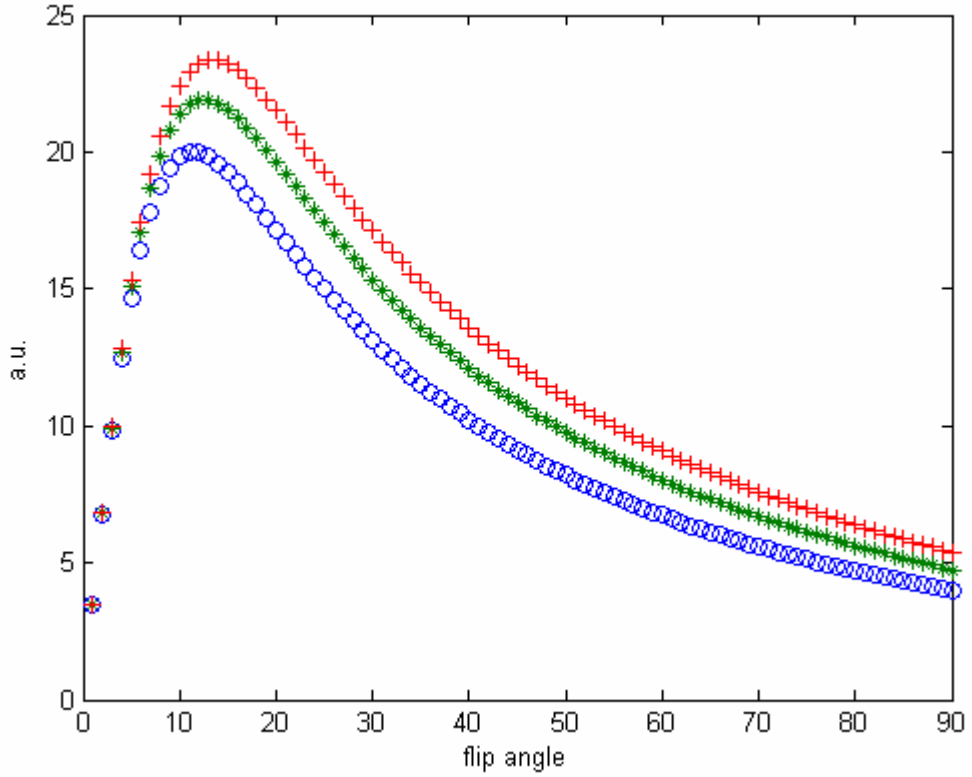

Figure 4.2: The signal as a function of flip angle pre contrast agent for blood ('o'), gray matter ('*'), and white matter ('+').

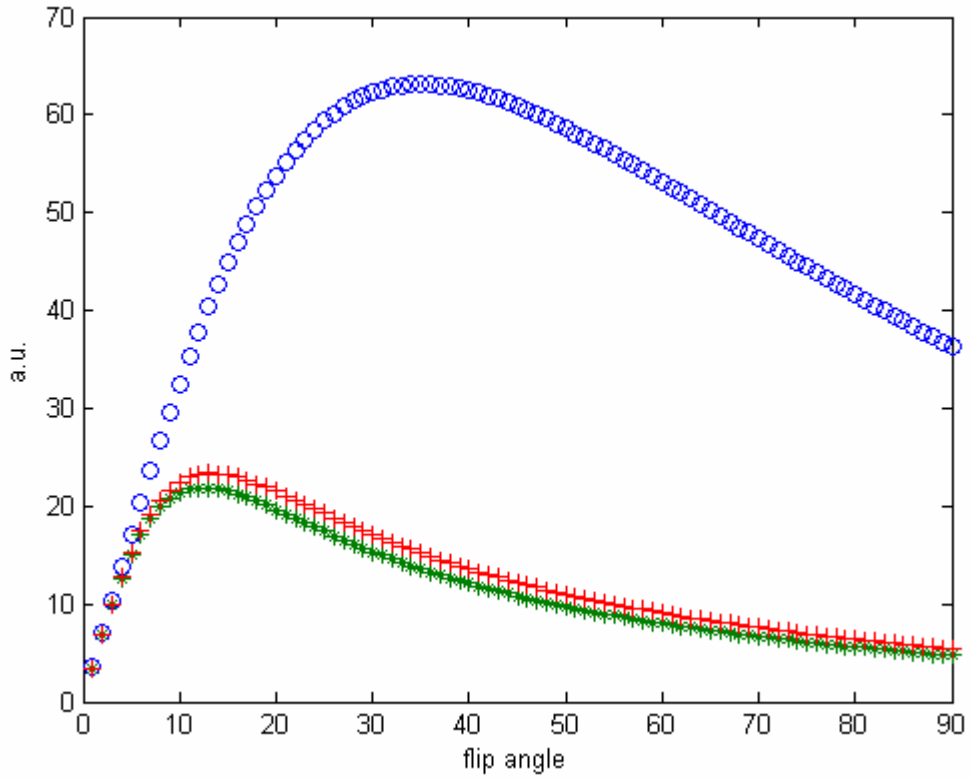

Figure 4.3: The signal as a function of flip angle post contrast agent for blood ('o'), gray matter ('*'), and white matter ('+').

4.2.4 Water Exchange Mechanisms

However, in reality, the effects of the contrast agent can be extended to the vascular compartment via water exchange process, which will be discussed below, thus complicating the CBV measurement.

Water exchange between two compartments (e.g. intravascular and extravascular compartments) with the exchange rate defined as

$$\frac{1}{\tau} = \frac{1}{\tau_{iv}} + \frac{1}{\tau_{ev}} \tag{4.13}$$

where τ_{iv} and τ_{ev} are the average residence time of a proton spent in the intravascular and extravascular compartments, respectively[144]. The criteria for determining whether the exchange is fast or slow is given as follows. Fast exchange is given by

$$\frac{1}{\tau} >> \left| \frac{1}{T1_{iv}} - \frac{1}{T1_{ev}} \right| \tag{4.14}$$

Similarly, the slow exchange is

$$\frac{1}{\tau} << \left| \frac{1}{T1_{iv}} - \frac{1}{T1_{ev}} \right| \tag{4.15}$$

Under the fast exchange condition, a tissue with two compartments behaves like a single compartment with a single relaxation rate, given by

$$\frac{1}{T1} = \frac{f_{iv}}{T1_{iv}} + \frac{f_{ev}}{T1_{ev}} \tag{4.16}$$

where f_{iv} and f_{ev} are the volume fractions of the intravascular and extravascular compartments, respectively, and $f_{iv}+f_{ev}=1$. On the other hand, under slow exchange conditions, the two compartments behave differently with new relaxation rates as

$$\frac{1}{T1_{iv}^{'}} = \frac{1}{T1_{iv}} + \frac{1}{\tau_{iv}} \tag{4.17}$$

$$\frac{1}{T1_{ev}^{'}} = \frac{1}{T1_{ev}} + \frac{1}{\tau_{ev}} \tag{4.18}$$

where prime indicates the relaxation times influenced by the water exchange and $f_{iv} / \tau_{iv} = f_{ev} / \tau_{ev}$ holds. If the exchange is neither fast nor slow, it is called intermediate exchange, mathematically described by the following condition

$$\frac{1}{\tau} \approx \left| \frac{1}{T1_{iv}} - \frac{1}{T1_{ev}} \right| \tag{4.19}$$

In this case, multiple relaxation rates could be observed.

In a two-compartment system, its behavior largely depends on the water exchange between the two compartments, but all conditions of exchange can be taken into account with the mathematical model proposed by Hazelwood et al.[145].

The modified Bloch equation below reflects that a magnetization transfer between the intravascular and extravascular compartments exists by the water exchange:

$$\frac{\partial M_{iv}}{\partial t} = \frac{M_{oiv}}{T1_{iv}} - \frac{M_{iv}}{T1_{iv}} - \frac{M_{iv}}{\tau_{iv}} + \frac{M_{ev}}{\tau_{ev}} \tag{4.20}$$

$$\frac{\partial M_{ev}}{\partial t} = \frac{M_{oev}}{T1_{ev}} - \frac{M_{ev}}{T1_{ev}} - \frac{M_{ev}}{\tau_{ev}} + \frac{M_{iv}}{\tau_{iv}} \tag{4.21}$$

where M_{0ev} and M_{0iv} represent the thermal equilibrium magnetization values of M_{iv} and M_{ev} respectively.

Solution of the eqs(4.20), (4.21) using a flash sequence is given by

$$S_{tissue}(TR) = f_{iv}^{'} \times M_0 \left(\frac{(1-\exp(-TR/T1_{iv}^{'})\sin\theta}{1-\exp(-TR/T1_{iv}^{'})\cos\theta}\right)$$

$$+ f_{ev}^{'} \times M_0 \left(\frac{(1-\exp(-TR/T1_{ev}^{'})\sin\theta}{1-\exp(-TR/T1_{ev}^{'})\cos\theta}\right) \tag{4.22}$$

Where

$$\frac{1}{T1_{iv}^{'}} = A_1 + A_2$$

$$\frac{1}{T1_{ev}^{'}} = A_1 - A_2$$

$$f_{iv}^{'} = \frac{1}{2} - \frac{1}{4}\left[(f_{ev} - f_{iv})\left(\frac{1}{T1_{iv}} - \frac{1}{T1_{ev}}\right) + \frac{1}{\tau_{iv}} - \frac{1}{\tau_{ev}}\right] / A_2$$

$$f_{ev}^{'} = -\frac{1}{2} + \frac{1}{4}\left[(f_{ev} - f_{iv})(\frac{1}{T1_{iv}} - \frac{1}{T1_{ev}}) + \frac{1}{\tau_{iv}} - \frac{1}{\tau_{ev}} \right] / A_2 \qquad (4.23)$$

In which

$$A_1 = \frac{1}{2}\left[\frac{1}{T1_{iv}} + \frac{1}{T1_{ev}} + \frac{1}{\tau_{iv}} + \frac{1}{\tau_{ev}} \right]$$

$$A_2 = \frac{1}{2}\left[(\frac{1}{T1_{iv}} + \frac{1}{T1_{ev}} + \frac{1}{\tau_{iv}} - \frac{1}{\tau_{ev}})^2 + \frac{4}{\tau_{iv}\tau_{ev}} \right]^{1/2} \qquad (4.24)$$

The parameters in eq. (4.23) obey the general relationship

$$\frac{f_{iv}^{'}}{T1_{iv}^{'}} + \frac{f_{ev}^{'}}{T1_{ev}^{'}} = \frac{f_{iv}}{T1_{iv}} + \frac{f_{ev}}{T1_{ev}} \qquad (4.25)$$

which means the initial slope of the signal decay is independent of the exchange rate.

When the following conditions are satisfied:

$TR << \min(T1_{iv}^{'}, T1_{ev}^{'})$

and

$\frac{\cos\theta}{1-\cos\theta}\frac{TR}{T1} << 1,$

CBV can be measured independently of the exchange model due to the fact that the blood or tissue signal can be expressed as a linear function of the longitudinal relaxation time. Therefore the no-exchange model and fast-exchange model give the same estimates of CBV. This justifies the assumption that no exchange occurs between the blood and the tissue for the steady-state method to measure CBV.

4.3 Dynamic Susceptibility Contrast (DSC)

Another method to measure CBV in MRI is the dynamic imaging method, which will be briefly described here.

The indicator dilution method has been used for many years to extract tissue hemodynamic information, and currently this approach is the most commonly used in MR to obtain in vivo cerebral physiological parameters including blood volume, cerebral blood flow, and mean transit time in both normal and diseased states. This model also assumes intact blood-brain barrier[107, 108]. Measurements of the signal intensity before, during and after the injection of a non-diffusible contrast agent are required; therefore, a rapid dynamic imaging sequence such as an echo-planar imaging sequence is employed in this approach.

In a T2* weighted dynamic MR imaging sequence, the signal intensity before and after the contrast agent injection are:

$$S_{precontrast}(TE)=M_0 \exp(-TE\times R^*_{2precontrast}) \quad (4.26)$$

$$S_{postcontrast}(TE)=M_0 \exp(-TE\times R^*_{2postcontrast}) \quad (4.27)$$

where $R^*_{2precontrast}$ is the effective relaxation rate of the tissue, and R^*_{2post} is the effective relaxation rate after the injection of the contrast agent.

The concentration of contrast agent in a volume of interest obeys the relationship:

$$C_{VOI}(t) \propto \Delta R_2^* = R^*_{2\,postcontrast} - R^*_{2\,precontrast} = -\frac{\ln(\frac{s(t)}{s_0})}{TE} \quad (4.28)$$

where S_0 is the mean signal intensity before the contrast agent injection and S(t) is the signal intensity during and after the injection of contrast agent. Fig 4.4 shows the signal intensity curve of the voxels chosen to obtain global arterial input function from five blood voxels, and Fig 4.4 shows the concentration time curve as the arterial input function, from which we can see the concentration reaches its maximum and then decays to zero eventually.

According to indicator dilution theory, a single function h(t) can be used to describe a system with a single input and single output. The amount of contrast agent that leaves the

system between the time t and t+dt is given by h(t)dt, and the fraction of contrast agent remaining in the system[107, 108] (residue function) R(t) is given by

$$R(t) = (1 - \int_0^t h(\tau) d\tau) \tag{4.29}$$

The concentration of tracer in a given volume of interest $C_{VOI}(t)$ and that in an artery $C_a(t)$ obey the relationship[107, 108]:

$$C_{VOI}(t) = F_t \cdot C_a(t) \otimes R(t) \tag{4.30}$$

where F_t is tissue flow. R(t) and F_t can be obtained simultaneously with a singular value decomposition (SVD) method.

At the same time, CBV and mean transit time (MTT) can be given by

$$CBV = \frac{\int_0^\infty C_{VOI}(\tau) d\tau}{\int_0^\infty C_a(\tau) d\tau} \tag{4.31}$$

$$MTT = \frac{CBV}{Ft} \tag{4.32}$$

Fig 4.6 shows the rCBF, rMTT and rCBV maps on an ischemia rat during occlusion period. The arrows point to the ischemia area.

4.4 The Continuous Arterial Spin Labeling (CASL) Method to Measure CBF

Arterial spin labeling (ASL) is a method to calculate CBF without the need for an exogenous contrast agent. ASL can be classified into two categories: the pulsed technique of flow-alternating inversion recovery, or FAIR, and continuous ASL (CASL). Despite its relatively low sensitivity, ASL makes use of arterial water as an endogenous perfusion tracer, and therefore is fully noninvasive[100].

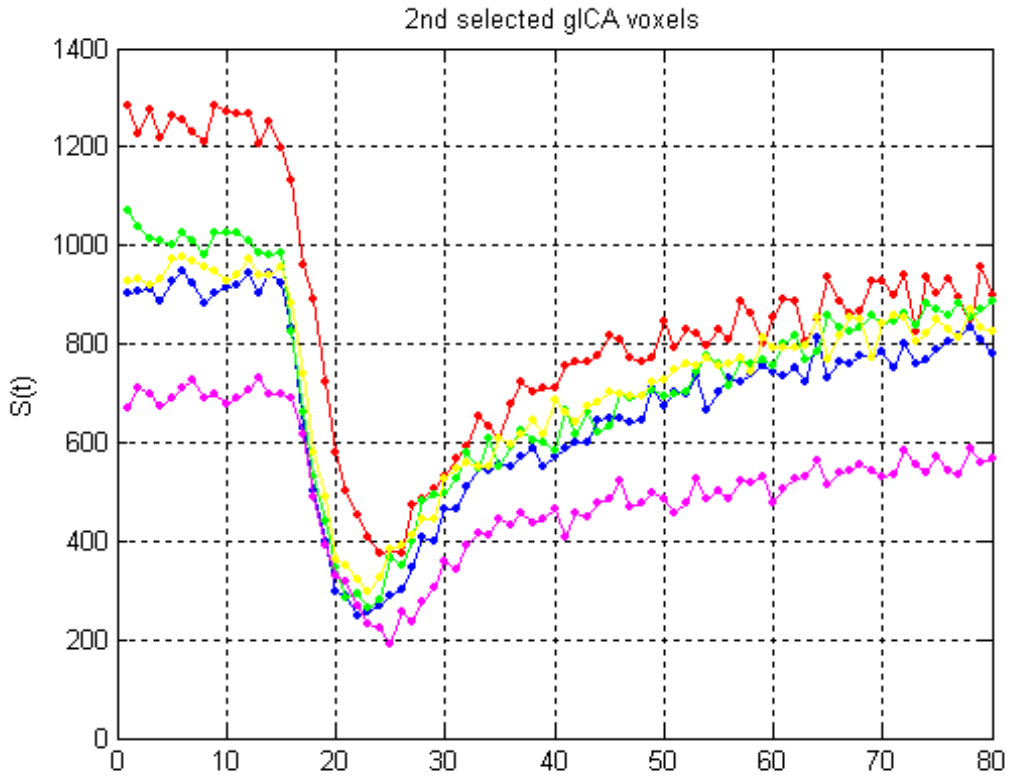

Figure 4.4: signal curves of the voxels chosen to obtain global arterial input function.

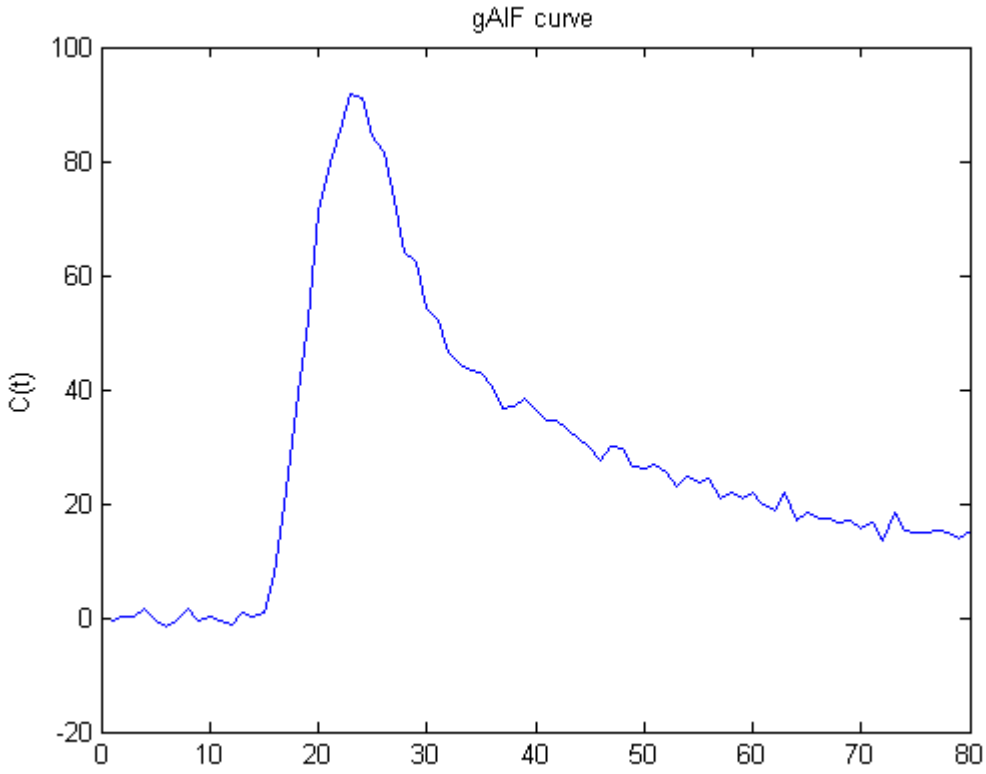

Figure 4.5: Concentration curve as the global arterial input function.

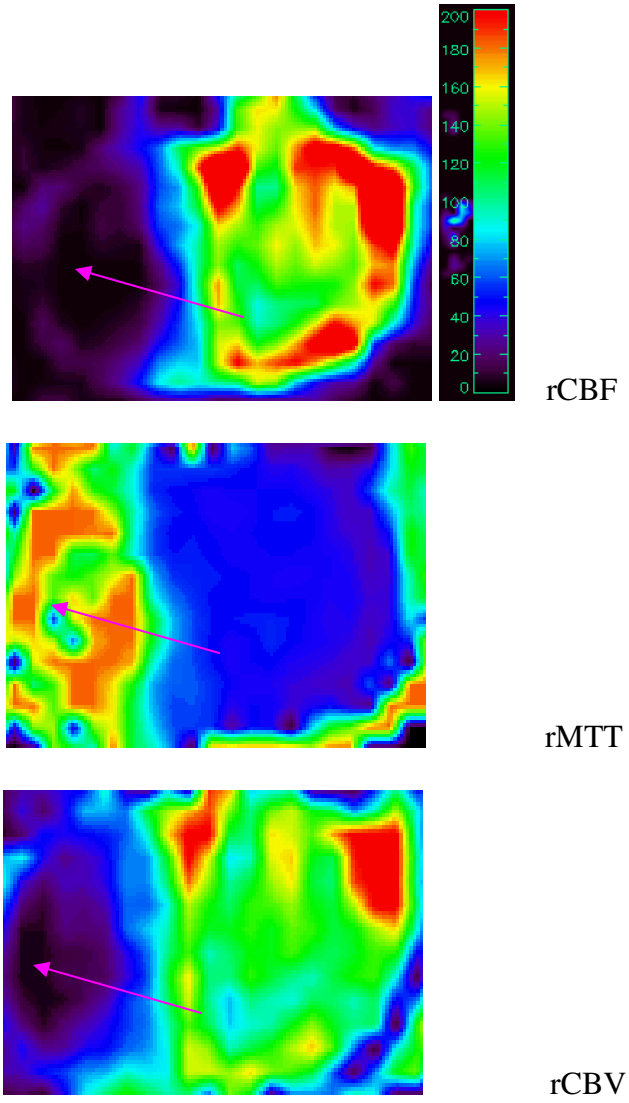

Figure 4.6: rCBF, rMTT and rCBV maps on an ischemia rat during occlusion period.

The FAIR technique uses a 180^0 nonselective RF pulse to invert or "label" the longitudinal magnetization of the protons, which is measured using EPI after an inversion time (TI), whereas for the control image, a selective RF pulse is applied, inverting only the protons in the image slice. The difference in signal between the control and labeled images is proportional to the blood flow rate[100].

CASL uses a spatially localized RF field with a labeling period τ to continuously invert the longitudinal magnetization of the protons in arterial blood. Fig.4.7 shows the pulse sequence timing diagram. At the end of the labeling, a short delay, w, is introduced. Upon arrival at the image slice of the labeled spins, the magnitude of the longitudinal magnetization of the arterial blood has decreased due to T1 relaxation and is then measured using EPI [100, 101]. Subsequently, a control image is taken without arterial spin labeling. The signal difference between the "labeled" image and the control image is given by

$$\Delta M = \frac{2M_0 f\alpha}{\lambda R_{1a}}[\exp(-wR_{1a}) - \exp(-(\tau + w)R_{1a})] \qquad (4.33)$$

where M_0 is the equilibrium magnetization of the brain, f is CBF, α is tagging efficiency, λ is blood/tissue water partition coefficient, and R_{1a} is the longitudinal relaxation rate of blood.

Fig. 4.8 shows a typical color-coded CBF map under ischemic condition, and CBF can be reduced to about 40ml/100g/min. The arrow points to the ischemia area.

4.5 Patlak Plot Method to Measure Permeability

Fig. 4.9 shows the theoretical model of water exchange between blood and brain proposed by Patlak et al.[49]. This model consists of a blood-plasma compartment, a reversible tissue region, and one or more irreversible tissue regions. The n compartments in the

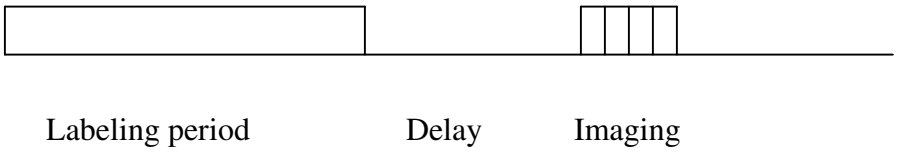

Figure 4.7: Pulse sequence timing diagram. Labeling RF and gradients are applied during the labeling period. Then, a postlabeling delay is inserted. Finally, rapid gradient-echo echo-planar imaging is performed to acquire images.

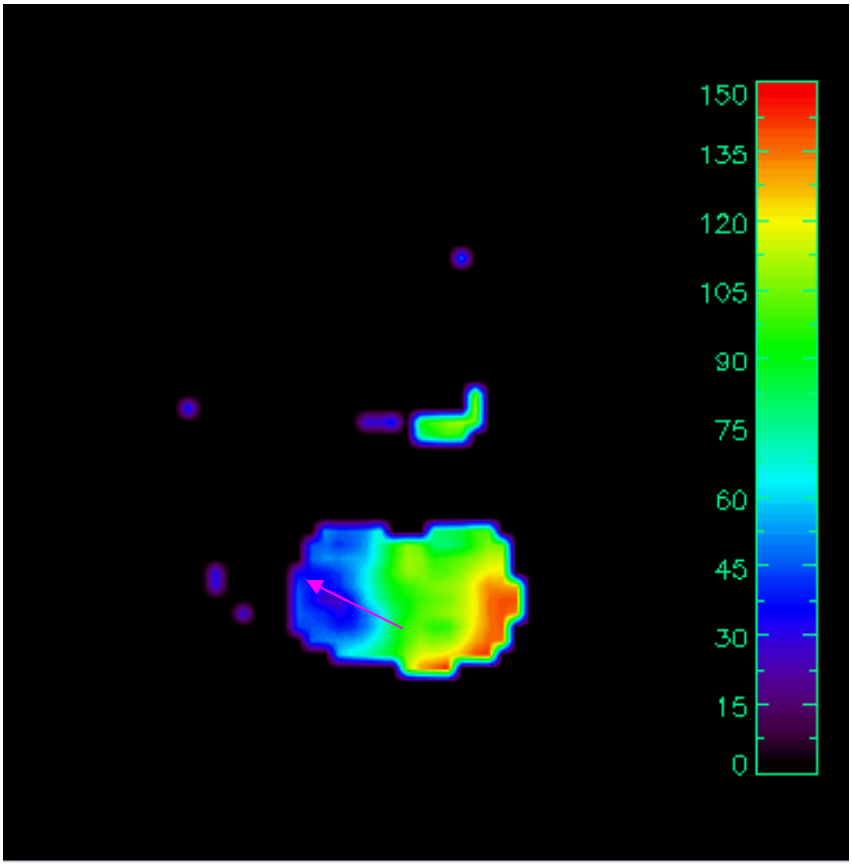

Figure 4.8: A typical CBF map under ischemic condition.

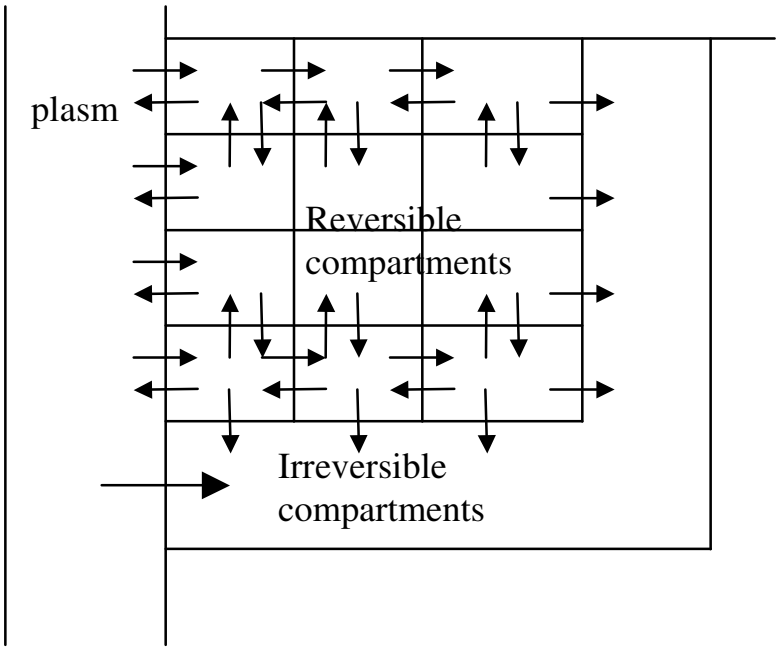

Figure 4.9: A Model of blood-brain exchange. The test solute may move from the plasma to any of the reversible compartments or vice versa; the solute can enter, but can not leave the irreversible regions.

reversible region freely communicate with each other and the plasma; the test solute can move in or between the plasma and any of the compartments. The solute can enter the irreversible regions from the plasma and/or the reversible region but cannot leave the irreversible region[47-55].

Assuming linear transfer kinetics, Patlak et al. derived a procedure to obtain the blood-to-tissue transfer or influx constant, Ki, by graphical analysis of a time series of tissue and arterial concentrations with the following equation:

$$\frac{C_{tis}(t)}{C_{pa}(t)} = K_i \frac{\int_0^t C_{pa}(\tau)d\tau}{C_{pa}(t)} + V_p \qquad (4.34)$$

where $C_{tis}(t)$ is the tissue concentration (per unit weight) at the end of the experimental period (t); $C_{pa}(\tau)$ is the arterial plasma concentration (per unit volume) at a series of times over the duration of the experiment, and is used to calculate the arterial concentration-time integral; K_i is the blood-to-brain transfer constant of the indicator; and V_p is the tissue volume in which the blood-borne indicator mixes prior to crossing the rate-limiting barrier. The Patlak plot is a graph of the ratio of the total tissue solute concentration at the sampling time $C_{tis}(t)$ to the plasma concentration at the respective times $C_{pa}(t)$ versus the ratio of the arterial plasma concentration-time integral $\int_0^t C_{pa}(\tau)d\tau$ to $C_{pa}(t)$. This graph will yield a curve that eventually becomes linear when a unidirectional transfer process is dominant during part or all of the experimental period. In this case, the slope of the line is K_i, and the intercept of the line is V_p. In normal tissue, V_p is the volume of the plasma plus the volume of red blood cells, which are adjacent to the plasma and have high membrane water permeability. When the BBB is open, V_p could also include the volume of various elements of the brain parenchyma.

In an MRI study, a contrast agent is injected as a test solute, and the concentration of the contrast agent is estimated by $\Delta R_1(t)$, the difference between R1 measured at time t after the contrast injection minus the preinjection R1 as discussed in:

$$C_{pa}(t_n) \propto \frac{\Delta R_{1a}(t_n)}{(1-Hct)} \text{ , and } C_{tis}(t_n) \propto \Delta R_{1tis}(t_n) \qquad (4.35)$$

where $\Delta R_{1tis}(t_n)$ and $\Delta R_{1a}(t_n)$ are differences in R1 measured in tissue and sagittal sinus, respectively, at time t_n. n stands for different time points and the hematocrit (Hct) is the

fraction of the volume of red blood cells to the volume of whole blood, with a typical value 0.4.

In fact, $\Delta R_{1tis}(t)$ and $\Delta R_{1a}(t)$ are often used as estimates of tissue and arterial concentrations, since we generally assume that the constant of proportionality between concentration and ΔR_1 (i.e., the relaxivity) does not change across tissues, that is, the scaling constant to tissue concentration in (4.35) is the same for blood and tissue.

4.6 Look-locker Method to Measure T1

The Look-Locker method[57] is extremely popular for in vivo T1 measurements due to its fast sampling capacity of a large set of points on the recovery curve. The T-one by multiple readout pulses (TOMROP) sequence, an imaging variant of the look-locker (L-L) technique, can be used for a pixel-by-pixel estimate of T1.

Fig. 4.10. shows the TOMROP sequence diagram. First, inversion of spins is accomplished by using a nonselective hyperbolic secant adiabatic pulse. A train of pulses with a small flip angle β can create a set of gradient echoes. After acquisition of each gradient echo, a spoiler gradient (S) is employed to destroy the remaining transversal magnetization.

The longitudinal magnetization Mn just before the n-th (1<<n<<N) read out pulse is given by the equation[57]

$$M_n = M_{eq}[F + (C_\beta E_2)^{n-1}(Q - F)], \qquad (4.36)$$

where $C_\beta = \cos\beta$, $E_2 = \exp(-TI_2 / T_1)$, $F = (1 - E_2)/(1 - C_\beta E_2)$, and Q is the quotient of the longitudinal magnetization M_1, just before the first small flip angle RF pulse and the equilibrium magnetization M_{eq}. After some sequence cycles, the spin system reaches a steady

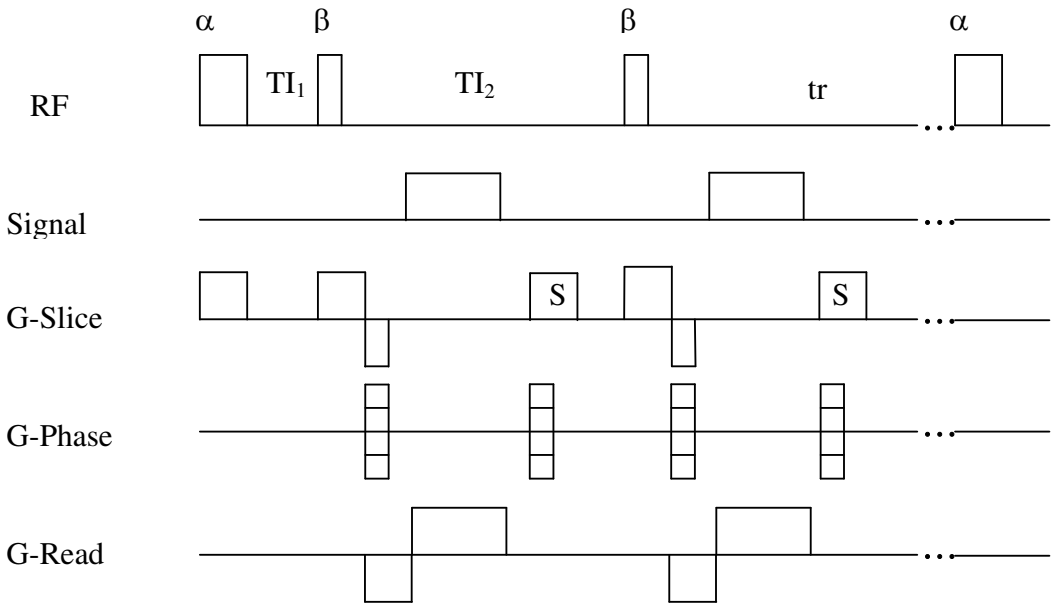

Figure 4.10: Schematic diagram of the TOMROP sequence.

state with M (0)=M (TR), where TR=TI_1+(N-1) TI_2+tr is the sequence repetition time. By calculating the longitudinal magnetization M (TR), Q can be obtained as

$$Q = \frac{FC_\alpha C_\beta E_r E_1[1-(C_\beta E_2)^{N-1}]}{1-C_\alpha C_\beta E_r E_1 (C_\beta E_2)^{N-1}} + \frac{C_\alpha E_1(1-E_r)-E_1+1}{1-C_\alpha C_\beta E_r E_1 (C_\beta E_2)^{N-1}} \ , \qquad (4.37)$$

with $C_\alpha = \cos\alpha$, $E_1 = \exp(-TI_1 / T_1)$, and $E_r = \exp(-tr / T_1)$.

M_n relaxes toward $M_\infty = M_{eq} F$ with an effective time constant

$$\tau = TI_2 / [\ln(C_\beta) - TI_2 / T_1] . \qquad (4.38)$$

The signal intensity of the n-th gradient echo image at a pixel (i,j) can be written as

$$S_n(i,j) = \left| S_\beta(i,j) M_n(i,j) \exp[-T_D / T_2^*(i,j)] \right| \qquad (4.39)$$

where $S_\beta = \sin\beta$, T_2^* is the characteristic decay constant of the FID and T_D the time between the small flip angle pulse and data acquisition. From Eq. (4.39), we can see that the theoretical signal S_n is proportional to the longitudinal magnetization M_n.

From Eqs. (4.37), (4.38), and (4.39), the two parameters T_1 and M_{eq} can be computed at each pixel by minimizing χ^2, the square of the signal difference between experimental data and calculated fit values. The quantity χ^2 is defined as

$$\chi^2 = \sum_{n=1}^{N} [(S_n - L_n)]^2, \qquad (4.40)$$

where L_n is the measured signal of the n-th gradient echo.

4.7 UNFOLD

Some dynamic applications monitor the evolution of the signal, thus acquiring data in a k-t space, which contains both temporal and spatial information. According to the Nyquist Criterion, a less dense k space coverage results in reduced acquisition time at the expense of aliasing in the image domain. Spatially distinct points within the objects are overlapped at the same position, yielding an aliased image. UNFOLD[56] (Unaliasing by Fourier Encoding the Overlaps Using the Temporal Dimension) is a method that it labels the overlapped components along t direction, and then resolves them through a Fourier transform. UNFOLD can be used to reduce the acquisition time or to increase the spatial coverage with the same acquisition time. The idea behind UNFOLD is illustrated in Fig. 4.11. If the sampling function in the phase-encoding direction is shifted by f, the point P_0 from the central peak and the point P_1 from the first peak will overlap at the same position, but the difference lies in that P_0 remains the same, and P_1 is phase shifted by an angle 2π f. In a dynamic study, the shift in the sampling function can be varied from image to image. For example, if the first

image is acquired with f=0, hence the overlapped components (P_0+P_1), and the second image is acquired with f=0.5, hence the overlapped components (P_0-P_1), and so on, then P_0 and P_1 occupy different frequencies after Fourier transform. Only the DC component remains after filtering out the high frequency components, obtaining a unaliased image. If P_0 and P_1 vary with time, their frequency spectrum is a distribution of frequencies instead of a delta function, as shown in Fig. 4.12. As long as the change is slow enough to separate their frequency distribution, which is true for most dynamic studies, UNFOLD works.

The filtered images are obtained as follows. First, raw k-space data are obtained using the reduced sampling schemes, and the missing k-space values are filled with zeros. At this time, taking the inverse (spatial) Fourier Transform produces aliased images. But we take the (temporal) Fourier transform of each pixel first, then filter out any spectral components outside the passband, and subsequently take the inverse Fourier transform to return to the temporal domain. Finally, the inverse (spatial) Fourier Transform gives unaliased images. Fig. 4.13 shows the aliased images on a phantom from half k-space coverage and the reconstructed unaliased image using UNFOLD method.

As shown in Fig. 4.12, a filter F(ω) is used to filter out the Nyquist frequency. This filter changes the SNR, by a factor f_{SNR}, which depends on the filter, since it removes the noise contained in part of the BW_2 bandwidth

$$f_{SNR} = \sqrt{\frac{BW_2}{\int_{BW2} F^2(\varpi)d\varpi}}\left(\frac{V_2\sqrt{\tau_2}}{V_1\sqrt{\tau_1}}\right) \qquad (4.41)$$

The index 1 refers to a conventional acquisition in which the whole FOV is imaged with a same temporal resolution, whereas the index 2 refers to an UNFOLD application. V

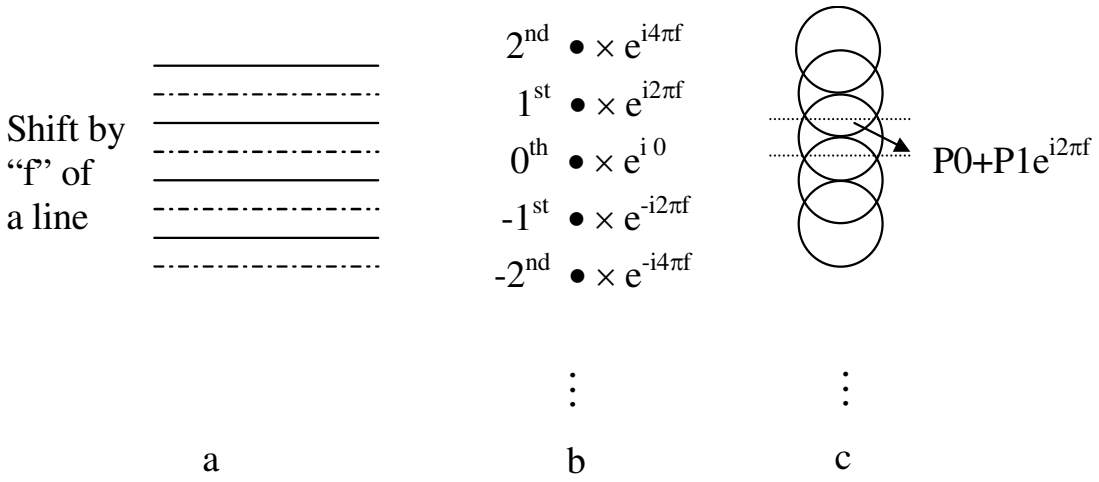

Figure 4.11: a: The sampling function is shifted along the phase-encoding direction; b: the shift generates a phase ramp in the point spread function shown in b; c: phase shifts are passed to the images in c.

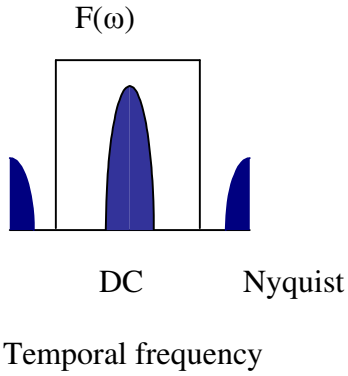

Figure 4.12: Object and aliasing components occupy different frequencies.

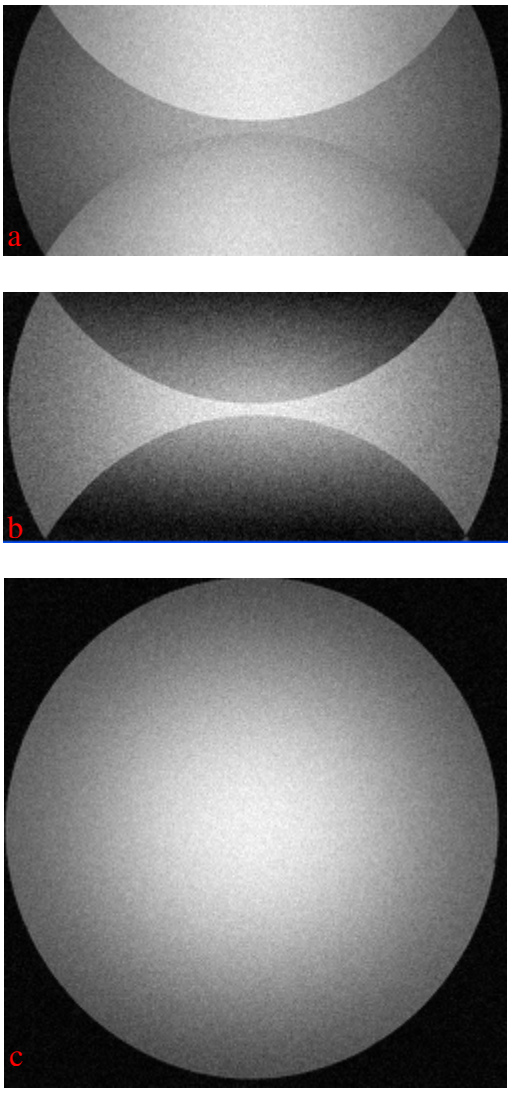

Figure 4.13: Aliased images on a phantom with half k-space coverage a: without and b: with shifting the sampling function along the phase-encoding direction; c: reconstructed image using UNFOLD method.

and τ represent, respectively, the volume of a voxel and the time spent acquiring data for a time frame. The term on the right hand side involving Vs and τs comes form well-known relationships for the signal-to-noise ratio (SNR), which I also discussed in last chapter.

Since the object is stationary, the filter used is equal to 1 over nearly the whole bandwidth BW_2, $V_2=V_1$, and $\tau_2= \tau_1/2$ (only half the ky lines are acquired for any given frame), so the above eq. (4.41) gives $f_{SNR} = 1/\sqrt{2}$, which means UNFOLD will reduce SNR by a factor of $\sqrt{2}$.

4.8 Magnetization Transfer Contrast (MTC)

Magnetization transfer between ^1H in " free" bulk water of relatively unrestricted motion (^1H_f) and ^1H in restricted motion moieties (^1H_r), such as macromolecular protein matrices and cellular membranes, is proposed to dominate water ^1H spin-lattice relaxation in biological tissues[120]. This process is schematically represented in Fig.4.14. In this model, ^1H in a surface layer of water interacts with the macromolecular matrix via chemical exchange or dipole-dipole interaction while it then communicates with the bulk water pool by diffusion[120].

The saturation transfer method can be used to study the magnetization transfer between ^1H_f and ^1H_r and to generate a unique form of NMR image contrast, magnetization transfer contrast (MTC) [120]. In this approach, the 5-10 KHz off-resonance radiofrequency (rf) irradiation from ^1H_f is effective in saturating the 20-40 KHz broad ^1H_r components with little effect on the narrow (15Hz) ^1H_f signal. With steady-state ^1H_r saturation, magnetization transfer between the ^1H_f and ^1H_r pools causes a decrease in the ^1H_f NMR signal intensity, which is related to the rate of magnetization transfer by the equation[120]

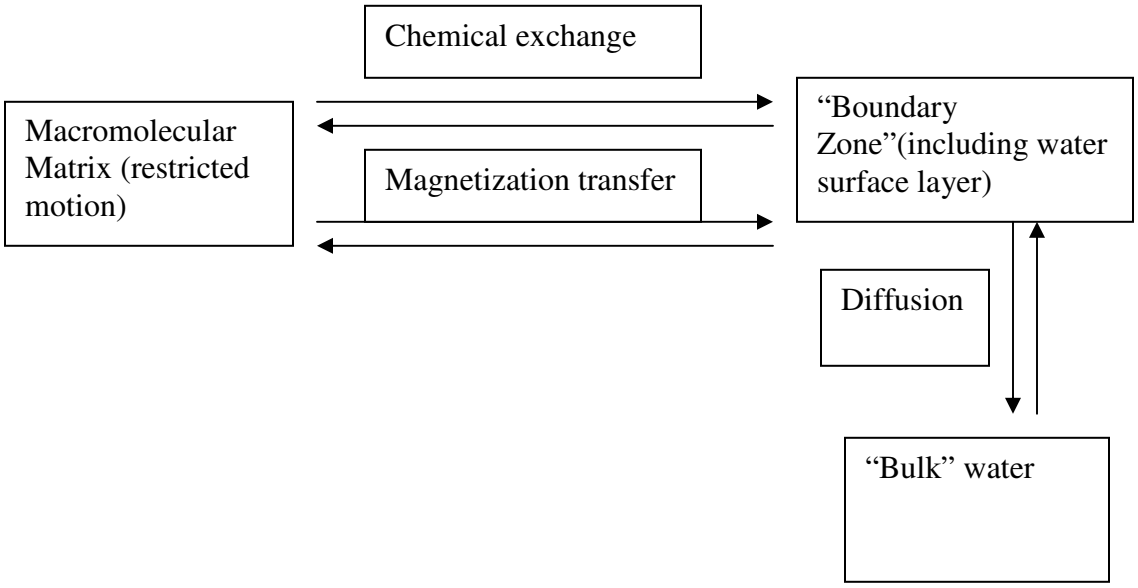

Figure 4.14: Water proton magnetization transfer in biological tissues

$$k_{for} = \frac{1}{T_{1fsat}}(1 - \frac{M_{sf}}{M_{0f}}) \qquad (4.42)$$

where k_{for} is the forward pseudo-first-order rate constant of magnetization transfer from ^1H_f to ^1H_r whether the exchange is due to chemical exchange or through space interactions, T_{1fsat} is the spin-lattice relaxation time of ^1H_f in the presence of steady-state ^1H_r saturation, and M_{sf} and M_{0f} are the ^1H_f magnetization in the presence and absence of ^1H_r saturation, respectively[120].

The effect of a given B_1 strength on either ^1H_r or ^1H_f is given by the equation[120]

$$m_{zratiou} = \frac{M_{su}}{M_{0u}} = \frac{1 + \Delta\varpi^2 T_{2uobs}^2}{1 + \Delta\varpi^2 T_{2uobs}^2 + \gamma^2 B_1^2 T_{1uobs} T_{2uobs}} \qquad (4.43)$$

where the subscript symbol u is either f or r to denote the ^1H_f and ^1H_r spins, respectively; the function $m_{zratiou}$ is the fraction of ^1H_u magnetization remaining along the z axis; M_{su} and M_{0u} are the magnetization of ^1H_u observed in the presence and absence of off-resonance irradiation, respectively; $\Delta\varpi$ is the off-resonance frequency shift (rad/s); T_{1uobs} is the observed spin-lattice relaxation time of ^1H_u; and T_{2uobs} is the observed spin-spin relaxation time of ^1H_u[120].

If the effect of chemical exchange is neglected, the magnetization for two cross-relaxed spins (e.g., via the dipole-dipole coupling) can be described by the coupled Bloch equations[121-126]

$$\frac{dM_A^z}{dt} = -(K_A + \frac{1}{T_{1A}})(M_A^z - M_A^{z0}) + \frac{K_A(M_B^z - M_B^{z0})}{F} + \varpi_1 M_A^y,$$

$$\frac{dM_B^z}{dt} = -(\frac{K_A}{F} + \frac{1}{T_{1B}})(M_B^z - M_B^{z0}) + K_A(M_A^z - M_A^{z0}) + \varpi_1 M_B^y,$$

$$\frac{dM_{A,B}^x}{dt} = -R_{2A,B} M_{A,B}^x + \Delta\varpi M_{A,B}^y,$$

$$\frac{dM_{A,B}^y}{dt} = -R_{2A,B} M_{A,B}^y - \Delta\omega M_{A,B}^x - \varpi_1 M_{A,B}^z, \qquad (4.44)$$

where $M_A^{x,y,z}$ are the x, y, and z components of the magnetization for spin A, and $M_B^{x,y,z}$ are those for spin B; $\Delta\varpi$ is the offset frequency; ϖ_1 is the spin frequency for the B_1 field along the x axis; R_{2A} and R_{2B} are the spin-spin relaxation rates for spins A and B; T_{1A} and T_{1B} are the spin-lattice relaxation times for spins A and B; and K_A and K_B are the cross-relaxation rate constants. F is the ratio of M_B^z / M_A^z at equilibrium. And K_A and K_B are related to the transition probabilities between the energy levels of the dipole-dipole coupled spins A and B in the same way. Therefore, they are proportional to each other:

$K_B=K_A/F$[122-126].

MTC between free water and protein is strongly dependent on both water content and the mobility of the macromolecular pool. Progressing ischemic infarction in the brain brings the accumulation of water and the mobilization of protein accompanying the loss of cellular structure through proteolysis; therefore k_{for} should decrease in the region of infarct[118-121].

Fig. 4.15 shows T_{1s}, T_1, M_0, M_{0s}, K_{for} and MTR ($1-M_{0s}/M_0$) map of a stroke rat with 90 min occlusion 48hrs after reperfusion. In the ipsilateral hemisphere, T_{1s}, T_1, M_0, M_{0s} increased while K_{for} and MTR decreased. Arrows point to the ischemia area.

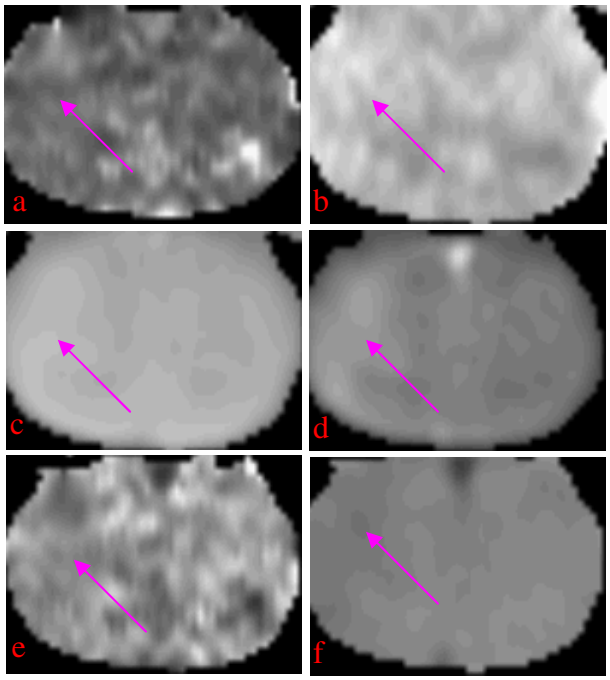

Figure 4.15: MT related maps (a) T_{1s} (b) T_1 (c) M_0 (d) M_{0s} (e) K_{for} (f) MTR of a stroke rat with 90 min occlusion 48hrs after reperfusion.

CHAPTER 5

Major Findings on SHRsp Rats

This chapter gives our preliminary results on edema formation, permeability elevation, hemorrhagic transformation and cerebral blood volume alteration with increased CPP in SHRsp rats.

5.1 Vascular Permeability and Absolute Water Content in SHRsp Rats: A Magnetic Resonance Imaging Approach

Introduction

The stroke-prone spontaneous hypertensive rats (SHRsp), established by Okamoto et al.[64], is a suitable experimental model for investigating the pathogenesis of stroke occurring as a consequence of high blood pressure and its treatment measures in humans. However, it is difficult to precisely predict the timing and the location of the lesions in SHRsp. Therefore, the pathogenesis of the damage (hemorrhage, infarct, or hemorrhagic infarct) is not univocally clear.

The pathogenesis of the brain tissue damage in severe hypertension has been debated. Recent studies strongly favor the view that vasogenic edema plays the crucial role in the development of tissue damage[59, 67], rather than thromboses or vascular spasm. The primary events in the development of brain damage include the breakdown of the blood brain barrier (BBB), leakage of plasma proteins into the vessel walls and fibrinoid degeneration in the penetrating arterioles and microvessels. Plasma constituents can leak into the brain

parenchyma through the injured BBB and, frequently, small petechial hemorrhages occur when blood cells leak out [59].

However, further studies need to be conducted concerning the onset and development of the spontaneous brain damage as well as the mechanisms responsible for the development of brain abnormalities[65, 66].

In the past, edema was studied by measuring the specific gravity of selected brain regions[60], by wet-dry method, or by acquiring T2W images. With specific gravity measurements it is possible to obtain reliable results in tissue samples as small as 1mg, but with the wet-dry method, 100-150mg tissue samples are required for accurate measurement. T2W images can define the spatial distribution and quantify the size of brain lesions better than any other imaging modality [61,153-157]. High signal on T2-weighted images originates from edema with increased water content and consequently prolonged T2 relaxation time.

The spread of plasma constituents into the brain due to breakdown of the BBB have been revealed with the use of tracers (e.g., Evans blue) or immunohistochemistry[60, 66, 67, 148].

To the best of our knowledge, MRI was used in only one study to monitor the appearance of brain damage and of altered permeability of the BBB on SHRsp rats qualitatively over time after intravenous injection of gadolinium[62]. It was reported that the leakage of contrast agent was visible in all of the SHRsp rats at the same time as hyperintense areas appeared in the T2W images. Now, both absolute water content measurements[43-46] and permeability maps[47-55] can be obtained with MRI noninvasively, thus making longitudinal study in one rat feasible.

Therefore, this study was undertaken to test the following hypothesis using a quantitative MRI approach: there is a linear relationship between permeability and water

content; and the corresponding null hypothesis: there was no linear relationship between permeability and water content.

Materials and Methods

Animals and Treatments

20 SHRsp rats obtained from Washington University were used in this study. The procedures involving the animals and their care were performed at the University of North Carolina at Chapel Hill in conformity with institutional guidelines.

SHRsp rats (n=20), fed a high-salt low-protein diet after weaning and given tap water ad libitum, were imaged weekly on a 3T SIEMENS Allegra head-only scanner with a 4.3cm birdcage coil beginning at 12 week of age and continuing for five weeks.

T1-weighted images, T2-weighted images, water content map and permeability map were acquired by using MRI on these SHRsp rats.

Theory

Water Content Measurement

Absolute water content of the rat brain, in the presence of RF inhomogeneity and flip angle miscalibration, can be measured using an MRI approach[43-46]. The principle of such an approach is introduced below.

The ideal FLASH signal is given as

$$s(\theta) = \frac{(1 - E_1)}{1 - E_1 \cos\theta} \sin\theta \qquad (5.1)$$

where $E_1 = e^{-TR/T_1}$. It can be transformed into

$$\frac{s(\theta)}{\sin\theta} = \frac{s(\theta)}{\tan\theta} E_1 + M_0 (1 - E_1) \qquad (5.2)$$

where the T^*_2 effect is ignored.

This expression implies that the data in [$x = \frac{s(\theta)}{\tan\theta}$, $y = \frac{s(\theta)}{\sin\theta}$] space can be least squares fitted to a line whose slope and intercept made with the y axis are E_1 and $M_0(1-E_1)$, respectively. Subsequently, M_0, a measure of water content, can be estimated with a known T_1.

But in practice, there are spatial variations in the RF field. If the same coil is used for both RF-transmission and reception, the RF sensitivity patterns for transmission and reception are the same. If α is used to model the spatial sensitivity variation, the signal at a given voxel ρ is scaled to $\alpha\rho$, and the flip angle is also scaled from the desired value θ to $\alpha\theta$. In addition, there is a flip angle miscalibration scaling factor α_0, which will be estimated later.

Then the signal for the nonideal case can be given as[45]

$$\rho_{nonideal}(\theta_0) = \alpha\rho_0 \sin(\alpha\alpha_0\theta_0)\frac{(1-E_1)}{(1-E_1\cos(\alpha\alpha_0\theta_0))} \qquad (5.3)$$

In order to obtain quantitative estimates of brain water content as well as to correct for T2* decay, a double echo 3D FLASH sequence was used to acquire images with five different flip angles, including 2°, 5°, 10°, 20°, and 40°. Imaging parameters were: TR = 35 ms, TE1 = 3.72 ms, TE2 = 15 ms, matrix size = 128 × 128, FOV = 32 mm^2 and 32 slices with a volume thickness of 32 mm, average=4 for 2^0 with imaging time 9'35'', average=2 for 5^0 and 40^0 with imaging time 4'48'', and average=1 for $10^0$and 20^0 with imaging time 2'25''.

First, the T2* effect is corrected based on the double echo image intensity Eqs.

$S_1=S_0\times\exp(-TE1/T2^*)$ (5.4)

$S_2=S_0\times\exp(-TE2/T2^*)$ (5.5)

where S_1 is the signal intensity of the first echo image, and S_2 is the signal intensity of the second echo image, S_0 can be obtained.

Second, to further reduce flip angle miscalibration, a single echo 3D FLASH sequence was used with five large flip angles, including 160°, 170°, 180°, 190°, 200° and 210°. Imaging parameters were: TR = 35 ms, TE1 = 3.72 ms, matrix size = 64 × 64, FOV = 32 mm^2 and 32 slices with a volume thickness of 64 mm, average=2, with imaging time 2'25'' for each flip angle.

The signal should be zero for all the tissues when the actual flip angle experienced is 180^0, and the signal behaves linearly as a function of flip-angle in the neighborhood of 180^0. The signal zero crossing can be obtained by fitting a set of high flip angle (around 180^0) signal measurements to a straight line. If the signal zero crossing occurs at θ_z, then α_0 is estimated as

$$\alpha_0 = \frac{180}{\theta_z} \tag{5.6}$$

Third, a low flip-angle (<< the Ernest angle) image of a homogeneous gel phantom with 80% water content (measured with wet-dry method) that fills the volume-of-interest in the nonideal case is described by[45]

$$\rho(r,\theta_0)\Big|_{\theta_0<<\theta_E} \approx (\alpha(r)\rho_0)(\alpha(r)\alpha_0\theta_0) \propto \alpha^2(r) \tag{5.7}$$

yielding the estimates of the spatial variations in the RF-field. That is, a relative RF-field map is the square root of the low flip-angle (2^0) image of a homogeneous object. Usually this 2^0 image has very high SNR by averaging many times since there is no time constraint for the gel phantom study.

In summary, for the nonideal case, the signal can be rewritten in the form

$$\frac{\rho_{nonideal}(\theta_0)}{\sin(\alpha_0\alpha\theta_0)} = \frac{\rho_{nonideal}(\theta_0)}{\tan(\alpha_0\alpha\theta_0)}E_1 + \alpha\rho_0(1-E_1) \qquad (5.8)$$

This expression implies that the data in [$x = \frac{\rho_{nonideal}(\theta_0)}{\tan(\alpha_0\alpha\theta_0)}$, $y = \frac{\rho_{nonideal}(\theta_0)}{\sin(\alpha_0\alpha\theta_0)}$] space can be least-squares fitted to a line whose slope and intercept made with the y axis are E_1 and $\alpha\rho_0$ (1-E_1), respectively. Subsequently, ρ_0 , a measurement of water content, can be estimated with a known T_1 and α .

Finally, an absolute estimate of brain water content is obtained by normalizing the effective spin-density of the brain to that of a water phantom.

Permeability Measurement

In order to obtain estimates of permeability, the Look-Locker (L-L) technique[57] employing the T-one by multiple read-out pulses (TOMROP) sequence was used for pixel-by-pixel estimates of T1.

The T1 maps pre contrast agent and post contrast agent at ten time points are obtained before permeability measurement. Ten time points are chosen based on two considerations. One is to make sure the uptake of the contrast agent is unidirectional during the first half-hour post contrast agent. The other is to improve the accuracy of permeability measurement. In this study, two versions of TOMROP were used to obtain T1 maps.

Before the injection of contrast agent, 20 echoes were created to sample more points along the magnetization regrowth curve due to a long T1 of blood with TR=1500ms, while 9 echoes were created after the injection of contrast agent with TR=750ms. In both cases, the small flip angle was 15^0, the time interval between the first inversion pulse and the small flip angle RF pulse was 35.46ms, and the time interval between two small flip angle RF pulses

was 60 ms. Other imaging parameters were as follows: FOV=32×32mm, matrix size=128×64, and four 2 mm slices.

Then the T1 values for blood voxel and tissue voxel both pre and post contrast (ten time points) are substituted into Eq. (5.9) to obtain the concentration curve of the blood and tissue.

$$C_{pa}(t_n) \propto \frac{\Delta R_{1a}(t_n)}{(1-Hct)} \text{ , and } C_{tis}(t_n) \propto \Delta R_{1tis}(t_n) \qquad (5.9)$$

where $\Delta R_{1tis}(t_n)$ and $\Delta R_{1a}(t_n)$ are differences in R1 measured in tissue and the jugular vein, respectively, at time t_n, and the hematocrit (Hct) is the fraction of the volume of red blood cells to the volume of whole blood, with a typical value 0.4.

In fact, $\Delta R_{1tis}(t)$ and $\Delta R_{1a}(t)$ are often used as estimates of tissue and arterial concentrations, since we generally assume that the constant of proportionality between concentration and ΔR_1 (i.e., the relaxivity) does not change across tissues, that is, the scaling constant to tissue concentration in (5.9) is the same for blood and tissue.

Finally, the PATLAK approach[48] was utilized with the images acquired using the TOMROP sequence for obtaining permeability maps for each rat.

Eq. (5.10) is utilized to obtain permeability K_i.

$$\frac{C_{tis}(t)}{C_{pa}(t)} = K_i \frac{\int_0^t C_{pa}(\tau)d\tau}{C_{pa}(t)} + V_p \qquad (5.10)$$

The Patlak plot is a graph of the ratio of the total tissue solute concentration at the sampling time $C_{tis}(t)$ to the plasma concentration at the respective times $C_{pa}(t)$ versus the ratio of the arterial plasma concentration-time integral $\int_0^t C_{pa}(\tau)d\tau$ to $C_{pa}(t)$. The abscissa has

the unit of time, but it is concentration adjusted, and therefore will be referred to as "stretch time" or $t_{stretch}$. A typical Patlak plot of proton MRI data is shown in Fig. 5.1. A Patlak plot of one voxel from the ROI with BBB leakage and one voxel from the contralateral region (normal brain) from one experiment is shown. The data points were obtained at 3-min intervals after intravenous injection of Gd-DTPA. The lines are the least-squares fit of these points, respectively. This graph will yield a curve that eventually becomes linear when a unidirectional transfer process is dominant during part or all of the experimental period. In this case, the slope of the line is K_i, and the intercept of the line is V_p.

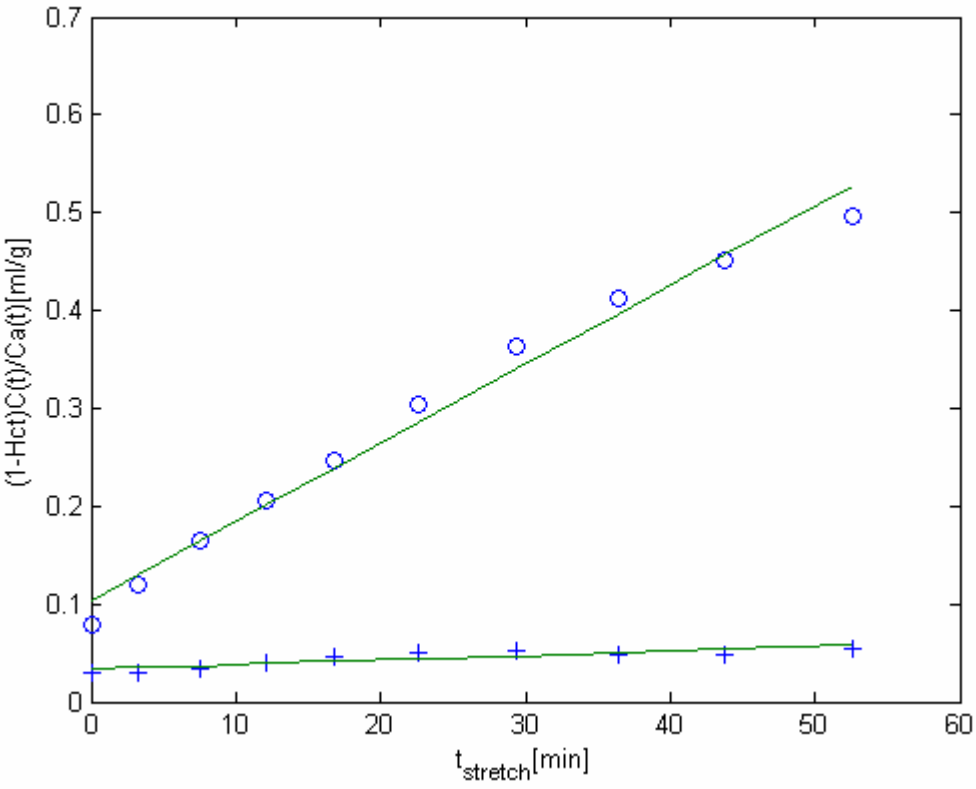

Figure 5.1: Patlak plot of the data from one voxel with BBB leakage and one voxel with normal BBB.

MRI Measurements

At each session, rats were anesthetized with isoflurane, and tail veins were catheterized for the injection of Gd-DTPA (0.15 cc/100 g) to facilitate permeability measurement.

First, A T2-weighted image was acquired using the following parameters: isotropic 32 cm field-of-view (FOV), 128x128 matrix size, 0.25 mm^3 pixel size, TR=6790ms, TE = 98 ms, and 30 slices.

Then, water content and permeability maps were obtained using the method described above.

After that, an additional dose of Gd-DTPA (0.1 cc/100 g) was injected through the tail vein, and 32 T1W slices were acquired. Contrast agent induced signal enhancement was interpreted as BBB leakage. T1W imaging parameters were: TE=2.66ms, TR= 35ms, FOV=32*32mm^2, matrix size=128*128.

Finally, in order to determine the progression of edema, all rats were divided into three groups: group A (without any abnormality on T2-weighted image), group B (with enlarged ventricle or little hyperintensities on T2-weighted image), and group C (with large hyperintensity on T2-weighted image). Typical T2-weighted images for the three groups are shown in Fig. 5.2.

ROI and Statistical Analysis

Regions of interest (ROI) analysis was employed for the measurements of brain water content as well as vascular permeability for each rat at each time point. An ROI encompassing the hyperintense area observed in permeability maps was used for vascular permeability measurements across four adjacent slices. Using mean plus two standard

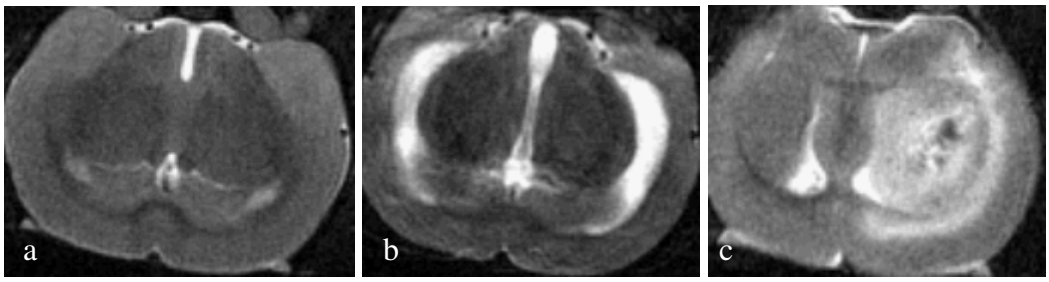

Figure 5.2: T2-weighted images from a: group A; b: group B and c: group C.

deviations of permeability of the normal hemisphere as the threshold, the mean of the ROI covering visible BBB leakage was used as the permeability. The permeability from the four slices was added together to obtain the final permeability. An ROI encompassing the whole hemisphere was used for brain water measurement across the central ten slices.

Statistical Analysis for Specific Aim 1

A linear regression model and a single-factor ANOVA were employed for specific aim 1. Both the linear regression model and the single-factor ANOVA assume independent observations of two variables, X and Y. In addition, the linear regression model assumes the residues follow a normal distribution with mean 0 and a constant variance for all values of X.

Some rats were observed more than once during this study. We assume each observation was independent since the rats were imaged weekly.

Pearson's correlation coefficient R was calculated between the two variables: water content and BBB permeability. The statistical test $T = \frac{R\sqrt{n-2}}{\sqrt{1-R^2}}$, which has a t distribution with n-2 df, was used to determine if there was a linear relationship between water content and permeability among the rats of group C with both water content increase and BBB leakage.

In addition, a single-factor analysis of variance to correct for multiple comparisons, specifically, the Turkey multiple comparison test, was employed to see the effect of intra-subject difference on the ratio of water content to permeability. Each rat with measurements at different time points was treated as a separate group. $P<0.05$ was considered to indicate significance at a 95% confidence level.

The error rate 0.05, called an experiment wise error rate, no longer refers to a particular interval, but instead refers to the experiment as a whole. This means in approximately 95% of these experiments no erroneous claim would be made about any of the intervals, whereas in only 5% would at least one incorrect claim be made. Because the confidence level for the entire set of comparisons of means is 95%, the confidence level for any particular comparison is larger than 95% and increases as the number of comparisons increases.

Results

Among the 20 SHRsp rats, 13 developed asymmetric T2 hyperintensities during the observation period, 3 remained normal before death, and 4 developed small lesions before death. Representative T2-weigthed images and the permeability map from one rat is shown in Fig. 5.3. Though the BBB breakdown usually occurs in focal area, the lesion can develop into a large area.

The lesions on T2W MRI were characterized by hyperintense pixels as a result of T2 prolongation. T2 prolongation, a sensitive MRI indicator of cerebral injury, is associated with edema. Occasionally, hyperintense pixels were combined with hypointense pixels, the latter resulting from T2 reduction, indicating hemorrhage, as shown in Fig. 5.4. T2 reduction is consistent with the paramagnetic effects of deoxyhemoglobin.

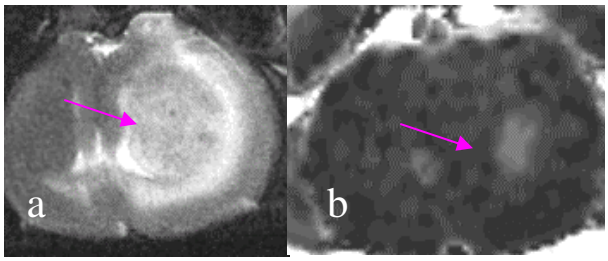

Figure 5.3: a: A T2-weighted image and b: the corresponding permeability map.

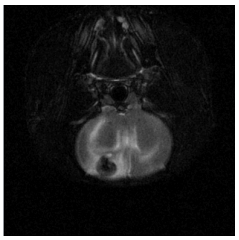

Figure 5.4: A T2-weighted image of one rat with hemorrhage.

Fig. 5.5 shows the lesion progression of one rat during the 5 consecutive weeks. Consistent with previous reports[59-62], lesion mainly developed from the cortex or the striatum. Then, via the white matter, edema spread along a pressure gradient from the lesioned gray matter to the white matter, sometimes even reaching the contralateral hemisphere via the corpus callosum, and further into the cerebrospinal fluid (CSF) spaces.

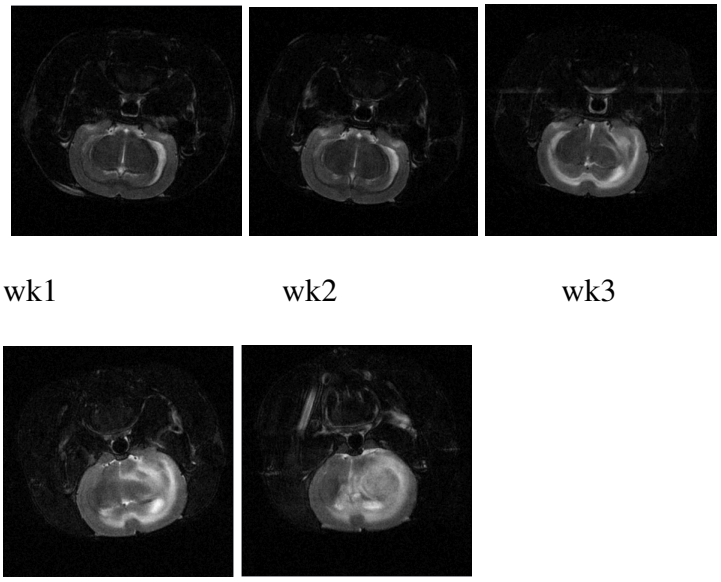

Figure 5.5: T2-weighted images of one rat during the five consecutive weeks.

BBB impairment can be shown as hyperintensity on T1-weighted images after gadolinium administration[62], while permeability maps gave an absolute permeability value. Extravasation of contrast agent was visible in all the salt-loaded SHRSP at the same time as hyperintensive areas appeared in the T2W images (Fig. 5.3). The onset of gadolinium enhancement was usually detectable inside the hyperintensive area corresponding to vasogenic edema.

Among the 20 SHRsp rats, 13 developed asymmetric T2 hyperintensities during the observation period. Among the 13 rats, 4 rats died during the experiment without the corresponding permeability measurement, and thus were excluded from the data analysis. Fig. 5.6 and Fig. 5.7 show the temporal evolution of brain water content and the vascular permeability of the 9 rats over the 5-week observation period. It is evident that the brain

water content continues to increase. In contrast, a minimal increase in permeability is observed in 1 of 9 rats while the remaining 8 rats exhibit a substantial elevation of permeability. In addition, Fig. 5.8 shows the mean and standard deviation of the water content for the three groups, with group A $78.52 \pm 1.15\%$ (n=32), group B $78.9 \pm 0.91\%$ (n=9), and group C $81.1 \pm 1.76\%$ (n=25). The brain water content in group C is significantly higher than the brain water content in group A ($p<0.05$), and than that in group B ($p<0.05$), while there is no significant difference in brain water content between group B and group A ($p>0.05$).

Results for Specific Aim 1

Finally, Fig. 5.9 shows the relationship between the permeability and the water content for group C. Statistical test $T = \frac{R\sqrt{n-2}}{\sqrt{1-R^2}}$ has a t distribution with n-2 df. With $R^2=0.3413$, n=19, $T=2.97>T_{0.025,\ 17}=2.1$, therefore, there is a linear relationship between the water content and the permeability ($r=0.584$, $p<0.05$). $R^2=0.3413$ means permeability only explains 34.13% of the observed variation of the water content. From ANOVA analysis, no significant inter-subject difference was found in the remaining eight rats except in one rat with only one observation. This was probably caused by the sensitivity of the measurement methods.

Discussion

MRI allows longitudinal, noninvasive examination of the brain. In this study, 20 SHRsp rats were imaged weekly for five weeks to quantitatively analyze the progression of cerebral edema, providing a powerful technique for future studies.

The Validity of the MRI Method to Measure Water Content in Specific Aim 1

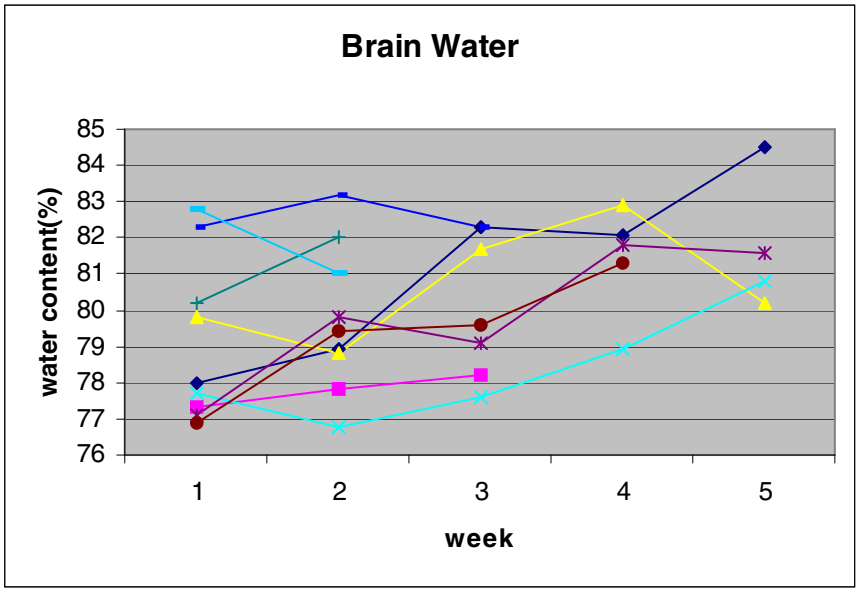

Figure 5.6: The temporal evolution of brain water content of different rats.

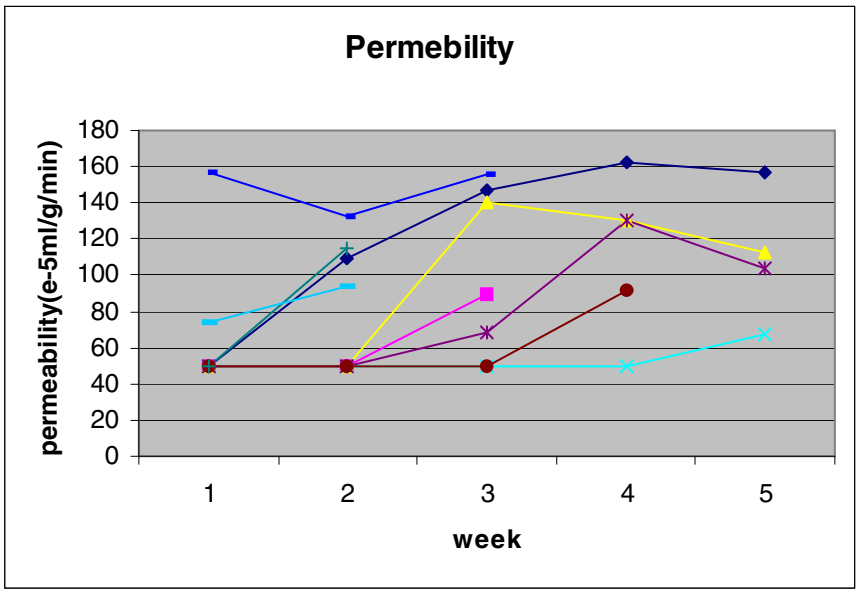

Figure 5.7: The temporal evolution of permeability of different rats.

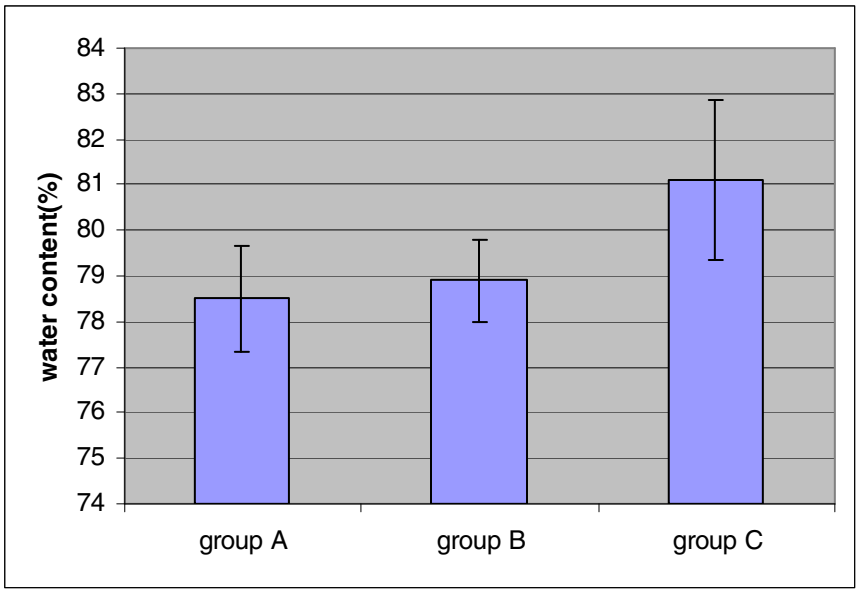

Figure 5.8: Water content of rat brain of group A, group B and group C. Error bars are the standard deviation of the intra-subject variability.

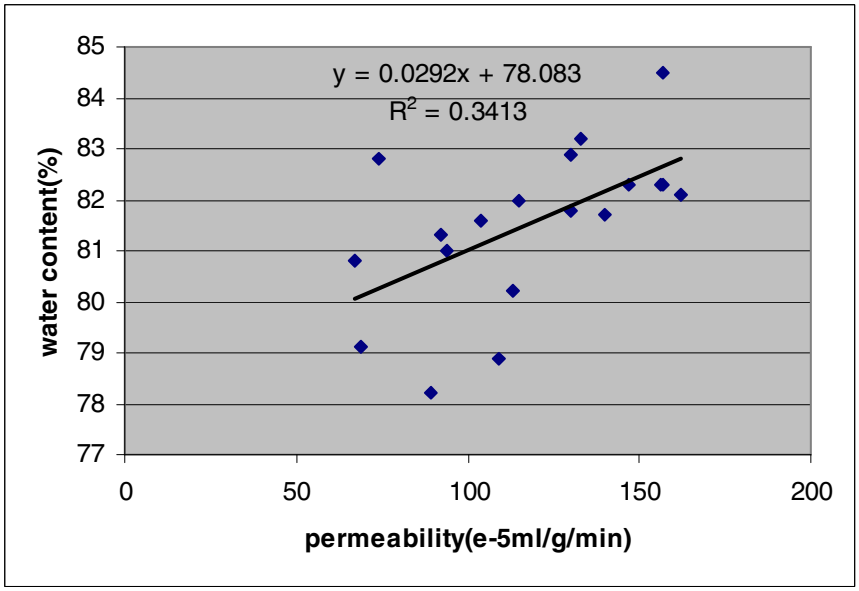

Figure 5.9: Relationship between water content and permeability of rats in group C.

Lin[44] et al. reported the mean rat brain water content obtained from the normal hemispheres was $80.1 \pm 0.6\%$ from the wet/dry measurements and $78.7 \pm 2\%$ from the MRI measurements. Our results show the mean water content for the normal rat group is $78.52 \pm 1.15\%$(n=32), agreeing well with their reports and therefore validating the MRI method to measure water content in both accuracy and precision.

The Sensitivity of the MRI Method to Measure Water Content

To investigate whether the observed spatial variation in the water content map is caused by the noise in the acquired images or is indicative of physiologic variations, the error of the water content, 4.3%, based on Monte Carlo simulation was compared with the experimentally measured variability 4.8%. Because the experimentally measured variability is only slightly higher than that obtained from the simulation, the results suggest that the observed spatial variation in the water content map is likely to be dominated by noise with relatively little effects from physiologic variation.

The Validity of MRI Method to Measure Permeability in Specific Aim 1

Knight[160] et al. estimated the blood-to-brain transfer constants for identical non-labeled and radio labeled versions of the Gd-DTPA tracer compounds for both MRI and quantitative autoradiographic (QAR) methods. Their results indicate a high degree of correlation between MRI and QAR methods with a R^2 value of 0.926 and a p-value of 0.002, thus validating the Patlak methodology for estimating BBB permeability.

Our parameters are different from theirs in TR and the number of echoes used. However, when checked visually, our MRI data in ROI with BBB leakage showing no systemic nonlinearity indicates the uni-directional uptake of the contrast agent is maintained during the experimental period.

For the contralateral ROIs chosen as controls, the mean Gd-DTPA transfer constant was $(0.5 \pm 0.2) \times 10^{-3} mlg^{-1} min^{-1}$. This immeasurably low K_i is consistent with that reported by Ewing[48] et al. ($(0.62 \pm 1.88) \times 10^{-3} mlg^{-1} min^{-1}$). Therefore, K_i calculated from Gd-DTPA MRI data by Patlak plots is reliable.

The Sensitivity of the MRI Method to Measure Permeability

For the contralateral ROIs chosen as controls, the mean Gd-DTPA transfer constant was $(0.5 \pm 0.2) \times 10^{-3} mlg^{-1} min^{-1}$ from experimental measurements and was $(0.74 \pm 0.13) \times 10^{-3} mlg^{-1} min^{-1}$ from Monte Carlo simulation. If we use the mean plus 2 standard deviations as the threshold, in both cases, permeability below (90-100) $\times 10^{-3} mlg^{-1} min^{-1}$ was not detectable with the current sensitivity.

Generally there is no brain water content increase when BBB remains intact. The brain abnormality detected by the T2-weighted image with a significant water content increase occurs at the same time as the BBB leakage, suggesting the important role of BBB leakage to the onset of the edema. Besides, a significant ($p<0.05$) relationship exists between the accumulation of water and the permeability to Gd-DTPA during the edema formation, thus disproving the null hypothesis in specific aim 1 that there was no linear relationship between water content and permeability. To maintain the uni-directional uptake of the contrast agent, the experiment should be finished within about half an hour. Within this time, only four slices with slice thickness=2mm can be obtained with satisfactory signal to noise ratio. This may be one of the reasons causing the weak linear relationship between permeability and water content. The correlation suggests movement of water into brain tissue could have been facilitated by the increase in cerebrovascular permeability to such small molecules as Gd-DTPA. Our results are consistent with the finding[66] that the edema in the

SHRsp rats fed with the Japanese diet and exposed to 1% NaCl develops as vasogenic edema (increase in absolute extracellular water content). Previous reports[66] showed that the edema developed in SHRsp rats was of vasogeinc nature without the phase of the cytotoxic edema (the transfer of water from the extracellular space into the cells due to cellular energy failure) [66] since both T2 and ADC values increased at the onset of cerebral damage. Edema was caused by BBB breakdown[62], which was believed to result from a very high blood pressure[152]. Our results showed that once BBB broke down, it remained open, probably due to the presence of high blood pressure.

Previous reports[13-20] showed that with a permanent occlusion model, water content in ischemic brain tissue increased significantly as early as 1 hour after MCA occlusion, while BBB permeability to serum protein or sucrose remained intact for at least several hours after an ischemic insult. After the BBB broke down, there was a significant correlation between the accumulation of brain water and the increase in BBB permeability to ^{14}C-sucrose instead of ^{125}I-BSA (bovine serum albumin), indicating that disruption of the blood-brain barrier to small molecules is accompanied by accumulation of edematous fluid during the later stages of ischemia. The early accumulation of edematous fluid is associated with hydrostatic and osmotic pressure gradients. Increased intraluminal pressure can increase water content further.

If we compare our SHRsp model to a permanent occlusion model, we can see there is no brain water content increase before BBB breakdown, even with an elevated MAP in the SHRsp model. In SHRsp rats, there is no water content increase even with an increased pressure gradient, possibly reflecting the low conductivity of the capillary with an intact BBB. Water movement is decided by not only the pressure gradient between arterial pressure and

tissue, but also the hydraulic conductivity of the capillary. In the permanent occlusion model, water content increases in the core as early as 1hr after occlusion, however, no water content increases in the periphery 3hr after occlusion though the pressure gradient is higher in the periphery than in the core. Edema forms when cerebral blood flow falls below a critical threshold for membrane failure, or enough time elapses with a blood flow higher than the threshold for membrane failure[14-17].

However, water content increase is significantly correlated with the permeability to small molecules after BBB breakdown in both of these two models, indicating the important role of BBB leakage detected by small molecules to edema accumulation in these two models.

In addition, the increased vascular permeability appears to be highly focal while the spatial extent of brain edema encompasses almost the entire hemisphere. This may not be surprising since severe focal BBB damage can result in a large lesion with water leaking into extravascular space.

Besides, when compared with previous reports, we observed both single focus BBB breakdown [61, 62, 65], and multiple foci BBB breakdown [60, 67, 158]. The spread pattern is also consistent with previous reports. Lesions mainly developed from gray matter (GM) of the cortex or in the striatum. Then via the white matter, edema spread through the whole hemisphere, sometimes even reaching the contralateral hemisphere via the corpus callosum.

Our findings indicate that no rt-PA should be given for a hypertension stroke in a patient with a detectable lesion on T2-weighted image, since the BBB is already broken down in this case.

In summary, the temporal and spatial relationship between permeability and water content suggests that, at first, when BBB remains intact, there is no significant water content

increase. Later, water content increase is always associated with a higher permeability, indicating severe BBB damage, which may imply vascular walls have necrotized and ruptured. Besides, there is a significant correlation between the accumulation of water and the permeability to Gd-DTPA during the edema formation. Movement of water into brain tissue could have been facilitated by the increase in cerebrovascular permeability to such small molecules as Gd-DTPA. By quantifying the BBB damage and lesion formation dynamics, the progression of the lesion development can be better understood.

This study provides a picture of water content and permeability changes occurring in SHRsp rats as brain abnormalities progress. The findings may be useful in evaluating strategies aimed at controlling the progression of brain damage.

5.2 Vascular Permeability May Spatially Predict Subsequent Hemorrhages in Stroke-prone Spontaneous Hypertensive Rats

Introduction

Increases of vascular extravasations of MR contrast agent have been implicated to be predictive of hemorrhagic transformation in acute stroke patients. The SHRsp rat is a suitable experimental model for investigating the pathogenesis of stroke occurring as a consequence of high blood pressure. Although blood-brain-barrier (BBB) breakdown, cerebral edema, and hemorrhage have been well described in this model, the spatial and temporal relationship between these events has not been well delineated. In the present study we serially imaged a cohort of SHRsp rats using MRI.

To test the hypothesis in specific aim 2: in SHRsp rats, BBB breakdown detected by Gd occurs no later than hemorrhage, since Gd is much smaller than red blood cells, with the corresponding null hypothesis: hemorrhage occurs before BBB breakdown detected by Gd.

Methods and Materials

SHRsp rats (n=12), fed a high-salt low-protein diet after weaning, were imaged weekly on a 3T SIEMENS Allegra head-only scanner beginning at 12 weeks of age and continuing for five weeks. At each session rats were anesthetized with isoflurane, and tail veins were catheterized for the injection of Gd-DTPA (0.15 cc/100 g) to facilitate permeability measurement. Three sequences were used to acquire images, including a T2-weighted, a T2*-weighted, and a turboFLASH sequence. The acquired T2-weighted images provided both anatomical data as well as an indication of brain edema. The imaging parameters for the T2-weighted sequence were: isotropic 32 cm field-of-view (FOV) and 128×128 matrix, 0.25 mm3, TR=6790ms, TE = 98 ms, 30 slices, and 11 minute imaging time. T2*-weighted images allowed assessment of hemorrhage and were acquired using a 3D gradient echo sequence with the following imaging parameters: TR=35msc; TE=25ms; 256x256; TH=0.4mm; and FOV=43x43 mm^2. In order to obtain estimates of permeability, the Look-Locker (L-L) technique employing the T-one by multiple read-out pulses (TOMROP) sequence[57] was used for pixel-by-pixel estimates of T1. For the TOMROP sequence, a TI of 40 ms was used and a total of 20 and 9 echoes were acquired before and after the injection of contrast agent, respectively. Other imaging parameters for the TOMROP sequence were as follows: matrix size was 128×64, FOV 32×32 mm^2 and four 2 mm slices. The TOMROP sequence was repeated 10 times post-contrast. Finally, the PATLAK approach[48] was utilized with the images acquired using the TOMROP sequence for obtaining permeability maps for each rat.

Statistical Analysis

Fisher's Exact test was used to reject the null hypothesis: there was no difference in the probability of hemorrhage with or without BBB breakdown detected by Gd-DTPA.

In addition, probability was calculated to reject the null hypothesis that hemorrhage occurs before BBB breakdown detected by Gd-DTPA.

Justification of Fisher's Exact test

χ^2 test is used to compare the distribution of a categorical variable in a sample with the distribution of a categorical variable in another sample.

A special form of the χ^2 test, called a "fourfold table" or "2*2 contingency table" is applicable when two groups with two cases within each group are compared.

In fourfold tables, a χ^2 test is inappropriate if the total of the table is less than 20. In this case, Fisher's Exact test should be used as an alternative to the χ^2 test for fourfold tables.

Results

Among the 12 rats, 10 rats developed asymmetric T2 hyperintensities by 14 weeks of age; 5 rats developed 7 regions of intracerebral hemorrhage (detected by T2*) at later time-points; the other 5 rats did not develop hemorrhage even with damaged BBB, probably due to the limited observation period. We believe they would have developed hemorrhage later. Four hemorrhages were located within the striatum; three were located in the cortex. All rats that developed spontaneous hemorrhages demonstrated concurrent or prior vascular permeability (determined by Gd as described above) at the site of the hemorrhage. In 4 of the 7 hemorrhages, visible hyperintensity on the permeability map was found prior to the detection of hemorrhage, preceding it by up to 2 weeks. The remaining three temporally coincided with the hemorrhage.

Therefore, 10 rats with BBB leakage developed hemorrhage, no rats with BBB leakage did not develop hemorrhage, no rats without BBB leakage developed hemorrhage, and 2 rats without BBB leakage did not develop hemorrhage. In this case, P=0.015 (<0.05) for the Fisher's Exact test, thus rejecting the null hypothesis: there was no difference in the probability of hemorrhage with or without BBB breakdown detected by Gd-DTPA.

In addition, P (BBB leakage no later than hemorrhage)=10/10>0.95, and P (hemorrhage before BBB leakage)=0/10<0.05, thus rejecting the null hypothesis that hemorrhage occurs before BBB breakdown detected by Gd-DTPA.

To show the temporal evolution of vascular permeability, T2 and T2* images of a representative rat are shown in Fig. 5.10. It is immediately evident that the presence of vascular leak precedes the hemorrhage by one week.

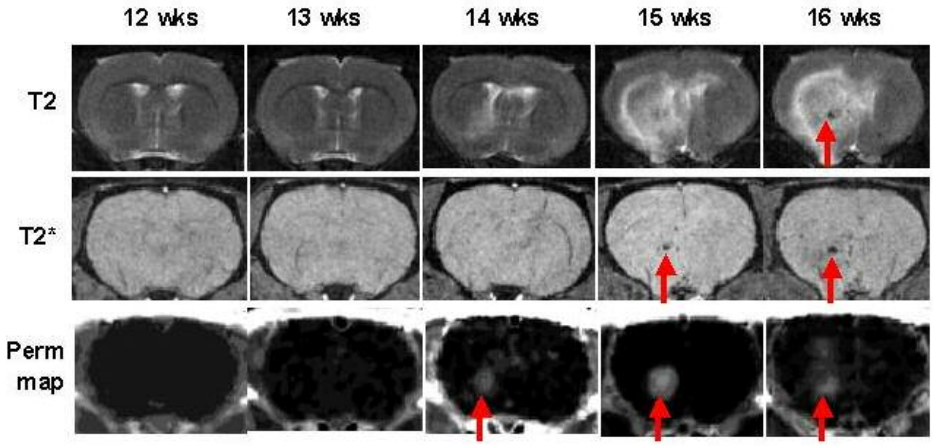

Figure 5.10: The temporal evolution of T2-weighted images, $T2^*$-weighted images, and permeability maps of a representative rat.

Discussion

The spatial and temporal relationship between BBB breakdown and hemorrhage was studied using the SHRsp model. The increased vascular permeability preceded 4 of 7 hemorrhages, and appeared concurrently with the other 3 hemorrhages. Regions of increased permeability coincided with the area of subsequent hemorrhage in all cases. These data suggest that hypertensive intracerebral hemorrhage is preceded by focal vasculopathy resulting in breakdown of the BBB. P(BBB leakage no later than hemorrhage)=10/10>0.95, and P(hemorrhage before BBB leakage)=0/10<0.05, thus disproving the null hypothesis in specific aim 2 that hemorrhage occurs before BBB leakage. Given the fact that Gd-DTPA is smaller than blood cells, Gd should leak out through damaged BBB before blood cells leak out, resulting in hemorrhage. The concurrency of increased permeability and hemorrhage may be due to the poor temporal resolution of our imaging scheme.

5.3 Regional Cerebral Blood Volume Alteration in Stroke-Prone Spontaneous hypertensive Rats

Introduction

Cerebral vessels are capable of altering their diameters in response to pathophysiological conditions. The cerebral blood volume (CBV) change can reflect this autoregulatory ability. Little is known about the cerebral blood volume (CBV) change in SHRsp rats. In this study, we serially imaged a cohort of SHRsp rats using MRI to obtain quantitative regional cerebral blood volume maps and permeability maps in order to delineate brain vascular alteration in response to hypertension, to better understand the progression of hypertensive cerebral pathology, and to determine if CBV change precedes blood-brain barrier (BBB) breakdown or vice versa. This study was undertaken to test the hypothesis in specific aim 3: under hypertensive conditions, CBV should decrease before BBB breakdown

to maintain constant CBF due to the autoregulatory mechanism, with the corresponding null hypothesis: there is no CBV change under chronic hypertension.

Methods

SHRsp rats (n=8), fed a high-salt low protein diet after weaning, were imaged weekly on a 3T SIEMENS Allegra head-only scanner with a 4.3cm birdcage coil beginning at 12 weeks of age and continuing for 4 weeks. At each session, rats were anesthetized with isoflurane, and tail veins were catheterized for the injection of Gd-DTPA to facilitate permeability and CBV measurement. A T2-weighted image was acquired using the following parameters: 32cm field of view (FOV), 128*128 matrix size, slice thickness=1mm, TR=6790ms, TE=98ms, and 29 slices. Pre- and post-contrast T1-weighted images were acquired with imaging parameters: TR=30ms, TE=2.66ms, matrix size=128*128, flip angle=35^0, average=2, FOV=$32mm^2$ and 32 slices with a volume thickness of 32mm. The T1-weighted images obtained prior to and after the injection of Gd-DTPA were used for obtaining CBV using the steady state approach[113]. The permeability was measured using our previously proposed approach[48]. CBV value was measured in 4 regions of interest (ROI1 left cortex, ROI2 left subcortical area, ROI3 right subcortical area, ROI4 right cortex) of each rat at each time point. If BBB breakdown was observed based on the permeability maps, no CBV was measured in regions of BBB breakdown.

Statistical Analysis for Specific Aim 3

The rats were divided into three groups: normal, with enlarged ventricles/weight loss, and with T2 lesions.

A single-factor analysis of variance to correct for multiple comparisons, specifically, the Turkey multiple comparison test, was used for the comparison of CBV between different

groups for all 4 ROIs and normal CBV at different time points for all four ROIs. $P<0.05$ was considered to indicate significance at a 95% confidence level.

Results

A representative T2-weighted image, a T1-weighted image pre and post contrast, and a permeability map are shown in Fig. 5.11. Two rats developed stroke during the first week, one developed stroke during the second week, two had enlarged ventricles, and the remaining three showed no abnormality on T2-weighted image. CBV of four ROIs at three different stages: normal, with enlarged ventricle/weight loss, and with T2 lesions, is shown in Fig. 5.12. There is significant decrease of CBV ($p<0.05$) for all ROI2 and ROI4 in rats with enlarged ventricle/weight loss when compared with normal rats. In rats with a lesion, there is no significant difference of CBV in ROI2 and ROI4, but a significant increase in ROI1 is seen when compared with normal rats. Fig. 5.13 shows the CBV change of different areas at different time points in the normal rats. Basically, CBV decreases gradually as function of time, but no significant difference was found.

Discussion

The Validity of the CBV Measurement in Specific Aim 3

Lin[161] et al. reported the baseline rCBV for the whole rat brain was $2.40\% \pm 0.34\%$ (n=21), in good agreement with literature values using alternative techniques. Our CBV in normal rats was $4.2\% \pm 0.5\%$ (n=52 ROIs). The difference may be due to different imaging parameters, different contrast agent doses. However, the main focus of our study is to investigate the CBV change.

The Sensitivity of the CBV Measurement

Based on the error propagation law, the standard deviation of CBV from noise is 1.67% with

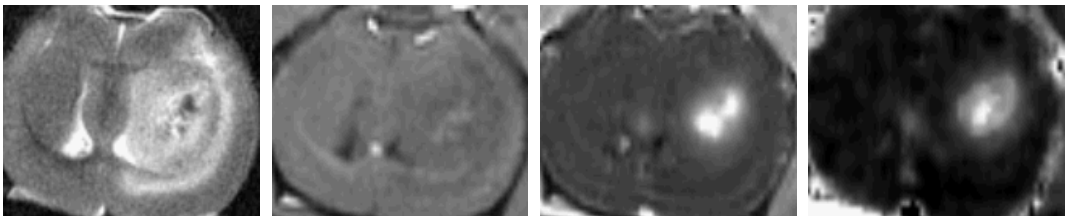

Figure 5.11: Representative T2-weighted image, T1-weighted image pre and post contrast, and permeability map.

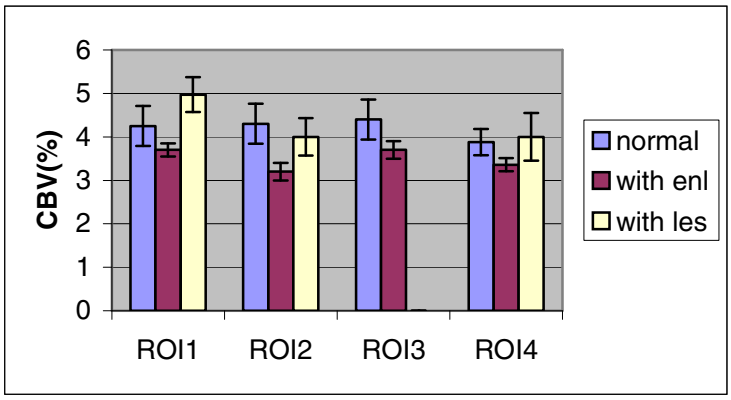

Figure 5.12: CBV values of four ROIs at three different stages: normal, with enlarged ventricle/weight loss, with lesions.

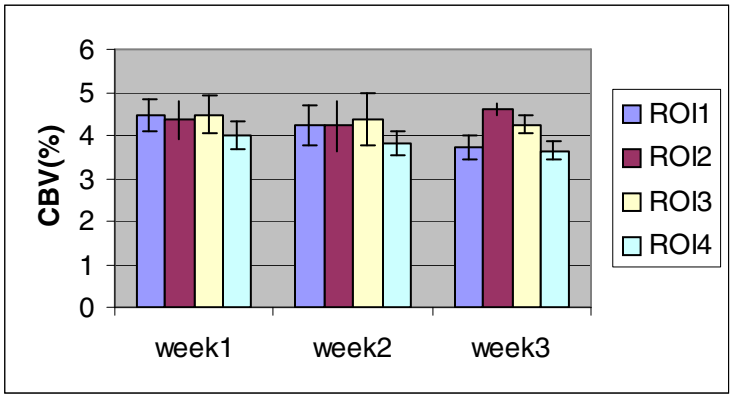

Figure 5.13: CBV alteration of different areas at different time points in the normal rats.

the signal-to-noise measured from the experimental data. In contrast, the standard deviation of the whole brain CBV can be obtained as 3.4%, and the SD of CBV from spatial variation is 3%. The comparison indicates that the spatial variation contributed more to the CBV variation than noise.

The regional CBV alteration in relation to BBB breakdown was studied. Cerebral vessels are capable of altering their own diameter in response to pathophysiological conditions. Brain arterioles constrict when the systemic blood pressure is raised and dilate when it is lowed. Under hypertensive conditions, the upper limit of CBF auto-regulation is shifted to a higher pressure.

SHRsp rats develop malignant hypertension on a high-salt, low-protein diet (Japanese diet), and the mean arterial pressure (MAP) continues to increase with time. BBB breakdown is believed to result from high blood pressure at about 200mmHg[152].

When the rats were still normal, there was no significant CBV change. When the rats had enlarged ventricles or weight loss, CBV decreased significantly with $p<0.05$ in two ROIs, indicating the increase of blood pressure, thus disproving the null hypothesis in specific aim 3 that there was no CBV change under hypertensive conditions before BBB breakdown. When the rats developed lesions with BBB breakdown, MAP should be very high, however, CBV was normal or even increased, indicating the blood pressure was already beyond the autoregulatory range, and the vessels were passively dilated with blood pressure accordingly.

Based on the studies described above, we can see the big picture of the progress of stroke in SHRsp rats.

When the rats were normal, there was no significant CBV change. When the rats had enlarged ventricles or weight loss, CBV decreased significantly, indicating the increase of

blood pressure. The cerebral blood vessels constricted to maintain constant CBF with increased MAP through the autoregulatory mechanism. When the rats developed lesions with BBB breakdown, MAP should be very high, however, CBV was normal or even increased, indicating the blood pressure was already beyond the autoregulatory range, and the vessels were passively dilated with blood pressure accordingly.

Before the BBB breakdown, there was no water content increase. The disruption of BBB is believed to result from high blood pressure at around 200 mmHg[152]. The edema developed as vasogenic edema since it occurred at the same time as BBB breakdown. Usually the BBB broke down in one area, and remained open for the study period. Lesions developed from the cortex or the striatum, and spread through the whole hemisphere, sometimes even reaching the contralateral hemisphere via the corpus calllosum. It was found there was a significant correlation between the accumulation of water and the permeability to Gd-DTPA during the edema formation. Movement of water into brain tissue could have been facilitated by the increase in cerebrovascular permeability to such small molecules as Gd-DTPA.

In some cases, the hemorrhage occurred as the red blood cells leaked out of the blood vessel. The increased vascular permeability preceded or appeared concurrently with the hemorrhages. Regions of increased permeability coincided with the area of subsequent hemorrhage in all cases. These data suggest that hypertensive intracerebral hemorrhage is preceded by focal vasculopathy, resulting in breakdown of the BBB. Given the fact that Gd-DTPA is smaller than blood cells, Gd should leak out through damaged BBB before blood cells leak out to form hemorrhage. The concurrency of increased permeability and hemorrhage may be due to the poor temporal resolution of our imaging scheme.

However, damaged BBB does not necessarily result in hemorrhage, indicating BBB breakdown is only one of the mechanisms for hemorrhage formation.

The main drawback of this study is that we did not measure the blood pressure of each rat at each time point. Otherwise the intra-animal difference and the underlying mechanism for stroke development could be better explained.

CHAPTER 6

Temporal and Spatial Relationship Between Water Content and Permeability in the Suture Model

While the previous chapter gives the findings in SHRsp rats with increased CPP, this chapter introduces the results on suture model with decreased CPP.

Introduction

Normal function of the BBB is altered by ischemia. An increased permeability of the BBB is associated with severe ischemic injury, occurring with some delay after the insult. Previous studies[13-20] have reported that the integrity of the BBB is preserved at 3-4 h after middle cerebral artery occlusion (MCAo), but that progressive BBB disruption occurs following 6h of ischemia, while the water content of the rat brain can increase as early as 30min after impairment of blood supply.

Reperfusion of tissue after transient ischemia accelerates the development of abnormal vascular permeability, which depends on the duration of occlusion and extent of CBF reduction and worsens postischemic edema[21-36]. Kuroiwa[28] et al. demonstrated a biphasic opening of the BBB after 1h of transient MCAo, occurring first at 15 min after release of vascular occlusion, then at 5h and 72h of recirculation. Belayev[24] et al. reported that an initial, acute disruption of the BBB occurs between 3 and 5 h following MCAo with a suture model of 2h temporary occlusion, and that a later increase in regional BBB permeability is present at 48h.

However, how altered vascular permeability affects the formation of edema in ischemic tissue subjected to reperfusion is unknown. Stimulated by our recent findings in SHRsp rats with increased CPP that there is a linear relationship between water content and permeability, our present experiment was designed to study how changes in BBB function relate to the formation of edematous fluid under ischemic conditions with decreased CPP. We sought to clarify the relation between the brain water content and BBB permeability to such small molecules as Gd-DTPA with a suture model of 90 min occlusion.

In summary, this study was carried out to test the hypothesis in specific aim 4 that there was a linear relationship between water content and permeability in the suture model, with the corresponding null hypothesis: there was no linear relationship between water content and permeability.

Materials and Methods

Animal Preparation

In total, 17 Long Evans rats were studied. Transient focal cerebral ischemia was induced via intraluminal occlusion of the MCA with a nylon filament. A brief description of the surgical procedure for suture model[38-42] is given below.

The right common carotid artery and external carotid artery were exposed through a ventral midline incision. After the right proximal external carotid artery is permanently ligated, a 4-0 nylon monofilament is advanced into the internal carotid artery through an arteriotomy of the common carotid artery ~3mm below the carotid bifurcation, roughly 20-22 mm until reaching the proximal anterior cerebral artery to block the origin of the MCA. After a suture was inserted, the neck incision was closed. The rats were then returned to their cages. Rats that did not demonstrate a right upper paresis after recovering from anesthesia suggested

insufficient occlusion, and were thus excluded from further study. Ischemia lasted 90 minutes by keeping the suture in place and reperfusion was achieved by withdrawing the suture from the internal carotid artery to the common carotid artery.

At each session, rats were anesthetized with isoflurane, and tail veins were catheterized for the injection of Gd-DTPA (0.15 cc/100 g) to facilitate permeability measurement.

Experimental Procedures after Reperfusion

All animal protocols were approved by the Institutional Animal Review Committee of the University of North Carolina at Chapel Hill. All images were acquired on a Siemens 3T Allegra head only scanner (Siemens Medical Inc., Erlangen, Germeany). A small animal birdcage coil (Nova Medical Inc., Ma, USA) was used as the transmitter/receiver coil.

The rats were divided into two groups: group A and group B. In group A, water content was measured shortly after reperfusion, then followed by permeability measurement. 24 hr after reperfusion, T2-weighted images were acquired to show the final lesion. In group B, 1hr after reperfusion, permeability and water content were measured. Then water content was measured 4hr and 6 hr after reperfusion. Between the experiments, the rat was taken out, and allowed to awake from anesthesia. Finally, 24 hours after reperfusion, water content and permeability were measured. Group B was divided into two subgroups: group B1 with BBB leakage and group B2 without BBB leakage.

T2-weighted Image

T2-weighted images were acquired using the following parameters: isotropic 32 cm field-of-view (FOV), 128x128 matrix size, TR=6790ms, TE = 98 ms, and 30 slices.

Measurement of Water Content and Permeability

The methods to measure water content and permeability have been described in detail in the previous chapter.

T1-weighted Image

After that, an additional dose of Gd-DTPA (0.1 cc/100 g) was injected through the tail vein, and 32 T1W slices were acquired. Contrast agent induced signal enhancement was interpreted as BBB leakage. T1W imaging parameters were: TE=2.66ms, TR= 35ms, FOV=32*32mm^2, and matrix size=128*128.

Statistical Analysis for Specific Aim 4

For simplicity, the water content was expressed as ipsilateral/contralateral ratios. A single-factor analysis of variance to correct for multiple comparisons, specifically, the Turkey multiple comparison test, was used for the comparison of the water content. Group B1 and B2 at different time points were treated as separate groups. $P<0.05$ was considered to indicate significance at a 95% confidence level.

The rats were observed at 1hr and 24hr after reperfusion during this study. We assume each observation was independent.

Pearson's correlation coefficient R was calculated between the two variables: water content and BBB permeability. The statistical test $T = \frac{R\sqrt{n-2}}{\sqrt{1-R^2}}$, which has a t distribution with n-2 df, was used to determine if there was a linear relationship between water content and permeability.

Results

Due to the heterogeneity of the ischemic lesion produced with this anima model, two types of final lesions were seen as shown in Fig. 6.1.

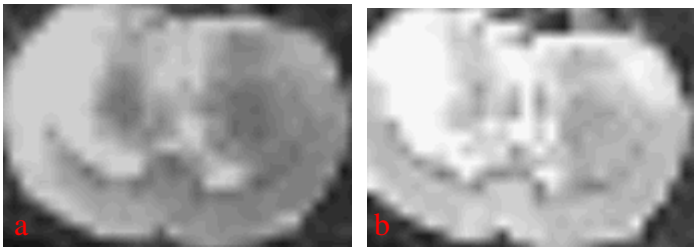

Figure 6.1: T2-weighted image showing final lesion 24 hrs after reperfusion, a: lesion both in cortex and striatum, b: lesion only in stritum.

In group A, all 8 rats developed a final lesion on T2-weighted image 24hr after reperfusion. Among the 8 rats, 4 had detectable BBB leakage with water content (1.002 ± 0.006) immediately after reperfusion, and the other 4 did not have detectable BBB leakage with water content (1.003 ± 0.005).

In group B, all 9 rats developed final lesion. Among the 9 rats, 4 rats had BBB leakage both at 1hr and 24hr after reperfusion. Two of them had decreased permeability at 24hr after reperfusion, indicating the recovery of the BBB. While 2 rats had BBB leakage only at 24hr after reperfusion, the other 3 rats did not have BBB leakage either at 1 or 24hr after reperfusion. Examples of the T2-weighted images, permeability maps, and T1-weighted images post contrast for one rat at both 1hr and 24hr after reperfusion are shown in Fig. 6.2.

Group B was divided into two subgroups: group B1 with BBB leakage and group B2 without BBB leakage. The time course of water content for the two subgroups is shown in Fig. 6.3.

In group B1, water content continued to increase with time, and there was significant water increase ($p<0.05$) as early as 2 hr after reperfusion. In group B2, water content continued to increase up to 6hr after reperfusion, however, no increase was observed after

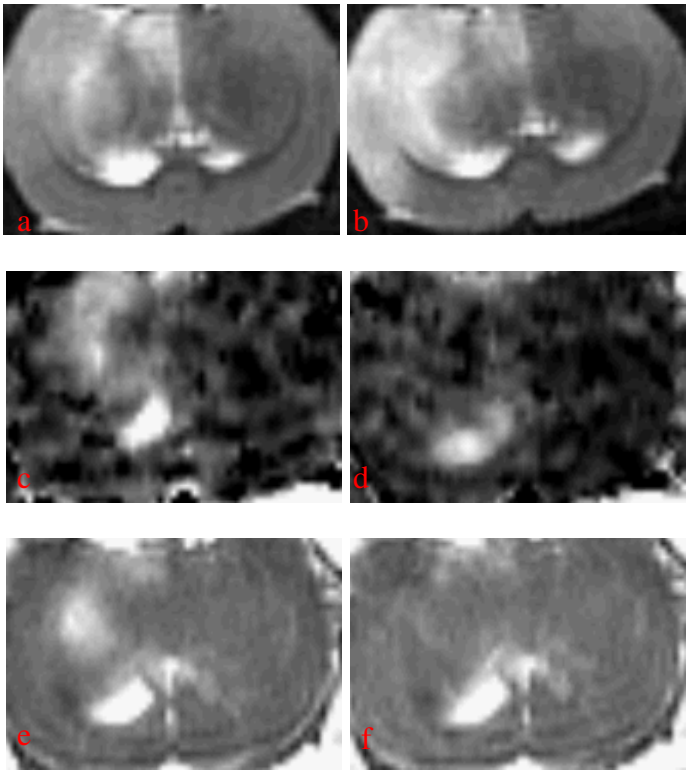

Figure 6.2: T2-weighted images, a: 1hr and b: 24 hr after reperfusion; permeability maps, c: 1hr and d: 24hr after reperfusion; T1-weighted images, e: 1hr and f: 24hr after reperfusion.

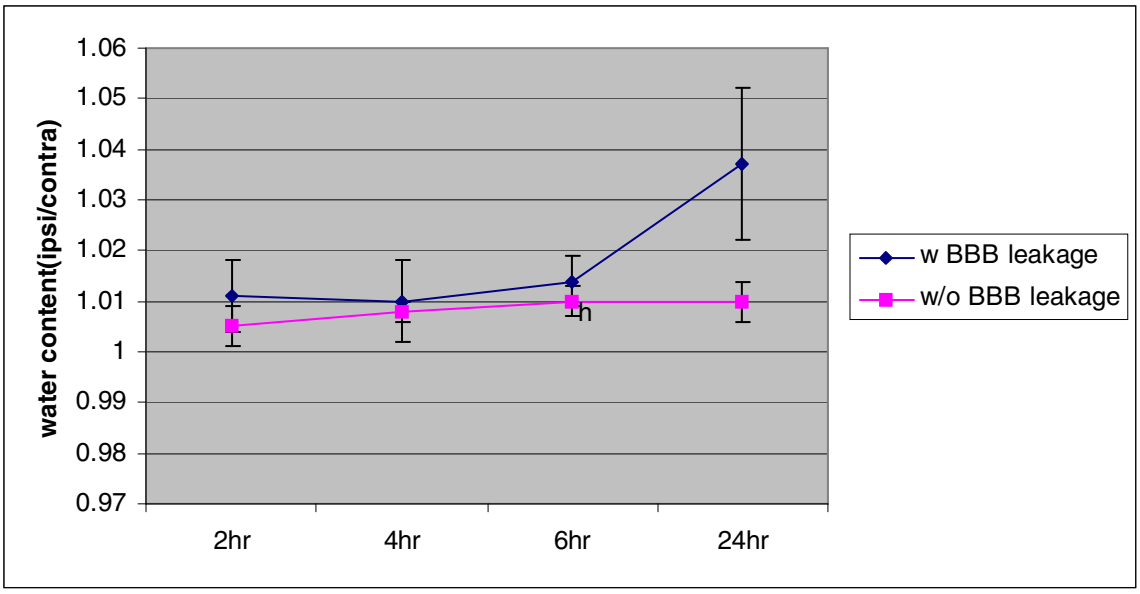

Figure 6.3: The evolution of water content for group B.

that. A significant increase ($p<0.05$) was observed 4hr after reperfusion.

There was no significant difference in water content between group B1 and B2 at 2hr, 4hr, and 6hr after reperfusion, however, there was significant difference between them at 24hr after reperfusion.

Results for Specific Aim 4

Fig. 6.4 shows the relationship between permeability and water content for group B1. The statistical test $T = \frac{R\sqrt{n-2}}{\sqrt{1-R^2}}$ has a t distribution with n-2 df. With $R^2=0.1088$, n=12, $T=1.105<T_{0.025,17}=2.2$, therefore, there is no linear relationship between the water content and permeability ($r=0.33$, $p>0.05$).

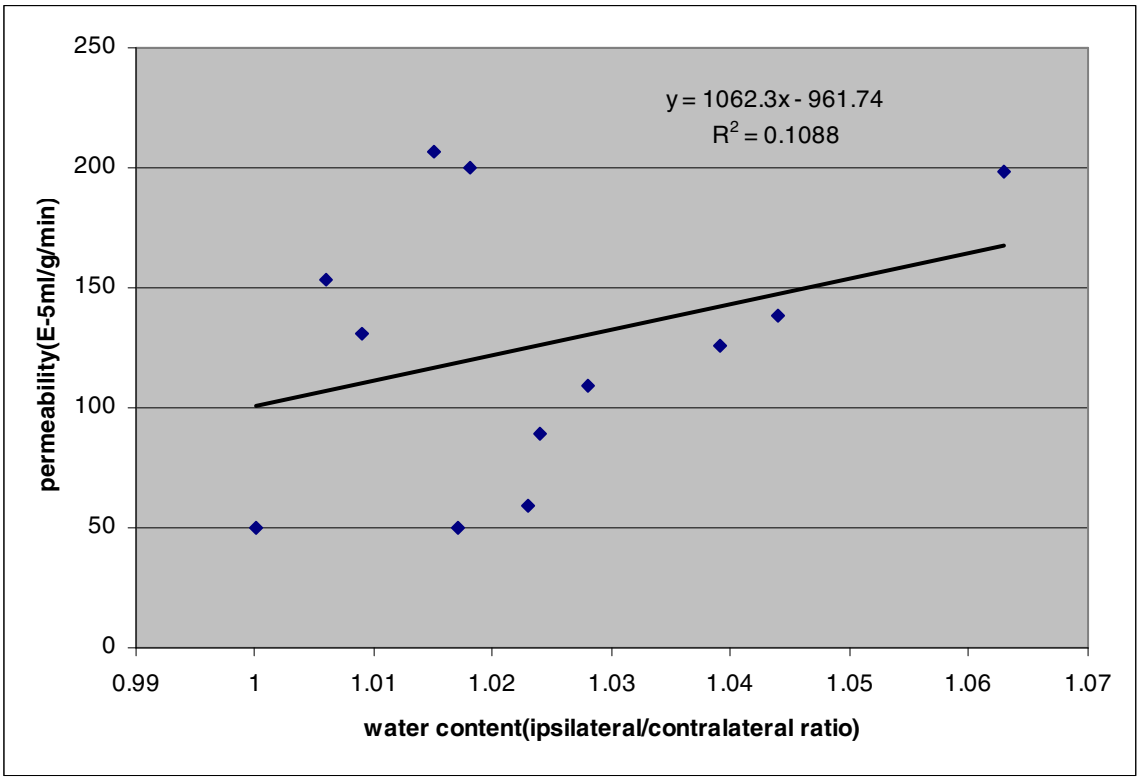

Figure 6.4: The relationship between water content and permeability for group B1.

Discussion

The time course of water content in relation to permeability was studied using the suture model.

Belayev[24] et al. reported Evans Blue (EB) extravasation first became grossly visible between 2 and 3hr after reperfusion with a suture model of 2h temporary occlusion, and was grossly unapparent at 24-26hr.

Our results showed BBB opening to Gd-DTPA was detectable as early as 1hr after reperfusion, possibly because Gd is smaller than EB. The permeability at 1hr varied from rat

to rat, probably depending on the severity of ischemia. In 2 rats, BBB showed obvious recovery at 24hr. The BBB opening at 24hr but not at 1hr indicated a delayed BBB opening. Our results agreed with Belayev's results quite well.

The first BBB opening is believed to depend on the depth and duration of ischemia, and is associated with a pronounced reactive hyperemia, which almost invariably develops after release of arterial occlusion previously subjected to severe ischemia[28, 24]. The recovery of the BBB may be due to re-establishment of normal function of the BBB after progressively subsiding hyperemia and re-establishment of autoregulation[28]. Another explanation could be inhibition of pinocytotic activity. It is possible the postischemic disturbance in energy metaboliam could temporarily inhibit pinocytotic transport, an active, energy-dependent process. Since the permeability measured in this study is essentially identical to the permeability-surface area (PS) products, the decreased permeability may also be due to the decreased surface area such as with the no reflow phenomenon.

While BBB opening showed a biphasic pattern, the water content showed a trend of increase, with $r=0.33, P>0.05$, thus proving the null hypothesis in specific aim 4 that there was no linear relationship between water content and permeability.

There was a significant water increase in group B2 from 4hr after reperfusion indicated edema could develop in the absence of detectable BBB leakage. This edema formation might be related to pressure gradients and the conductivity of the capillaries previously subjected to ischemia.

BBB leakage did not play an important role in water content increase at an early stage since there was no significant difference between group B1 and B2 up to 6hr after reperfusion. During this period, BBB broke down in group B1, but not in group B2. After 6hr,

no water increase was observed in group B2, however, water increased substantially in group B1 after 6 hr, probably due to the elevated permeability.

Our results, shown in Fig. 6.4, proved the null hypothesis in specific aim 4 that there was no linear relationship between water content and permeability. This was probably due to the different development trends of the two variables: water content and permeability.

In summary, while BBB opening followed a biphasic pattern, the water content showed a trend of increase. BBB leakage did not play an important role in water content increase at least to 6hr after reperfusion. After that, BBB opening worsened the formation of edema. While permeability recovered by 24 hr after reperfusion, water content reached its maximal value of the study period.

When comparing SHRsp and suture models, there are several differences, though both have edema and BBB breakdown.

First, the temporal resolution of the study is different. The SHRsp rats were imaged weekly starting from 12 weeks and continuing for 5 weeks. The suture models were imaged immediately, 2hr, 4hr, 6hr and 24hr after reperfusion.

Second, the disruption of the BBB is different. In SHRsp, the BBB leakage could occur either in cortex or the striatum, the weakest area for the specific rat under chronic hypertension, while BBB broke down in the territory supplied by MCA in suture model.

Third, the pattern of BBB leakage is different. In SHRsp, BBB remained open once it broke down, while the BBB recovered at 24hr after reperfusion, following a biphasic pattern, in the suture model.

Fourth, the result of BBB opening is different. In SHRsp, elevated permeability might result in hemorrhagic transformation, however, hemorrhage seldom occurred in the suture

model due to BBB leakage.

Fifth, the mechanism for BBB opening is different. In SHRsp rats, the disruption of the BBB is believed to result from high blood pressure, while BBB opening in the suture model is caused by ischemia followed by the recirculation. The recovery of the BBB in this area may be due to the recovery of the cells.

Sixth, the development pattern of edema is different. In SHRsp rats, lesion mainly developed from the cortex or the striatum. Then, via the white matter, edema spread along a pressure gradient from the lesioned gray matter to the white matter, sometimes even reaching the contralateral hemisphere via the corpus callosum, and further into the cerebrospinal fluid (CSF) spaces. In the suture model, on the other hand, edema was always at the ipsilateral side during the study period.

Seventh, the role of BBB opening on development of edema is different. In SHRsp, edema developed as vasogenic edema. BBB brerakdown played an important role in the onset of edema. Before BBB breakdown, there was no water content increase. In the suture model, BBB breakdown did not play an important role in water content increase at the early phase, up to 6 hours after reperfusion.

Eighth, the relationship between water content and permeability is different. In SHRsp rats, there was a linear relationship between water content and permeability to Gd-DTPA. Movement of water into brain tissue could have been facilitated by the increase in cerebrovascular permeability to such small molecules as Gd-DTPA. In the suture model, while BBB opening followed a biphasic pattern, the water content showed a trend of increase. There was therefore not a linear relationship between water content and permeability in the suture model. BBB leakage did not play an important role in water content increase at least to

6hr after reperfusion. But, after that, BBB opening worsened the edema formation. When permeability recovered at 24 hr after reperfusion, water content reached its maximal value of the study period.

CHAPTER 7

Conclusions and Future Directions

The main goal of this dissertation was to apply MRI to the pathologic study of stroke, specifically, to look into the relationship between water content and blood-brain barrier permeability detected by Gd-DTPA under both chronic hypertension with increased CPP and acute ischemic conditions with decreased CPP.

A theoretical model was employed for absolute measurement of rat brain water content, the Patlak Plot was utilized for permeability measurement, and CBV was measured by using a steady-state method.

The major findings using these two animal models are as follows:

Under chronic hypertension condition using a SHRsp rat model, no edema was formed before BBB breakdown to small molecules detected by Gd-DTPA, and there was a weak linear relationship between the water content increase and BBB permeability once BBB broke down; BBB broke down no later than the presence of hemorrhage, and CBV decreased under the symptoms of weight loss/enlarged ventricles. Under acute ischemic conditions, while BBB opening showed a biphasic pattern, the water content showed a trend of increase. BBB leakage did not play an important role in water content increase at least to 6hr after reperfusion. After that, BBB opening worsened the edema formation. While permeability recovered at 24 hr after reperfusion, water content reached its maximal value of the study period.

In conclusion, magnetic resonance imaging (MRI) is a powerful non-invasive imaging modality, which has been used for pathological investigation of stroke using two animal models in this dissertation. Though both increased CPP or decreased CPP can result in BBB breakdown down and edema development, the stroke development pattern is different under chronic hypertension and acute ischemic condition due to different underlying mechanisms.

Our results shed some light on the mechanism of stroke development under both chronic hypertensive conditions and acute ischemic conditions, and may be helpful for the therapy of edema. Furthermore, some future directions can be explored.

1) Use $MnCl_2$ to detect small leakage. Manganese-enhanced MRI (MEMRI) [128-143] is being increasingly used for MRI in animals due to the unique T_1 contrast that is sensitive to a number of biologic processes. MEMRI has been as a whole-brain contrast agent after systemic administration. It has been demonstrated in mice and rats that an i.p., i.v., or subcutaneous (s.c.) injection of $MnCl_2$ leads to unique MRI contrast of the brain.

2) Use MnCl2 to fMRI. Due to the fact that manganese ion (Mn^{2+}) can enter excitable cells via voltage-gated calcium channel, protocols have been devised that enable accumulation of Mn^{2+} in active areas of the brain and heart. This technique has been referred to as activation-induced MEMRI[128-143].

3) Compare different methods to measure T_1, including inversion recovery spin echo sequence, TOMROP method, and gre sequence with multiple flip angles.

4) Apply UNFOLD method[56] to fMRI to save the acquisition time.

5) Use UNFOLD method[56] to measure permeability via infusion of contrast agent to maintain the constant concentration of contrast agent.

6) Measure CBV and permeability simultaneously to correct the contrast agent leakage effect in CBV measurement.

7) Explore the relationship between MT related parameters[118-127] and BBB opening. Since we already know where the BBB opening most likely occurs, we may be able to find more applications of MT related parameters.

REFERENCES:

1. Johansson BB, Brain Edema, *Acta Neurochirurgica Suppl*. 36, 137-141,1986.

2. Cervos-Navarro J, Artigas J, and Mrsulja BJ. Morphofunctional Aspects of the ormal and Pathological Blood-Brain Barrier, *Acta Neupathol (Berl) Suppl*. VIII, 1-19, 1983.

3. Henderson E, Sykes J, Drost D, Weinmann H, Rutt BK, and Lee T, Simultaneous MRI Measurement of Blood Flow, Blood Volume, and Capillary Permeability in Mammary Tumors Using Two Different Contrast Agents, *JMRI* 12:991-1003, 2000.

4. Hoehn M, Nicola K, Franke C, and Sanden B, Application of Magnetic Resonance to animal models of cerebral ischemia, *JMRI* 14:491-509, 2001.

5. Forsting M, Reith W, Dorfler A, Meyding-Lamade U, and Sartor K, MRI Monitoring of Experimental Cerebral Ischaemia: Comparison of Two Models, *Neuroradiology* 36:264-268, 1994.

6. Siesjo BK, Pathophysiology and treatment of focal cerebral ischemia Part I: Pathophysiology, *J Neurosurg* 77:169-184, 1992.

7. Siesjo BK, Pathophysiology and treatment of focal cerebral ischemia Part II: Mechanisms of Damage and Treatment, *J Neurosurg* 77:337-354,1992.

8. Yang GY, Chen SF, Kinouchi H, Chan PH, and Weinstein PR. Edema, Cation Content, and ATPase Activity After Middle Cerebral Artery Occlusion in Rats. *Stroke* 23: 1331-1336, 1992.

9. Young W, Rappaport ZH, Chalif DJ, and Flamm ES. Regional Brain Sodium, Potassium, and Water Changes in the Rat Middle Cerebral Artery Occlusion Model of Ischemia. *Stroke* 18:751-759, 1987.

10. Hossmann KA, Sakaki S, and Zimmermann V. Cation Activities in Reversible Ischemia of the Cat Brain. *Stroke* Vol 8, No 1: 77-81, 1977.

11. Todd NV, Picozzi P, Crockard HA, and Ross Russell RW. Duration of Ischemia Influences the Development and Resolution of Ischemic Brain Edema. *Stroke* Vol.17, No 3:466-471, 1986.

12. Kuroiwa T, Cahn R, Juhler M, Goping G, Gampbell G, and Klatzo I. Role of Extracellular Proteins in the Dynamics of Vasogenic Brain Edema. *Acta Neuropathol (Berl)* 66:3-11,1985.

13. Olsson Y, Crowell RM, and Klatzo I. The Blood-Brain Barrier to Protein Tracers in Focal Cerebral Ischemia and Infarction Caused by Occlusion of the Middle Cerebral Artery. *Acta Neuropath (Berl)* 18:89-102, 1971.

14. Kogure K, Busto R, and Scheinberg P. The Role of Hydrostatic Pressure in Ischemic Brain Edema. *Ann Neurol* 9: 273-282, 1981.

15. Hatashita S and Toff JT. Role of a Hydrostatic Pressure Gradient in the Formation of Early Ischemic Brain Edema. *JCBFM* 6:546-552, 1986.

16. Hatashita S and Toff JT. Biomechanics of Brain Edema in Acute Cerebral Ischemia in Cats. *Stroke* 19:91-97, 1988.

17. Hatashita S and Toff JT. Cortical Tissue Pressure Gradients in Early Ischemic Brain Edema. *JCBFM* 6:1-7, 1986.

18. Betz AL, Keep RF, Beer ME, and Ren X. Blood-Brain Barrier Permeability and Brain Concentration of Sodium, Potassium, and Chloride During Focal Ischemia. *JCBFM* 14:29-37,1994.

19. Hatashita S and Hoff JT. Brain Edema and Cerebrovascular, Permeability During Cerebral Ischemia in Rats. *Stroke* 21:582-588,1990.

20. Gotoh O, Asano T, Koide T, and Takakura K. Ischemic Brain Edema Following Occlusion of the Middle Cerebral Artery in the Rat. I: The Time Course of the Brain Water, Sodium and Potassium Contents and Blood-Brain Barrier Permeability to ^{125}I-Albumin.*Stroke* 16-1: 101-109,1985.

21. Sampaolo S, Nakagawa Y, Iannotti F, Cervos-Navarro J, and Bonavita V. Blood-Brain Barrier Permability to Micromoleculars and Edema Formation in the Early Phase of Incomplete Continuous Ischemia. *Acta Neuropathol* 82: 107-111,1991.

22. Hatashita S, and Hoff JT. Role of Blood-Brain Barrier Permeability in Focal Ischemic Brain Edema. *Advances in Neurology* 52:327-333,1990.

23. Yang G, Betz AL, Chenevert TL, Brunberg JA, and Hoff JT. Experimental intracerebral Hemorrhage: Relationship between Brain Edema, Blood Flow, and Blood-Brain Barrier Permeability in Rats. *J Neurosurg* 81:93-102,1994.

24. Belayev L, Busto R, Zhao W, and Ginsberg MD. Quantitative Evaluation of Blood-Brain Barrier Permeability following Middle Cerebral Artery Occlusion in Rats. *Brain Res* 739:88-96,1996.

25. Baskaya MK, Rao AM, Dogan A, Donaldson D, and Dempsey RJ. The Biphasic Opening of the Blood-Brain Barrier in the Cortex and Hippocampus after Traumatic Brain Injury in Rats. *Neurosci Letters* 226: 33-36, 1997.

26. Gartshore G, Patterson J, and Macrae IM. Influence of Ischmia and Reperfusion on the Course of Brain Tissue Swelling and Blood-Brain Barrier Permeability in a Rodent Model of Transient Focal Cerebral Ischemia. *Experi Neurology* 147:353-360,1997.

27. Neumann-Haefelin T, Kastrup A, de Crespigny A, Yenari MA, Ringer T, Sun GH, and Mosley ME. Serial MRI After Transient Focal Cerebral Ischemia in Rats: dynamics of tissue injury, BBB damage, and edema formation. *Stroke* 31:1965-1973, 2000.

28. Kuroiwa T, Ting P, Martinez H, and Klatzo I. The Biphasic Opening of the Blood-Brain Barrier to Proteins following Temporary Middle Cerebral Artery Occlusion. *Acta Neuropathol (Berl)* 68:122-129, 1985.

29. Sage JI, Van Uttert RL, and Duffy TE. Early Changes in Blood Brain Barrier Permeability to Small Molecules after Transient Cerebral Ischemia. *Stroke* Vol 15, No1: 46-50,1983.

30. Preston E, Sutherland G, and Finsten A. Three Openings of the Blood-Brain Barrier Produced by Forebrain Ischemia in the rat. *Neuroscience letters* 149:75-78, 1993.

31. Juhler M, Barry DI, Offner H, Konat G, Klinken L, and Paulson OB. Blood-Brain and Blood-Spinal Cord Barrier Permeability During the Course of Experimental Allergic Encephalomyelitis in the Rat. *Brain Res* 302:347-355,1984.

32. Shigeno T, Teasdale GM, McCulloch J, and Graham DI. Recirculation Model following MCA Occlusion in Rats: Cerebral Blood Flow, Cerebrovascular Permeability, and Brain Edema. *J Neurosurg* 63:272-277,1985.

33. Yang G, and Betz AL. Reperfusion-Induced Injury to the Blood-Brain Barrier after Middle Cerebral Artery Occlusion in Rats. *Stroke* 25:1658-1665,1994.

34. Todd NV, Picozzi P, Crockard HA, and Ross Russell R. Reperfusion After Cerebral Ischemia: Influence of Duration of Ischemia. *Stroke* Vol. 17, No3: 460-465, 1986.

35. Memezawa H, Smith M, and Siesjo BK. Penumbral Tissues Salvaged by Reperfusion Following Middle Cerebral Artery Occlusion in Rats. *Stroke* 23:552-559,1992.

36. Westergaard E, Go G, Klatzo I, and Spatz M. Increased Permeability of Cerebral Vessels to Horseradish Peroxidase Induced by Ischemia in Mongolian Gerbils. *Acta Neuropath (Berl.)* 35:307-325, 1976.

37. Belayev L, Alonso OF, Busto R, Zhao W, and Ginsberg MD. Middle Cerebral Artery Occlusion in the Rat by Intraluminal Suture: Neurological and Pathological Evaluation of An Improved Model. *Stroke* 27:1616-1623, 1996.

38. Oliff HS, Weber E, Eilon G, and Marek P. The Role of Strain/Vendor Differences on the Outcome of Focal Ischemia Induced by Intraluminal Middle Cerebral Artery Occlusion in the Rat. *Brain Res*. 675: 20-26, 1995.

39. Matsuo Y, Onodera H, Shiga Y, Shozuhara H, Ninomiya M, Kihara T, Tamatani T, Miyasaka M, and Kogure K. Role of Cell Adhesion Molecules in Brain Injury After Transient Middle Cerebral Artery Occlusion in the Rat. *Brain Res*. 656:344-352,1994.

40. Belayev L, Busto R, Zhao W, and Ginsberg MD. HU-211, a Novel Noncompetitive N-Methyl-D-Aspartate Antagonist, Improves Neurological Deficit and Reduces Infarct Volume after Reversible Focal Cerebral Ischemia in the Rat. *Stroke* 26:2313-2320,1995.

41. Longa EZ, Weinstein PR, Carlson S, and Cummins R. Reversible Middle Cerebral Artery Occlusion Without Craniectomy in Rats. *Stroke* 20:84-91, 1989.

42. Nagasawa H, and Kogure K. Correlation Between Cerebral Blood Flow and Histologic Changes in a New Rat Model of Middle Cerebral Artery Occlusion. *Stroke* 20:1037-1043, 1989.

43. Lin W, Paczynski RP, Venkatesan R, He YY, Powers WJ, Hsu CY, and Haacke EM. Quantitative Regional Brain Water Measurement with Magnetic Resonance Imaging in a Focal Ischemia Model. *MRM* 38:303-310,1997.

44. Venkatesan R, Lin W, Gurleyik K, He YY, Paczynski RP, Powers WJ, and Hsu CY. Absoluhte Measurements of Water Content using Magnetic Resonance Imaging: Preliminary Findings in an In Vivo Focal Ischemia Rat Model. *MRM* 43:146-150,2000.

45. Venkatesan R, Lin W, and Haacke EM. Accurate Determination of Spin-Density and T1 in the Presence of RF-field Inhomogeneities and Flip-Angle Miscalibration. *MRM* 40:592-602,1998.

46. Lin W, Venkatesan R, Kilichan G, He YY, Powers WJ, and Hsu CY. An Absolute Measurement of Brain Water Content Using Magnetic Resonance Imaging in Two Focal Cerebral Ischemic Rat Models. *JCBFM* 20(1): 37-44, 2000.

47. Kenney J, Schmiedl U, Maravilla K, Starr F, Graham M, Spence A, and Nelson J. Measurement of Blood-Brain Barrier Permeability in a Tumor Model using Magnetic Resonance Imaging with Gadolinium-DTPA. *MRM* 27:68-75, 1992.

48. Ewing JR, Knight RA, Nagaraja TN, Yee JS, Nagesh V, Whitton PA, Li L, and Fenstermacher JD. Patlak Plots of Gd-DTPA MRI Data Yield Blood-Brain Transfer Constants Concordant with Those of ^{14}C-Sucrose in Areas of Blood-Brain Opening. *MRM* 50:2003.

49. Patlak CS, Blasberg RG, and Fenstermacher JD. Graphical Evaluation of Blood-to-Brian Transfer Constants from Multiple-Time Uptake Data. *JCBFM* 3:1-7, 1983.

50. Tofts PS, and Berkowitz BA. Measurrement of Capillary Permeability From the Gd Enhancement Curve: A Comparison of Bolus and Constant Infusion Injection Methods. *MRI* 12:81-91, 1994.

51. Tofts PS, and Kermode AG. Measurement of the Blood-Brain Barrier Permeability and Leakage Space Using Dynamic MR Imaging. 1. Fundamental Concepts. *MRM* 17:357-367,1991.

52. Dobbin J, Crockard HA, and Ross-Russell R. Transient Blood-Brain Barrier Permeability following Profound Temporary Global Ischaemia: An Experimental stydy Using ^{14}C-AIB. *JCBFM* 9:71-78,1989.

53. Cao Y, Brown SL, Knight RA, Fenstermacher JD, and Ewing JR. Effect of Intravascular-to-Extravascular Water Exchange on the Determination of Blood-to-Tissue Transfer Constant by Magnetic Resonance Imaging. *MRM* 53:282-293,2005.

54. Landis CS, Lin X, Telang FW, Molina PE, Palyka I, Vetek G, and Springer CS. Equilibrium Transcytolemmal Water-Exchange Kinetics in Skeletal Muscle In Vivo. *MRM* 42:467-478,1999.

55. Hazlewood CF, Chang DC, Nichols BL, and Woessner DE. Nuclear Magnetic Resonance Transverse Relaxation Times of Water Protons in Skeletal Muscle. *Biophysical J* 14:583-606,1974.

56. Madore B, Glover HG, and Pelc NJ. Unaliasing by Fourier-Encoding the Overlaps Using the Temporal Dimension (UNFOLD), Applied to Cardiac Imaging and fMRI. *MRM* 42:813-828,1999.

57. Brix G, Schad LR, Deimling M, and Lorenz WJ. Fast and Precise T1 imaging using a TOMROP Sequence. *MRI* 8:351-356, 1990.

58. Ueno H, Hara T, Ishi A, and Shuto K. Effects of Benidipine Hydrochloride on Cerebrovascular Lesions in Salt-Loaded Stroke-Prone Spontaneously Hypertensive Rats: Evaluation by Magnetic Resonance Imaging. *Jpn. J. Pharmacol*. 84: 56-62, 2000.

59. Kalimo H, Fredriksson K, Nordborg C, Auer RN, Olsson Y, and Johansson B. The Spread of Brain Edema in Hypertensive Brain Injury. *Medic Biolo* 64:133-137, 1986.

60. Fredriksson K, Kalimo H, Westergren I, Kahrstrom J, and Johansson BB. Blood-Brain Barrier Leakage and Brain Edema in Stroke-prone Spontaneously Hypertensive Rats: Effect of Chronic Sympathectomy and Low Protein/High Salt Diet. *Acta Neuropathol (Berl)* 74:259-268, 1987.

61. Blezer EL, Schurink M, Nicolay K, Bar PD, Jansen GH, Koomans HA, and Joles JA. Proteinuria Precedes Cerebral Edema in Stroke-Prone Rats A Magnetic Resonance Imaging Study. *Stroke* 29:167-174, 1998.

62. Sironi L, Guerrini U, Tremoli E, Miller I, Gelosa P, Lascialfari A, Zucca I, Eberini I, Gemeiner M, Paoletti R, and Gianazza E. Analysis of Pathological Events at the Onset of

Brain Damage in Stroke-Prone Rats: A Proteomics and Magnetic Resonance Imaging Approach. *J Neurosci Res* 78:115-122, 2004.

63. Blezer EL, Nicolay K, Viergever MA, Koomans HA, and Joles JA. MRI-Based Quantification of Cerebral Edema in Individual SHRSP Rats Using Averaged Criteria Determined Before the Occurrence of Edema. *MRI* Vol.17, No.6: 903-907, 1999.

64. Okamoto K, yamori Y, and Nagaoka A. Establishment of the Stroke-prone Spontaneously Hypertensive Rat (SHR). *Circ. Res*. 35:1143-1153; 1974.

65. Sironi L, Tremoli E, Miller I, Guerrini U, Calvio AM, Eberini I, Gemeiner M, Asdente M, Paoletti R, and Gianazza E. Acute-Phase Proteins Before Cerebral Ischemia in Stroke-Prone Rats identification by proteomics. *Stroke* 32:753-760,2001.

66. Guerrini U, Sironi L, Tremoli E, Cimino M, Pollo B, Calvio AM, Paoletti R, and Asdente M. New Insights into Brain Damage in Stroke-Prone Rats: A Nuclear Magnetic Imaging Study. *Stroke* 33:825-830, 2002.

67. Fredriksson K, Auer RN, Kalimo H, Nordborg C, Olsson Y, and Johansson BB. Cerebrovascular Lesions in Stroke-prone Spontaneously Hypertensive Rats. *Acta Neuropathol (Berl)* 68:284-294,1985.

68. Fredriksson K, Kalimo H, Nordborg C, Olsson Y, and Johansson BB. Cyst Formation and Glial Response in the Brain Lesions of Stroke-prone Spontaneously Hypertensive Rats. *Acta Neuropathol* 76:441-450, 1988.

69. Fredriksson K, Kalimo H, Nordborg C, Johansson BB, and Olsson Y. Nerve Cell Injury in the Brain of Stroke-prone Spontaneously Hypertensive Rats. *Acta Neuropathol* 76:227-237, 1988.

70. Tagami M, Kubota A, Sunaga T, Fujino H, Maezawa H, Kihara M, Nara Y, and Yamori Y. Permeability of Intracranial Extracerebral Vessels in Stroke-Prone SHR. *Stroke* Vol 12, No 6:852-857, 1981.

71. Horie R, Yamori Y, and Handa H. An Essentail Difference between Stroke-prone SHR (SHRSP) and Stroke-resistant SHR (SHRSR): Quantitative Evidence Obtained by Yamori's Preparation II. *Jap. Heart J* Vol. 19 No. 4:630-632, 1978.

72. Akiguchi I, Horie R, Ohtaka M, Ooshima A, and Yamori Y. Typical Course of Stroke in SHRSP. *Jap. Heart J* July: 615-616,1978.

73. Yamori Y, Horie R, Handa H, Sato M, and Okamoto K. Studies on Stroke in Stroke-Prone Spontaneously Hypertensive Rats (SHRSP) (I) Local Factor Analysis on Stroke. *Jap. Heart J* Vol.16 No.3: 329-331, 1975.

74. Yamori Y, Horie R, Otsubo K, Handa H, Sato M, and Okamoto K. Studies on Stroke in Stroke-Prone Spontaneously Hypertensive Rats (SHRSP) (II) Cerebrovascular Fat Deposition and Cerebrovascular Permeability. *Jap. Heart J* Vol.16 No.3: 332-335, 1975.

75. Yamori Y, Fujikawa J, Akiguchi I, Nara Y, and Ikeda K. Effect of Acute Arterial Hypertension in Stroke-prone and Stroke-resistant SHR. *Jap. Heart J* Vol.19 No.4: 606-608, 1978.

76. Shima K, Ohashi K, Umezawa H, Chigasaki H, and Okuyama S. Blood-Brain Barrier, Cerebral Blood Flow, and Brain Edema in Spontaneously Hypertensive Rats with Chronic Focal Ischemia. *Acta Neurochir (suppl)* 60:271-273, 1994.

77. Horie R. Cerebral Circulation and the Initiation Mechanism of Stroke in Stroke-prone Spontaneously Hypertensive Rats (SHRSP). *Jap. Circulation J* Vol.41: 915-935, 1977.

78. Takahashi S, Hamai Y, and Okamoto K. On the Findings of Stroke-prone SHR. *Jap. Heart J.* July: 645, 1978.

79. Yoshida M, Horie R, Akiguchi I, Ohta K, Yoshida H, Amemiya T, and Yamori Y. Relationship between Arterial Lesions of the Retina and the Brain in Stroke-prone SHR (SHRSP). *Jap. Heart J* Julu: 612-614, 1978.

80. Yamori Y, Fujikawa J, Ohtaka M, Horie R, and Akiguchi I. Cerebral Stroke and Myocardial Lesions in Stroke-prone SHR. *Jap. Heart J* Vol.19 No.4: 609-611, 1978.

81. Horie R, Yamori Y, Akiguchi I, Ohtaka M, and Nara Y. Significance of Cerebral Blood Flow in the Mechanism of Stroke in Stroke-prone Spontaneously Hypertensive Rats (SHRSP). *Jap. Heart J* Vol.19 No.4: 601-603, 1978.

82. Yamori Y, Nara Y, Horie R, Ohtaka M, Ohta K, and Mitani F. Biomembrane C haracteristics in Stroke-prone Spontaneously Hypertensive Rats (SHRSP). *Jap. Heart J* July: 597-598, 1978.

83. Smeda JS, VanVliet BN, and King SR. Stroke-prone Spontaneously Hypertensive Rats Lose Their Ability to Auto-Regulate cerebral Blood Flow Prior to Stroke. *J Hypertension* 17:1697-1705,1999.

84. Fredriksson K, Ingvar M, and Johansson BB.Regional Cerebral Blood Flow in Conscious Stroke-Prone Spontaneously Hypertensive Rats. *JCBFM* 4:103-106,1984.

85. Hajdu MA, and Baumbach GL. Mechanics of Large and Small Cerebral Arteries in Chronic Hypertension. *The American Physiological Society* H1027-1033, 1994.

86. Coyle P, and Heistad DD. Blood Flow Through Cerebral Collateral Vessels One Month After Middle Cerebral Artery Occlusion. *Stroke* 18:407-411, 1987.

87. Coyle P, Odenheimer DJ, and Sing CF. Cerebral Infarction After Middle Cerebral Artery Occlusion in Progenies of Spontaneously Stroke-Prone and Normal Rats. *Stroke* Vol 15, No 4:711-716, 1984.

88. Ueno M, Sakamoto H, Tomimoto H, Akiguchi I, Onodera M, Huang C, and Kanenishi K. Blood-Brain Barrier is Impaired in the Hippocampus of Young Adult Spontaneously Hypertensive Rats. *Acta Neuropathol* 107:532-538,2004.

89. Ueno M, Sakamoto H, Liao Y, Onodera M, Huang C, Miyanaka H, and Nakagawa T. Blood-Brain Barrier Disruption in the Hypothalamus of Young Spontaneously Hypertensive Rats. *Histochem Cell Biol* 122:131-137, 2004.

90. Ueno K, Togashi H, Mori K, Matsumoto M, Ohashi S, Hoshino A, Fujita T, Saito H, Minami M, and Yoshioka M. Behavioural and Pharmacological Relevance of Stroke-prone Spontaneously Hypertensive Rats as an Animal Model of a Developmental Disorder. *Behavioural Pharmacology* 13:1-13, 2002.

91. Negishi H, Ikeda K, Nara Y, and Yamori Y. Increased Hydroxyl Radicals in the Hippocampus of Stroke-prone Spontaneously Hypertensive Rats During Transient Ischemia and Recirculation. *Neuroscience Letters* 306:206-208,2001.

92. Lin J, Tomimoto H, Akiguchi I, Wakita H, Shibasaki H, and Horie R. White Matter Lesions and Alteration of Vascular Cell Composition in the Brain of Spontaneously Hypertensive Rats. *Neurophysiology, Basic and Clinical.Vol.*12 No.9: 1835-1839,2001.

93. Abraham CS, Harada N, Deli MA, and Niwa M. Transient Forebrain Ischemia Increases the Blood-Brain Barrier Permeability for Albumin in Stroke-Prone Spontaneously Hypertensive Rats. *Cellular and Molecular Neurobiology* Vol.22 No.4: 455-462, 2002.

94. Nagao T, Sadoshima S, Ishitsuka T, Kusuda K, Shiokawa O, Ibayashi S, and Fujishima M. Effects of Acute Superior Cervical Ganglionectomy on Cerebral Blood Flow and Metabolism in Stroke-Prone Spontaneously Hypertensive Rats Subjected to Cerebral Ischsemia. *Clinical and Experimental Pharmacology and Physiology* 19:489-493,1992.

95. Taguchi H, Faraci FM, Kitazono T, and Heistad DD. Relaxation of the Aorta During Hypoxia Is Impaired in Chronically Hypertensive Rats. *Hypertension* 25[part2]: 735-738,1995.

96. Kita H, Shima K, Tatsumi M, and Chigasaki H. Cerebral Blood Flow and Glucose Metabolism of the Ischemic Rim in Spontaneously Hypertensive Stroke-Prone Rats with Occlusion of the Middle Cerebral Artery. *JCBFM* 15:235-241,1995.

97. Yabuuchi F, Takahashi M, Aritake K, Fujimoto M, Ito H, Tsuzaki M, Akai T, Yamaguchi M, Hayashi S, Nishino Y, and Brautigam M. Post-Stroke Treatment with Imidapril Reduces Learning Deficits with Less Formation of Brain Oedema in a

Stroke-Prone Substrain of Spontaneously Hypertensive Rats. *Fundam. Clin. Pharmacol*. 13: 475-483, 1999.

98. Sobey CG, Heistad DD, and Faraci FM. Effect of Subarachnoid Hemorrhage on Cerebral Vasodilatation in Response to Activation of ATP-Sensitive K^+ Channels In Chronically Hypertensive Rats. *Stroke* 28:392-397,1997.

99. Absher PM, Hendley E, Jaworski DM, Taatjes DJ, and Sobel BE. Impairment of the Blood-Brain Barrier: A Potential Surrogate Delineating the Determinants of Cerebral Bleeding Caused by Fibrinolytic Drugs. *Coronary Artery Disease* 10:413-420,1999.

100. Parkes LM and Tofts PS. Improved Accuracy of Human Cerebral Blood Perfusion Measurements Using Arterial Spin Labeling: Accounting for Capillary Water Permeability. *MRM* 48: 27-41, 2002.

101. Alsop DC and Detre JA. Multisection Cerebral Blood Flow MR Imaging with Continuous Arterial Spin Labeling. *Radiology* 208:410-416, 1998.

102. Kandel ER, Schwartz JH, and Jessell TM. *Principles of Neural Science*, 2000.

103. Kety SS, King BD, Horvath SM, Jeffers WS, and Hafkenschiel JH. The Effects of an Acute Reduction in Blood Pressure by Means of Differential Spinal Sympathetic Block on the Cerebral Circulation of Hypertensive Patients. *J Clin Invest*, Apr; 29 (4): 402-407, 1950.

104. Kety SS. Circulation and Metabolism of The Human Brain in Health and Disease. *Am J Med*. Feb; 8 (2): 205-217, 1950.

105. Boysen G. Cerebral Hemodynamics in Carotid Surgery. *Acta Neurol Scand Suppl*. 52: 3-86, 1973.

106. Baron JC, Bousser MG, Rey A, Guillard A, Gmar D, and Castaigne P. Reversal of Focal "Misery-Perfusion Syndrom' by Extra-intracranial Arterial Bypass in Hemodynamic Cerebral Ischemia. A Case Study with 15O Positron Emission Tomography. *Stroke*. Jul-Aug; 12 (4) 454-459, 1981.

107. Ostergaard L, Weisskoff RM, Chesler DA, Gyldensted C, and Rosen BR. High Resolution Measurement of Cerebral Blood Flow Using Intravascular Tracer Bolus Passages. Part I: Mathematical Approach and Statistical Analysis. *MRM* Nov; 36 (5) 715-725, 1996.

108. Ostergaard L, Sorensen AG, Kwong KK, Weisskoff RM, Gyldensted C, and Rosen BR. High Resolution Measurement of Cerebral Blood Flow Using Intravascular Tracer Bolus Passages. Part II: Experimental Comparison and Preliminary Results. *MRM* Nov; 36 (5) 726-736, 1996.

109. Melgar MA, Rafols J, Gloss D, and Diaz FG. Postischemic Reperfusion: Ultrastructural Blood-Brain Barrier and Hemodynamic Correlative Changes in an Awake Model of Transient Forebrain Ischemia. *Neurosurgery* Mar; 56 (3) 571-581, 2005.

110. Guyton AC, and Hall JE. *Medical Physiology*, 2000.

111. Rapoport SI. A Mathematical Model for Vasogenic Brain Edema. *J Theor Biol* 74: 439-467, 1978.

112. Kimelberg HK. Water Homeostasis in the Brain: Basic Concepts. *Neuroscience* 129: 851-860, 2004.

113. Lin WL, Celik A, and Paczynski RP. Regional Cerebral Blood Volume: A Comparison of the Dynamic Imaging and the Steady State Methods. *JMRI* 9: 44-52, 1999.

114. Ginsberg MD and Busto R. Rodent Models of Cerebral Ischemmia. Stroke 20:1627-1642, 1989.

115. Garcia JH. Experimental Ischemic Stroke: A Review. Stroke 15:5-14, 1984.

116. Molinari GF. Why Model Strokes? Stroke 19:1195-1197, 1988.

117. Bhardwaj A, Alkayed NJ, Kirsch JR, and Hurn PD. Mechanisms of Ischemic Brain Damage. Stroke 5:160-167, 2003.

118. Knight RA, Nagesh V, Nagaraja TN, Ewing JR, Whitton PA, Bershad E, Fagan SC, and Fenstermacher JD. Acute Blood-Brain Barrier Opening in Experimentally Induced Focal Cerebral Ischemia Is Preferentially Identified by Quantitative Magnetization Transfer Imaging. MRM 54:822-832, 2005.

119. Henkelman RM, Huang X, Xiang Q, Stanisz GJ, Swanson SD, and Bronskill MJ. Quantitative Interpretation of Magnetization Transfer. MRM 29:759-766, 1993.

120. Eng J, Ceckler TL, and Balaban RS. Quantitative ^{1}H Magnetization Transfer Imaging in Vivo. MRM 17:304-314, 1991.

121. Ewing JR, Jiang Q, Boska M, Zhang ZG, Brown SL, Li GH, Divine GW, and Chopp M. T_1 and Magnetization Transfer at 7 Tesla in Acute Ischemic Infarct in the Rat. MRM 41:696-705, 1999.

122. Koenig SH, and Brown III RD. A Molecular Theory of Relaxation and Magnetization Transfer: Application to Cross-Linked BSA, a Model for Tissue. MRM 30:685-695, 1993.

123. Koenig SH, Brown III RD, and Ugolini R. Magnetization Transfer in Cross-Linked Bovine Serum Albumin Solutions at 200 MHz: A Model for Tissue. MRM 29:311-316, 1993.

124. Wolff SD, and Balaban RS. Magnetization Transfer Contrast (MTC) and Tissue Water Proton Relaxation in Vivo. MRM 10:135-144, 1989.

125. Caines GH, Schleich T, and Rydzewski JM. Incorporation of Magnetization Transfer into the Formalism for Rotaing-Frame Spin-Lattice Proton NMR Relaxation in the Presence of an Off-Resonance-Irradiation Field. MRM 95:558-566, 1991.

126. Grad J and Bryant RG. Nuclear Magnetic Cross-Relaxation Spectroscopy. JMR 90:1-8, 1990.

127. Wu X. Lineshape of Magnetization Transfer via Cross Relaxation. JMR 94:186-190, 1991.

128. Kuo Y, Herlihy AH, So P, Bhakoo KK, Bell JD. In Vivo Measurements of T1 Relaxation Times in Mouse Brain Associated with Different Modes of Systemic Administration of Magnese Chloride. JMRI 21:334-339, 2005.

129. Nordhoy W, Anthonsen HW, Bruvold M, Brurok H, Skarra S, Krane J, Jynge P. Intracellular Magnese Ions Provide strong T1 Relaxation in Rat Myocardium. MRM 52:506-514, 2004.

130. Natt O, Watanabe T, Boretius S, Radulovic J, Frahm J, Michaelis T. High-Resolution 3D MRI of Mouse Brain Reveals Small Cerebral Structures.In Vivo. J Neurosc Method 120:203-209,2002.

131. Aoki I, Lin Wu Y, Silva AC, Lynch RM, Koretsky AP.In Vivo Detection of Neuroarchitecture in the Rodent Brain Using Manganese-Enhanced MRI. Neuroimage 22:1046-1059, 2004.

132. Aoki I, Ebisu T, Tanaka C, Katsuta K, Fujikawa A, Umeda M, Fukunaga M, Takegami T, Shapiro EM, Narusse S. Detection of the Anoxic Depolarization of Focal Ischemia using Manganese-Enhanced MRI. MRM 50(1):7-12, 2003.

133. Hu TC, Christian TF, Aletras AH, Taylor JL, Koretsky AP, Arai AE. Manganese-Enhanced Magnetic Resonance Imaging of Normal and Ischemic Canine Heart. MRM 54:196-200, 2005.

134. Eriksson R, Johansson L, Bjerner T, Saebo K, Ahlstrom H. Uptake of MnCl2 and Mangafodipir Trisodium in the Myocardium: A Magnetic Resonance Imaging Study in Pigs. JMRI 19:564-569, 2004.

135. Lin Y**,** Koretsky AP. Manganese Ion Enhances T1-weighted MRI during Brain Activation: An Approach to Direct Imaging of Brain Function. MRM 38:378-388, 1997.

136. Aoki I, Tanaka C, Takegami T, Ebisu T, Umeda M, Fukunaga M, Fukuda K, Silva AC, Koretsky AP, Naruse S. Dynamic Activity-Induced Manganese- Dependent Contrast Magnetic Resonance Imaging (DAIM MRI). MRM 48:927-933, 2002.

137. Morita H, Ogino T, Seo Y, Fujiki N, Tanaka K, Takamata A, Nakamura S, Murakami M. Detection of Hypothalamic Activation by Manganese Ion Contrasted T1-weighted Magnetic Resonance Imaging in Rats. Neuroscience Letters 326:101-104, 2002.

138. Watanabe T, Michaelis T, Frahm J. Mapping of Retinal Projections in the Living Rat Using High-Resolution 3D Gradient-Echo MRI with Mn^{2+}-Induced Contrast. MRM 46:424-429, 2001.

139. Allegrini PR, Wiessner C. Three-Dimensonal MRI of Cerebral Projections in Rat Brain In Vivo After Intracortical Injection of MnCl2. NMR in Biomed 16:252-256, 2003.

140. Watanabe T, Natt O, Boretius S, Frahm J, Michaelis T. In Vivo 3D MRI Staining of Mouse Brain After Subcutaneous Application of $MnCl_2$. MRM 48:852-859, 2002.

141. Pautler RG, Silva AC, Koretsky AP. In Vivo Neuronal Tract Tracing Using Manganese-Enhanced Magnetic Resonance Imaging. MRM 40: 740-748,1998.

142. Aoki I, Naruse S, Tanaka C. Manganese-Enhanced Magnetic Resonance Imaging (MEMRI) of Brain Activity and Applications to Early Detection of Brain Ischemia. NMR in Biomed 17:569-580, 2004.

143. Lee J, Silva Ac, Merkle H, Koretsky AP. Manganese-Enhanced Magnetic Resonance Imaging of Mouse Brain after Systemic Administration of $MnCL_2$: Dose-Dependent and Temporal Evolution of T1 Contrast. MRM 53: 640-648, 2005.

144. AC. McLaughlin and JS Leigh, Jr. Relaxation times in systems with chemical exchange: approximate solution for the nondiluted case. J. Magn. Reson., 9:296-304, 1973.

145. CF Hazlewood, DC Chang, BL Nichols, and DE Woessner. Nuclear magnetic resonance transverse relaxation times of water protons in skeletal muscle. Biophysical J., 14:583-606, 1974.

146. Yamori Y, Nagaoka A and Okamoto K: Pathogenetic similarity of strokes in stroke-prone spontaneously hypertensive rats and human. Stroke7: 46-53, 1976.

147. Yamori Y, Nagaoka A and Okamoto K: Importance of genetic factors in hypertensive cerebrovascular lesion; An evidence obtained by successive selective breeding of stroke-prone and resistant SHR. Cir J 38:1095-1100, 1974.

148. Ogata J, Fujishima M, Tamaki Y, Nakatomi T, Ishitsuka T, Omae T. Vascular changes underlying cerebral lesions in stroke-prone spontaneously hypertensive rats. Acta Neuropathol (Berl). 54:183-188, 1981.

149. Volpe M, Iaccarino G, Vecchione C, Rizzoli D, Russo R, Rubattu S, Condorelli G, Ganten U, Ganten D, Trimarco B, Lindpaintner K. Association and cosegregation of stroke with impaired endothelium-Dependent vasorelaxation in stroke prone, spontaneously hypertensive Rats. J Clin Invest. 98:256-261, 1996.

150. Nagaoka A, Iwatsuka H, Suzuoki Z, Okamoto K. Genetic predisposition to Stroke in spontaneously hypertensive rats. Am J Physiol. 230: 1354-1359, 1976.

151. Gratton JA, Sauter A, Rudin M, Lees KR, McColl J, Reid JL, Dominiczak AF, Macrae IM. Susceptibility to cerebral infarction in stroke-prone spontaneously hypertensive rats is inherited as a dominant trait. Stroke 29:690-694, 1998.

152. Tamaki K, Sadoshima S, Baumbach GL, Iadecola C, Reis DJ, Heistad DD. Evidence that disruption of the blood-brain barrier precedes reduction in cerebral blood flow in hypertensive encephalopathy. Hypertension 6: 175-181; 1984.

153. Bradley WG, Waluvh V, Yadley RA, Wycoff RR. Comparison of CT and MRI in 400 patients with suspected disease of the brain and cervical spinal Cord. Radiology 152: 695-702, 1979.

154. Kertesz A, Blank SE, Nicolson L. The sensitivity and specificity of MRI in Stroke. Neurology 37: 1580-1585, 1987.

155. Brant-Wadzki M, Weinstein P, Bartkowski H, Moseley M. MR imaging and Spectroscopy in clinical and experimental cerebral ischemia: a review. AJNR Am J Neuroradiol. 148: 579-588, 1987.

156. McNamara MT, Brant-Wadzki M, Berry I, Pereria B, Weinstein P, Penguin N. Acute experimental cerebral ischemia: MR emhancement using Gd-DTPA. Radiology. 158:701-705, 1986.

157. Chien D, Kwong KK, Gress DR, Buonanno FS, Rosen BR. MR diffusion Imaging of cerebral infarction in humans. AJNR Am J Neuroradiol.13: 1097-1102, 1992.

158. Fredriksson K, Nordborg C, Kalimo H, Olsson Y, Johansson BB. Cerebral Microangiopathy in stroke-prone spontaneously hypertensive rats: an Immunohistochemical and ultrastructural study. Acta Neuropathol (Berl) 75:259-268, 1988.

159. Haacke EM, Brown RW, Thompson MR, Venkatesan R. Magnetic Resonance Imaging physical principles and sequence design, 1999.

160. Knight RA, Nagaraja TN, Ewing JR, Whitton PA, Keenan KA, Fagan SC, Fenstrmacher. MRI assessment of the blood-to-brain transfer constant estimates for Gd-DTPA in ischemic brain tissue: validation of MRI methods by comparison to quantitative autoradiographic estimates. ISMRM P977, 2005.

161. Lin W, Paczynski RP, Kuppusamy K, Hsu CY, Haacke EM. Quantitative measurements of regional cerebral blood volume using MRI in rats: effects of arterial carbon dioxide tension and mannitol. MRM 38:420-428 ,1997.